11-4-2015

Nanoscale Photovoltaic Performance of Thin Film Solar Cells by Atomic Force Microscopy

Yasemin Kutes
University of Connecticut - Storrs, yaseminkutes@gmail.com

Nanoscale Photovoltaic Performance of Thin Film Solar Cells by Atomic Force Microscopy

Yasemin Kutes, Ph.D.

University of Connecticut, 2015

Research efforts have been going on for decades to improve the efficiency of photovoltaic devices in order to effectively compete with other energy sources. Considering the length scale of the underlying phenomena, scanning probe microscopy (SPM) based techniques are ideally suited for studying solar cells due to their ability to probe functioning materials and devices under operating conditions, and to directly correlate local film structure with local properties. Accordingly, Atomic Force Microscopy (AFM) techniques have been developed and applied in this thesis to investigate the photoelectrical properties of CdTe/CdS polycrystalline thin film solar cells, as well as an emerging technology that utilizes organometallic halide perovskites.

As a first approach, a new technique, photoconductive AFM spectroscopy (pcAFMs) has been developed and performed on isolated, strain-relieved, photovoltaic (PV) micro-cells of polycrystalline CdTe in light and dark conditions. Performance metrics of these solar cells are mapped, revealing the behavior of individual grains, grain boundaries, and planar defects, achieving the requisite sub-10 nm spatial resolution. Same methodology has also been applied to spatially map the performance metrics of hybrid perovskite solar cells (PSCs), revealing substantial variations in the PV performance parameters that correlate with the thin-film microstructural features. Similar PSCs are also investigated using piezoforce microscopy (PFM), to show the presence of ferroelectric domains within high quality films, for the first time, as well as evidence for their reversible switching.

Two additional AFM techniques are also developed within the scope of this work, for planarizing samples and ultimately achieving nanoscale milling and tomography. With periodic, or simultaneous functional imaging such as photoconductive AFM measurements during such AFM-NanoMilling (AFM-NM), 3-dimensional tomographic datasets are acquired, which revealed the 3-d network of photocarrier pathways in CdTe.

In summary, the AFM methods developed and applied in this thesis provide a means to understand the fundamental transport mechanisms in photovoltaic systems with nanoscale resolution, with applicability to the knowledge-driven design of future devices that will have optimized materials and hence properties.

Nanoscale Photovoltaic Performance of Thin Film Solar Cells by Atomic Force Microscopy

Yasemin Kutes

B.S. Middle East Technical University, 2009

M.S. University of Connecticut, 2012

A Dissertation

Submitted in Partial Fulfillment of the

Requirements for the Degree of

Doctor of Philosophy

at the

University of Connecticut

2015

APPROVAL PAGE

Doctor of Philosophy Dissertation

Nanoscale Photovoltaic Performance of Thin Film Solar Cells by Atomic Force Microscopy

Presented by

Yasemin Kutes, M.S.

Major Advisor _____

Bryan D. Huey

Associate Advisor _____

George A. Rossetti, Jr.

Associate Advisor _____

Puxian Gao

University of Connecticut

2015

Nanoscale Photovoltaic Performance of Thin Film Solar Cells by Atomic Force Microscopy

This work is supported by:

Department of Energy, Office of Basic Energy Sciences, Division of Materials Sciences and Engineering, under award DE-SC0005037 (Electron and Scanning Probe Microscopies)

Acknowledgements

First and foremost, I would like to express my gratitude to Prof. Bryan Huey, who accepted me to his research group five years ago and has offered his constant support and guidance ever since. I consider myself very lucky for having had the chance to learn from him for many years, both on an academic and personal level.

I would like to thank my associate advisors Prof. George Rossetti, Jr., Prof. Puxian Gao, and committee members Prof. Barrett Wells and Prof. Brian Willis for their guidance and insightful comments throughout my studies and final defense.

I would like to thank my collaborators in Sandia National Labs, Dr. Jose Luis Cruz-Campa and Dr. Brandon Aguirre. It was a pleasure working with you and thanks again for hosting me in New Mexico.

I would like to also thank Prof. Nitin Padture and Mr. Yuanyuan Zhou for the exciting and impactful collaboration we had on the hybrid perovskite solar cells. It was an honor and pleasure working with you and our collaboration certainly added a lot to my career.

I would like to acknowledge my colleagues in Huey AFM Group for always being kind and helpful. I would like to especially thank Dr. James Bosse. His wisdom, support and friendship helped me get through the tough times during this journey. I would like to also individually thank Ms. Linghan Ye, Mr. Manuel Rivas, Dr. Vincent Palumbo, Dr. Justin Luria, Mr. James Steffes, Mr. Alejandro Lluberes, Ms. Alexandra Merkouriou, Ms. Aliya Carter, Mr. Zach Thatcher, Mr. Gyuho Song and Mr. Ryan Cordier for the great times we shared and all the fruitful discussions we had. You make the Huey AFM Lab one of a kind.

I would like to acknowledge all members of the DPD Materials Science group at Groton Pfizer Research Center for giving me the opportunity to have a great summer internship with them and learn a lot. It was an honor working with you on exciting projects which added a lot to my skills and career. I would like to extend my special thanks to my boss Dr. Robert Wadams for his guidance and sharing his work experience with me.

There are many people who have held a very special place in my life throughout this journey and will always do so in the many more years to come. I cannot thank Jack and Jodi Gromek enough for the tremendous help and guidance they offered me. I will always be grateful for everything you have done for me and I love you both very much. I also would like to thank Rossy, Sethy, Siddy and of course WOODY ☺ for their endless love and being so soft and fluffy.

I would like to acknowledge my dear friend, one of the kindest people on earth, Dr. Gursel Akcay for all the support and wisdom he has given and for the great times we spent together. I would like to also acknowledge Dr. Juan Villegas, who is one of the most thoughtful people, for his help, guidance and friendship. It is an honor and absolute pleasure to have gotten to know you both.

I would like to extend my great gratitude towards Prof. Macit Ozenbas who helped open up a whole new path for my career by guiding and supporting me. It is an honor to be his student and taking his class has changed my life forever. Thank you for accepting me to your lab 8 years ago and making all this possible today.

And my family… First, I would like to express my immense gratitude and love towards my teyze, Halise Erem and my eniste, Mehmet Erem for their unconditional love, help and continuous support. My cousin, Oktay Ozbek, you have been the big brother I never had to me

and you always made sure to prepare me for what is next. Thank you very much for always checking up and keeping an eye on me. My big sister, Nijsje Dorman, I do not know how to even start expressing my gratitude towards you. I love you so much and I feel so lucky to be able to discuss everything with you. Thank you very much for guiding me in every possible way you could.

Finally, I would like to thank my mother Oya Kutes, my father Suleyman Kutes, who are the most caring and loving parents and my sister, Muge Kutes, who is the sweetest sister ever. I would like to dedicate all my achievements to you all and I love you so much. Thanks for giving your all to me and putting me in the center of your life all the time. I would not be able to do this without your unconditional love and support…

…This dissertation is dedicated to my mom Oya and my dad Suleyman…

Table of Contents

Table of Figures

Chapter 1: Introduction

1.1 Scope of Research

As the energy demands of modern society continue to increase, raising significant environmental concerns, substantial research on renewable energy technologies is important for realizing the potential of cleaner energy resources [1]. Among the major renewable energy systems, solar energy is the most abundant, inexhaustible and cleanest during operation of all viable options to date [2]. It will become truly main-stream when the ratio of performance to cost becomes comparable with other energy sources [1], requiring roughly a 3-10 fold improvement over current technologies.

Thus far, efforts have primarily addressed the development of cost-effective technologies and/or improved efficiency to compete effectively with other energy sources, including innovative technologies based on new solar cell architectural designs, as well as the exploration of advanced materials that may serve as better light absorbers and charge carriers [1]. Understanding both the operation and degradation processes in photovoltaic (PV) systems is thus a prerequisite to better engineer higher performing future devices and hence optimize the commercial competitiveness of these technologies. Up until now, several methods have been developed for electrical property characterization that progressed from macroscopic electrical testing to microprobe stations [3], with recent extensions to the sub-micron to nanoscale, implementing scanning probe and electron microscopy [4-6]. The characteristic length scales of many of the crucial phenomena, e.g. electron, hole and exciton transport distances, are of the order of 10's to 100's of nanometers, rendering scanning probe microscopy (SPM) a natural platform for exploration of these parameters, especially since it can be employed during *in situ* illumination [7].

A fundamental understanding of structure property relations in energy materials and devices on the mesoscopic and atomic levels is also required for better designs that would greatly increase the pace of progress [8]. This is because the physical and chemical phenomena that underlie the operation of energy devices occur at these very small scales, necessitating locally spatially resolved studies. These processes that occur at nanometer spatial scales must link to those at microscopic and then macroscopic scales. Atomic force microscopy (AFM) [9] techniques are particularly well-suited for studying solar cells due to their ability to characterize a wide variety of relevant properties, as well as structure, at length scales spanning nanometers to tens of microns [7] and under normal operating conditions. While most modern analytical and microscopy methods have important roles to play in understanding materials for next generation solar cells, SPM methods are unique in their ability to directly correlate local film structure with local properties such as photocurrent, carrier mobility, recombination rate, photovoltage etc. Here, patterned and continuous CdTe based thin film solar cells are investigated by photoconducting atomic force microscopy (pcAFM) and related newly developed techniques, where current/photocurrent maps of the solar cell surfaces can be acquired by raster scanning a conducting AFM probe during a constant applied voltage. Although, spatially resolved, these 2-d current maps provide only one data point in the current versus voltage (I/V) domain. Similarly, for a more quantitative approach, a voltage sweep can be applied while the AFM tip is fixed at a single point on the surface (no rastering) and a complete I/V curve may be acquired with high resolution in the voltage domain. However, this approach cannot capture the effect of defects and heterogeneities in the film, which again results in a lack of dimensionality. To address these issues, a new technique called photoconductive AFM spectroscopy (pcAFMs) has been developed. With this multidimensional technique, sequential conductive AFM images acquired

over an area are collected in dark and upon illumination of the specimen; with incrementally ascending (or descending) applied voltages per frame. From the resulting stack of high resolution current images, a matrix of I/V spectra is constructed where each pixel represents an I/V curve. From these curves, important solar cell performance metrics such as short circuit current (I_{SC}), open circuit voltage (V_{OC}) and maximum power (P_{MAX}) are extracted and mapped with nanoscale spatial resolution. These high resolution maps are very useful in investigating these performance parameters as a function of defects, changes in topography, or other artifacts. pcAFMs is ultimately applicable to a wide range of photovoltaic devices and provides faster (~20 times) results than conventional point by point mapping methods.

In order to investigate the role of crystal orientation on performance of these cells, certain regions of continuous film CdTe samples are modified by collaborators in Sandia National Laboratories, using focused ion beam (FIB) milling to create smooth surfaces that are suitable for electron backscatter diffraction (EBSD) mapping to be compared to the pcAFMs acquired data. Unfortunately, the electrical character of these EBSD mapped areas are found to have become essentially electrically insulating and featureless, possibly due to supersaturation of the surface by Ga ion used for FIB milling. To be able to image these problematic areas, various AFM probes of different stiffness and/or materials/work functions are used. A relatively high stiffness diamond coated conducting AFM probe was found to be a potential solution, in an unconventional way, due to its ability to scrape the altered top layer of the CdTe film in FIBed areas, exposing a fresh surface of the material with a more expected electrical behavior. This unconventional use of the diamond AFM probe, along with the suitable and convenient mechanical character of CdTe film, has opened up a whole new venue of research, allowing access to the depths of these devices.

Although SPM is often considered of as a surface technique [10] and this may be true for topography-only images, functional SPM methods can also convey information about processes occurring throughout the depth of a film — even probing buried interfaces [11, 12]. In addition, there also exist recent AFM techniques which are able to literally remove surface material through thermal-mechanical micro-machining [13]. Studies that combine milling with advanced techniques such as cAFM are rare, though, due to the generally limited robustness of conductive AFM probes. The first conducting tomographic images have only recently been reported, applied for three-dimensional nano-scale images of conductance in resistive switching memories and carbon nanotube interconnects [14]. In this work, cAFM scanning of the FIBed surfaces of CdTe solar cells resulted in current images that showed an electrically insulating top surface with highly conductive pits and pores which extend up to the bottom electrode. These observations made us want to explore beneath the top surface, and led to the development of two mechanical milling techniques by using AFM. One of these techniques is used solely for preparing smooth and/or angled CdTe surfaces. An as-grown CdTe film (or a material with similar mechanical behavior) can be planarized by using principles of *constant height AFM* imaging, where the AFM cantilever scans the surface at a user defined height that is kept fixed throughout the experiment. The cantilever applies a varying amount of force as a function of its spring constant and the topography of the film as it raster scans, where the force applied at each pixel is proportional to the relative height of that pixel. As a result of this differential force application, the topography of the scanned area gradually becomes flatter (resulting in a ~10 fold decrease in roughness) providing electrically unaltered and equally flat (optically reflective) surfaces as created by FIB milling, with a potential to be used in further EBSD studies.

The second technique, computed tomographic AFM (CT-AFM), combines nano-milling with simultaneous conductive/photoconductive AFM imaging. Again, a diamond coated AFM probe with a nominal 50 nm radius of curvature is utilized to map topography and photocurrents of CdTe/CdS solar cells. By applying forces on the order of micro-Newtons during scanning, the specimen is gradually milled frame by frame, while maintaining a contact radius and hence local spatial resolution on the order of 10-20 nm. All acquired photocurrent images are then rendered as a 3-d representation of the electrical behavior throughout the milled volume.

CT-AFM has enabled us to explore the depths of a CdTe solar device. To date, the influence of microstructural defects on the device properties in CdTe and other polycrystalline photovoltaics has largely remained unknown due to a lack of characterization techniques that are able to image electrical pathways through thickness with the necessary high resolution. Here, CT-AFM technique is first applied to micro and nano fabricated CdTe solar cells. The dimensions effectively generate poly and single crystalline microstructures, respectively, to better elucidate the significance of the network of possible transport pathways on solar cell operation. Analysis on the polycrystalline μ-cells showed some grains clearly outperforming or underperforming the rest. It is found that the optimally or most poorly performing regions do not generally correlate with any specific locations within the cell, such as at a critical depth in the film where recombination might be least likely. Instead, it is possible that the performance might correlate to specific orientations of CdTe grains, or even more likely to certain interfaces and defects. Regardless, these observations support the hypothesis that polycrystalline solar cell performance is strongly associated with nanoscale transport pathways that were essentially inaccessible until now.

Following the preliminary experiments, CT-AFM is also performed on essentially manufacturing grade continuous CdTe thin-film solar cells that are progressively nano-milled through the full thickness while photocurrents are mapped during *in-situ* illumination and/or biasing. The results suggest an orthogonal transport network comprising mostly vertical grain boundaries for e^- transport versus planar stacking faults for h^+ movement, conveniently diminishing recombination. These planar stacking faults are observed to have enhanced photocurrents, contrary to the conventional belief towards their adverse effects on device performance. Also, with supporting TEM studies, it is shown that these planar defects are associated with lamellae of wurtzite crystal structure sandwiched in the middle of more typical sphalerite grains. For comparison, CT-AFM is similarly applied to CdTe samples processed differently (without a $CdCl_2$ 'activation step'), which are both macroscopically less efficient and are found to lack a high density of the mentioned highly photoactive stacking faults.

CT-AFM thereby provides unique and valuable information giving access to the electrical performance of an entire volume. However, as is, it can only feasibly be employed throughout the whole volume with one applied bias condition at a time. Considering the solar cell performance metrics that are mapped with pcAFMs, it is clear that 3-d rendering of I_{SC} is the most convenient of all due to the fact that it is mapped under a 0 V biasing condition. Mapping V_{OC} on the other hand, requires application of gradually incrementing voltages at each frame, which, at this stage, cannot be achieved while simultaneously milling the material. Hence, pcAFMs and CT-AFM techniques are sequentially applied to fully functioning CdTe solar cells, to realize the change in these performance parameters (mapped by pcAFMs) as a function of CdTe film thickness (milling performed by CT-AFM).

The pcAFMs technique has been employed to spatially map the performance parameters of the emerging solar technology of hybrid perovskite solar cells (PSCs) as well. These devices, whose efficiencies have risen from 3.8% in 2009 to over 20% in 2014, hold unprecedented promise for low-cost, high-efficiency photovoltaics of the future. The collaborator site (Prof. Nitin Padture's facilities in Brown University, RI, USA) has the knowledge and capability to prepare high quality methylammonium lead triiodide ($CH_3NH_3PbI_3$ or $MAPbI_3$) thin films in particular, which we have used to create the first nanoscale-resolution maps of PV performance parameters of planar PSCs. These maps reveal substantial variations in the PV performance that again correlate with thin-film microstructural features such as intra-grain planar defects, grains, grain-aggregates, interfaces between them. The insights gained into the microstructure-localized PV mechanisms for these studies are essential for guiding the microstructural tailoring of such films for improved bulk PV performance in the future.

Finally, stemming from structure-property relationships, some of these OTPs are expected to be ferroelectric. Experimentally, though, their ferroelectric properties remain elusive and highly controversial. Various studies regarding the origin of the commonly observed hysteresis and a rate dependence in the photovoltaic response (current vs voltage) of $MAPbI_3$-based solar cells have been documented [15,16]. Possible causes include ion migration [17] and unbalanced charge collection rates at the interfaces [18], though it could be, at least in part, due to a ferroelectric effect [19, 20]. Hence, in a separate study, piezoforce microscopy (PFM) is performed on similar PSCs, fabricated again by the Padture Group, directly revealing the presence of ferroelectric domains for the first time in such films. The size of these domains is found to be about the size of the grains (~100 nm). By poling with DC biases, we also present evidence for reversible switching of these domain-like featuress. Although further work is

needed to see if finer sub-grain domains can be resolved, such results are crucial for the investigation of understanding the photovoltaic phenomena in perovskite-based solar cells, which have been topics of on-going debates.

The ultimate focus of this thesis work is therefore to improve and develop AFM characterization approaches for fundamentally understanding and thereby improving the local performance of both mature and emerging PV technologies. However, the photovoltaic performance mapping, planarizing, and tomographic methods introduced by this work are ultimately applicable to a far wider range of solar cell materials and semiconductors.

1.2 References

1. B. Parida, S. Iniyan, R. Goic, Renewable and Sustainable Energy Reviews 2011, 15.
2. N. Asim, K. Sopian, S. Ahmadi, et al., Renewable and Sustainable Energy Reviews 2012, 16.
3. D. K. Schroder, Semiconductor material and device characterization. 2006: Wiley-interscience.
4. S. Kalinin, A. Gruverman, Scanning probe microscopy. 2006: Springer Science - Business Media.
5. D. A. Bonnell, Scanning tunneling microscopy and spectroscopy: theory, techniques, and applications. 1993: VCH New York.
6. D. B. Williams, C. B. Carter, Micron 1997, 28.
7. D. A. Bonnell, S. V. Kalinin, Scanning Probe Microscopy for Energy Research: Materials, Devices, and Applications. 2013: World Scientific Publishing Company Incorporated.
8. D. o. E. B. E. S. (BES), Basic research needs for electrical energy storage. 2007.
9. Binnig, G., Ch Gerber, E_ Stoll, T. R. Albrecht, and C. F. Quate. "Atomic resolution with atomic force microscope." EPL (Europhysics Letters) 3, no. 12 (1987): 1281.
10. D. M. DeLongchamp, R. J. Kline, A. Herzing, Energy & Environmental Science 2012, 5.
11. O. G. Reid, G. E. Rayermann, D. C. Coffey, et al., The Journal of Physical Chemistry C 2010, 114.
12. H. Takano, S.-S. Wong, J. A. Harnisch, et al., Langmuir 2000, 16.
13. T. L. Chu, S. S. Chu, Progress in Photovoltaics: Research and Applications 1993, 1.
14. J. L. Cruz-Campa, D. Zubia, X. Zhou, et al. Photovoltaic Specialists Conference (PVSC), 2012 38th IEEE. 2012
15. Tress, W., Marinova, N., Moehl, T., Zakeeruddin, S. M., Nazeeruddin, M. K., & Grätzel, M. (2015). Understanding the rate-dependent J–V hysteresis, slow time component, and aging in CH3NH3PbI3 perovskite solar cells: the role of a compensated electric field. Energy & Environmental Science, 8(3), 995-1004.

16. Dualeh, A., Moehl, T., Tetreault, N., Teuscher, J., Gao, P., Nazeeruddin, M. K., & Grätzel, M. (2013). Impedance spectroscopic analysis of lead iodide perovskite-sensitized solid-state solar cells. ACS nano, 8(1), 362-373.

17. Almora, Osbel, Isaac Zarazua, Elena Mas-Marza, Ivan Mora-Sero, Juan Bisquert, and Germà Garcia-Belmonte. "Capacitive Dark Currents, Hysteresis, and Electrode Polarization in Lead Halide Perovskite Solar Cells." The Journal of Physical Chemistry Letters 6, no. 9 (2015): 1645-1652.

18. Ponseca Jr, Carlito S., Tom J. Savenije, Mohamed Abdellah, Kaibo Zheng, Arkady Yartsev, Tobjörn Pascher, Tobias Harlang et al. "Organometal halide perovskite solar cell materials rationalized: ultrafast charge generation, high and microsecond-long balanced mobilities, and slow recombination." Journal of the American Chemical Society 136, no. 14 (2014): 5189-5192.

19. Gottesman, Ronen, Eynav Haltzi, Laxman Gouda, Shay Tirosh, Yaniv Bouhadana, Arie Zaban, Edoardo Mosconi, and Filippo De Angelis. "Extremely slow photoconductivity response of CH3NH3PbI3 perovskites suggesting structural changes under working conditions." The Journal of Physical Chemistry Letters 5, no. 15 (2014): 2662-2669.

20. Kutes, Yasemin, Linghan Ye, Yuanyuan Zhou, Shuping Pang, Bryan D. Huey, and Nitin P. Padture. "Direct observation of ferroelectric domains in solution-processed CH3NH3PbI3 perovskite thin films." The Journal of Physical Chemistry Letters 5, no. 19 (2014): 3335-3339.

Chapter 2: Mapping Photovoltaic Performance with Nanoscale Resolution

2.1 Abstract

Photo-conductive AFM spectroscopy ('pcAFMs') is proposed as a high-resolution approach for investigating nanostructured photovoltaics, uniquely providing nanoscale maps of photovoltaic (PV) performance parameters such as the short circuit current, open circuit voltage, maximum power, or fill factor. The method is demonstrated with a stack of 21 images acquired during in situ illumination of micropatterned polycrystalline CdTe/CdS, providing more than 42 000 I/V curves spatially separated by ~5 nm. For these CdTe/CdS microcells, the calculated photoconduction ranges from 0 to 700 picoSiemens (pS) upon illumination with ~1.6 suns, depending on location and biasing conditions. Mean short circuit currents of 2 pA, maximum powers of 0.5 pW, and fill factors of 30% are determined. The mean voltage at which the detected photocurrent is zero is determined to be 0.7 V. Significantly, enhancements and reductions in these more commonly macroscopic PV performance metrics are observed to correlate with certain grains and grain boundaries, and are confirmed to be independent of topography. These results demonstrate the benefits of nanoscale resolved PV functional measurements, reiterate the importance of microstructural control down to the nanoscale for PV devices, and provide a widely applicable new approach for directly investigating PV materials.

2.2 Introduction

Thin film based solar cells such as CdTe, CIGS, and amorphous silicon are inexpensive competitors to conventional single crystal silicon. CdTe/CdS solar cells are a particularly mature technology for low-cost, terrestrial, thin film photovoltaic applications [1, 2], as they can be manufactured on low-cost glass instead of more costly semiconductor substrates, and scalable

manufacturing methods have been widely implemented. Polycrystalline CdTe is the primary absorber in these single junction solar cells, with a direct band gap of 1.5 eV at room temperature. CdS, with a direct band gap of 2.4 eV, functions as a window layer to the CdTe in a heterojunction. To serve as the anti-reflective front electrical contact, a transparent conducting oxide is used [3].

However, experimentally attained efficiencies for thin film solar cells such as polycrystalline CdTe and silicon [4] are consistently lower than the theoretical efficiencies based on the Shockley Quaeisser limit [5]. For both materials the theoretical efficiency is 32-33%, while the maximum experimentally obtained efficiency is 21% for CdTe [6] and 25% for silicon [4]. This has been attributed to spatial non-uniformities such as composition, morphology, grain boundary and crystallographic orientations [7], etc., though it is still not fully understood to what degree these features influence photovoltaic performance. This is partially because of challenges in directly measuring solar cell properties at these often nanoscale structures, the primary objective of the present work.

Even for single crystal (epitaxial) films, high defect densities resulting from lattice-mismatch between CdS and CdTe layers can cause low minority-carrier lifetimes [8]. These defects can also trap carriers, greatly reducing the open circuit voltage and efficiency of CdTe PV modules [8]. One approach to minimize such lattice-mismatch effects is compositional grading. For example ZnCdTe has been used to engineer a gradual shift in the lattice parameter between the CdTe and CdS layers [9, 10]. Equivalently, strain relief provided by nano or microstructured PV stacks can improve device efficiencies, a device geometry considered in this work. Combining both of these concepts, simulations predict that defect-free films are attainable in graded ZnCdTe

nanoislands below 90 nm on a side, with such solar cells potentially achieving up to 24% efficiency [10].

Figure 1 diagrams a cross-section of such a micro solar cell ('μ-cell'), with isolated PV islands of polycrystalline CdTe/CdS surrounded by non-PV dielectric (silica). This is sketched as mounted in an Atomic Force Microscope (AFM) for measurements of local photoconductivity during in situ illumination and spectroscopy (pcAFMs). The surface topography in fact displays the actual height of 9 distinct μ-cells in a 12 μm x 12 μm region. The accentuated vertical scale highlights the presence of distinct grains and grain boundaries within each μ-cell, with 1-10 grains apparent for any given island confirmed by separate studies of equivalent samples with electron back-scattering diffraction [11].

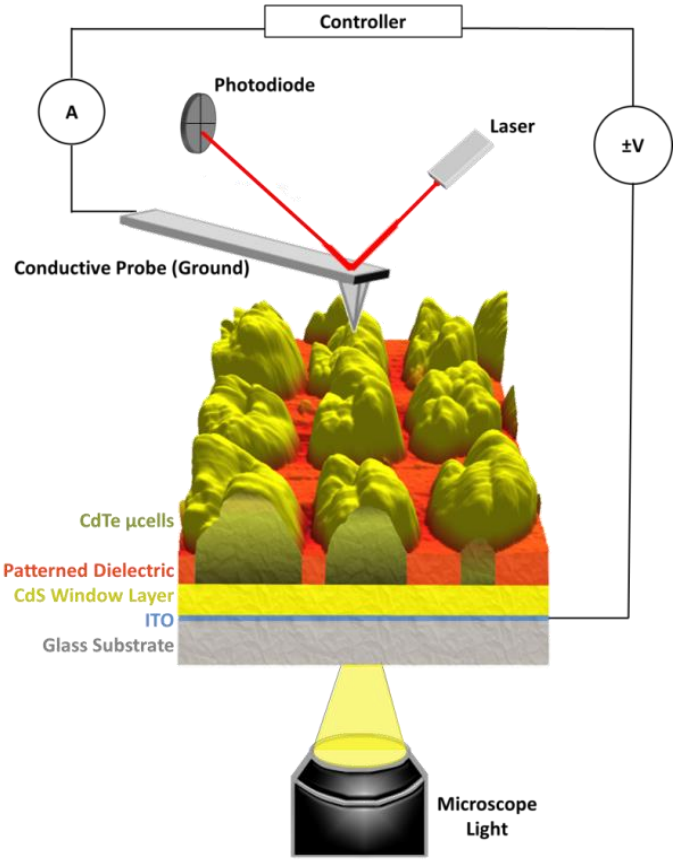

Figure 1: Configuration to illuminate the specimen from below, while measuring current with a conductive probe from above. The specimen is an array of CdTe/CdS photovoltaic µ-cells grown inside patterned SiO_2 dielectric windows. The CdTe µ-cells image was obtained from a 12 µm x 12 µm 3-d height measurement, revealing nine polycrystalline CdTe µ-cells protruding from the surrounding non-PV dielectric.

Functional maps of such nanostructured devices are often acquired with variations of scanning probe microscopy [12]. In circumstances where specimens are sufficiently conducting, scanning tunneling microscopy provides down to atomic scale resolution [13-16]. AFM is often a preferred platform for investigating photovoltaics, though, as it is robust even for regions that are not conducting, allows comparative measurements in dark conditions (without photocarriers), and provides nanometer scale spatial resolution. Conductive atomic force microscopy (cAFM) [17-20], transient-resolved electrostatic force microscopy [18, 21], and scanning surface

potential [22] or scanning Kelvin probe microscopy [18, 23, 24] are the most widely employed AFM variations for such studies of nanoscale electronic properties on semiconductors, ceramics, polymers, etc. Of course many other techniques have also been used with nanostructured or polycrystalline photovoltaics [25-27], such as transmission electron microscopy (TEM) [28], scanning electron microscopy (SEM) [29], and scanning transmission X-ray microscopy (STXM) [30], especially for investigations of morphology and microstructure.

Focusing on cAFM in particular, currents can be mapped with nanoscale resolution by scanning an area with a fixed voltage and recording the current, pixel-by-pixel. These individual images are excellent at qualitatively identifying heterogeneities, especially as they can be directly related to simultaneously imaged topographic features. For instance, CdTe/CdS μ-cells as sketched in Figure 1 were illuminated from below through the transparent substrate and conducting electrode, while the patterned structures and photocurrent were interrogated with c-AFM from above. Figure 2 presents the corresponding topography (a) and photocurrent during full, partial, and no illumination (b-d respectively) adjusted via neutral density filters, with 4 Vdc applied to the tip. The average current for the μ-cells in each image is 26 pA (160 mW/cm2, ~1.6 suns), 16 pA (~90 mW/cm2), and 10 pA (dark conditions), compared to 0 pA for the surrounding dielectric. Importantly, spatial variations of less than 5 pA are clearly resolved, with abrupt shifts over nanoscale distances of more than 30 pA in photocurrent, particularly apparent for the ~90 mW/cm2 illumination (c). Numerous heterogeneous current pathways are apparent, which in some locations are independent of the surface topography, whereas others correlate to grains or grain boundaries according to the surface topography (exemplified in the overlying oval).

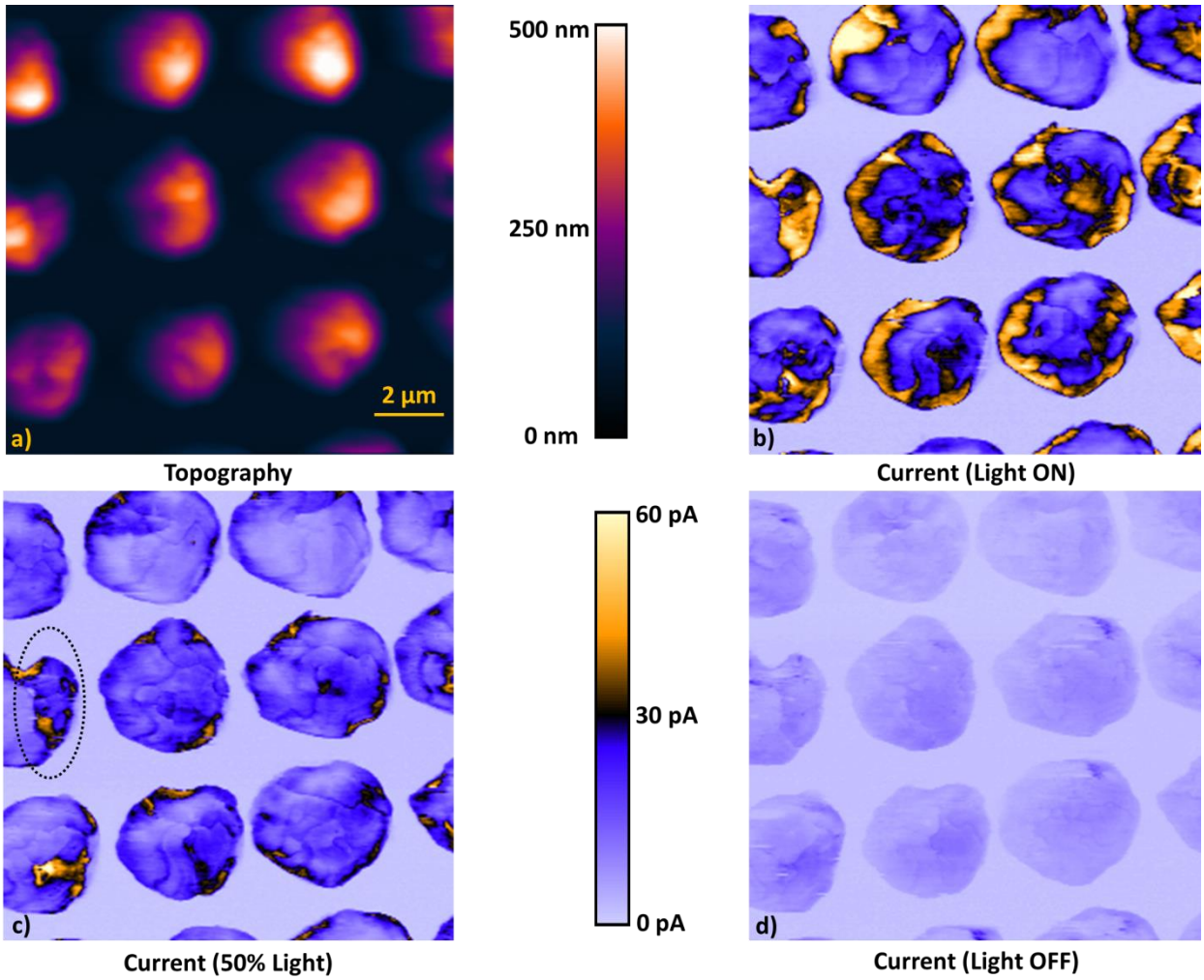

Figure 2: 12 µm by 12 µm topography (a) and photocurrent images of an array of µ-cells during 160 mW/cm^2 (~1.6 suns) illumination (b), 90 mW/cm^2 with overlain oval to identify a particular grain boundary (c), and in dark conditions (d), with topography and current scales as noted.

Coffey et al. have similarly used photoconductive AFM (pcAFM) to map local photocurrents in organic solar cells [17]. Under a concentrated intensity of 5 Suns, they also identified nanoscale variations in the photocurrent. Moutinho et al. investigated spatially dependent PV properties with cAFM as well, notably grain and grain boundary current enhancements as a result of various processing conditions for CdTe/CdS solar cells [31]. To interrogate dynamic effects, time-resolved electrostatic force microscopy [21, 32] and surface potential mapping [32, 33]

were separately developed by Ginger et. al., measuring the buildup and/or decay of photoexcited charges with demonstrated 100 nm spatial and 100 μs temporal resolution for nanostructured thin film organic solar cells. Such results identify where the majority of photoinduced charge is collected, important for optimizing the length scale and composition of phase separated domains in nanostructured polyfluorene blend solar cells.

From an engineering perspective, though, the actual performance of solar cells is typically assessed using macroscopic electrodes, and/or nano-manipulators to probe individual μ-cells. However, these relatively large-scale measurements are challenging in the event of any film defects such as pinholes or cracks. Even fine microprobes used for I/V measurements yield at best resolutions on the order of a couple of microns. Finer resolution is furthermore necessary to understand the fundamental mechanisms dominating device performance at the sub-granular level. This is particularly crucial in the case of nano and micro structured systems where grains and grain/phase boundaries may play significant roles in sensitivity, efficiency, or reliability. Consider the renewed interest in organometallic halide perovskites [34-36], solid oxide solutions like KBNNO [37], ferroelectric based devices [38], and solid state Graetzel cells [39, 40], where nano/microstructuring is likely or even crucial to device optimization.

Accordingly, in this work we present two new approaches for photovoltaic investigations. The first, photoconductive AFM spectroscopy (pcAFMs), determines and maps traditional macroscopic performance metrics for solar cells, except at the nanoscale. The second leverages high speed imaging concepts for efficient acquisition of high spatial resolution pcAFMs, yielding insight into fundamental PV mechanisms that was previously impractical experimentally. These methods are applicable to polycrystalline, amorphous, nanostructured, organic, ceramic, and

hybrid photovoltaics, but are specifically demonstrated here with microstructured CdTe/CdS solar cells.

2.3 Materials and Methods

Isolated micro CdS/CdTe p-n junctions were fabricated on indium tin oxide (ITO) coated glass substrates for conductive AFM (cAFM) characterization under light and dark conditions. Single sided ITO-coated glass substrates were purchased from Delta Technologies. Then, 100 nm-thick CdS films were grown on the substrates using chemical bath deposition. A 200 nm-thick SiO2 layer was deposited on the CdS films and patterned using optical lithography. The patterned SiO2 film consists of 2 µm-diameter window arrays. CdTe was selectively grown inside the 2 µm sized SiO2 windows using close space sublimation. This procedure results in arrays of isolated micro-CdTe cells grown on a polycrystalline CdS film as shown in Figure 1. More details about the fabrication of the microcells are described elsewhere [41].

All pcAFM measurements were performed using an Asylum Research MFP-3D AFM (Santa Barbara, CA, USA) operating in air. Current detection is achieved with an Asylum Research ORCA cantilever holder, featuring current resolution of 1pA up to a maximum of 20nA. Conducting (heavily boron doped) diamond coated silicon probes (Nanoworld CDT-FMR, Soquel, CA, USA) with a work function around 4.5 eV, which is close to the work function of p-type CdTe, a nominal 110 kHz resonant frequency and 1.5 - 18.3 N m^{-1} nominal spring constant were used for all AFM images. This system is built on an optical microscope (Nikon TE-2000, Melville, NY, USA) with a 40x objective lens (Plan Achromat, 0.65 numeric aperture), enabling simultaneous AFM imaging from the top during illumination from below. The sample is uniformly exposed over the field of view through the transparent substrate and conducting

electrode. While some shadowing or interference is feasible at the edges of the silica/micropatterned CdTe islands, this is believed to be negligible as systematic variations in photocurrents have not been observed at such feature edges.

The light source is primarily an unfiltered xenon arc lamp (Lambda DG-4, Novato, CA, USA) with an estimated illumination intensity of ~160 mW/cm^2 (1.6 Suns, measured with a silicon reference cell which was previously calibrated with a 300 W Oriel Instruments Sol2A solar simulator). The intensity can be programmatically adjusted between 100%, 55%, and 0% via neutral density filters. The relative percentages for neutral density filters are confirmed by an Optical Power Meter (Excelitas Technologies X-Cite XR2100, Ontario, Canada). This optical system is computer controlled (Improvision Volocity, software version 5.2.1 build 0, Waltham, MA, USA). A full spectrum 150 W Oriel Instruments solar simulator (Irvine, CA, USA) has also been employed for illumination, yielding similar results.

All experiments are performed in a dark room to avoid any influence of ambient light, though a <5 mW IR super luminescent diode (~860nm) used by the AFM to detect probe deflection is active throughout the experiments. This negligibly influences the photoconductivity measurements, however, because the IR source emits above the primary absorption range of the CdTe (850nm). Moreover, the overhanging cantilever and tip partially shadows the interrogated region of the specimen, which as a micron sized isolated island is totally independent of any surrounding material that might be incidentally illuminated.

2.4 Results and Discussion

2.4.1 Point by Point I/V analysis

The most common approach for studying photovoltaics with AFM is to record 'I/V' spectra by fixing a conducting probe at a desired location and then measuring the current while sweeping the tip or sample bias [42-44]. This essentially gains a new dimension in terms of current, but sacrifices the imaging capability of traditional cAFM. Figure 3(a) exemplifies this approach with curves acquired both on and off the CdTe µ-cells of Figure 2, both in light and dark, between ±3V applied to the tip. Each I/V curve shown in Figure 3(a) comprises 300 data points. Conductance values at each voltage are calculated from the slope of I vs. V from ±30 data points (b). These results confirm that the dielectric is insulating while the islands exhibit a diode-like behavior as anticipated. This is particularly enhanced upon illumination due to photocarrier generation.

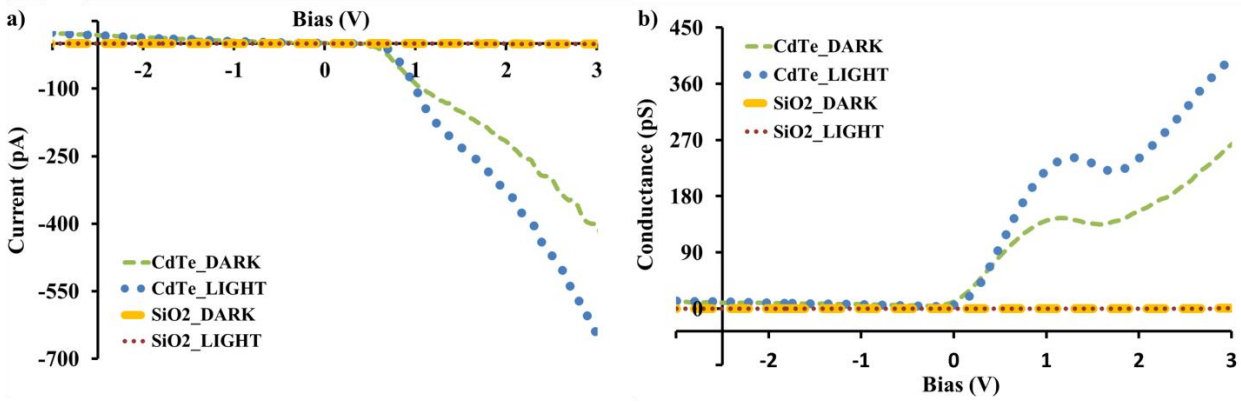

Figure 3: Current measurements as a function of applied bias from +3 to -3 Volts for single locations on SiO_2 versus CdTe µ-cells (left), revealing intensity dependent photoconduction (right) on the CdTe µ-cells and no signal for the surrounding dielectric, SiO_2.

While it may be feasible to correlate such individual I/V results to independent islands, or even some of the larger grains in the µ-cells, it is often impractical with conventional methods to

reliably couple nanoscale features with their I/V performance due to image drift, hysteresis in micropositioners, etc. Closed-loop scanners and high thermal stability systems can somewhat mitigate this concern. Higher spatial resolution is necessary, however, in order to identify current nonlinearities for truly nanoscale features such as the grains, grain boundaries, or possibly strain relieved island edges which are present in Figure 2.

Instead, this is normally attempted by acquiring arrays of I/V spectra, collected in a point-by-point fashion. Although time-consuming, such a measurement provides data that can be utilized to construct I/V response histograms, maps of easily extracted parameters such as the maximum conductance or current at specific voltages, etc. Conspicuously, though, device-relevant photovoltaic performance metrics have not previously been mapped, even though they are regularly extracted from equivalent but macroscopic I/V spectra following the equations below.

Equation **1** presents a simplified expression of current (I) as a function of applied voltage (V) [45], where I_{SC} is the short circuit current (current detected at V=0) and k is a constant determined for any given I/V spectra by least squares fitting. Equation 2 defines the open circuit voltage (V_{OC}), which is the bias at which the detected current is zero but which can also be calculated based on Equation 1. The maximum power (P_{MAX}) is determined according to Equation 3, and the empirical fill factor (FF) follows in Equation 4.

Equation 1: $$I = I_{sc}[exp(kV) - 1]$$

Equation 2: $$V_{oc} = \frac{1}{k} ln(1 - I_{sc})$$

Equation 3: $$P_{max} = I * V|_{\frac{\partial}{\partial V}(I * V)=0}$$

Equation 4: $$FF = \frac{I * V|_{\frac{\partial}{\partial V}(I * V)=0}}{I_{sc} * V_{oc}}$$

Accordingly, Equations 1-4 were applied to each of 1024 I/V spectra conventionally acquired over a 2 μm x 2 μm area with a data density of 32 x 32 pixels. Figure 4 uniquely presents corresponding photovoltaic performance maps of the measured (a) short circuit current (I_{SC}), (b) apparent open circuit potential (V_o), (c) maximum power (P_{MAX}), and (d) fill factor (FF), all determined near the edge of a μ-cell during ~160 mW/cm^2 illumination by the xenon arc lamp. Figure 4(a) reveals I_{SC} between 17 and 24 pA on the μ-cell, and negligible current for the surrounding dielectric as expected. The measured V_o for this same area ranges from 1 to 2 Volts on the μ-cell in Figure 4(b); these values are shifted from the true open circuit voltages by real resistances elsewhere in the electrical circuit. The map of P_{MAX} in Figure 4(c) exhibits a peak power of approximately 10 pW per pixel, with fill factors in Figure 4(d) of approximately 0.4 to 0.5. Note that occasionally the I/V spectra for individual pixels are not physically meaningful and are substituted instead with a value of 0. Only one such pixel exists in this image, apparent in Figure 4 at ~1.6 μm in x and 0.9 μm in y.

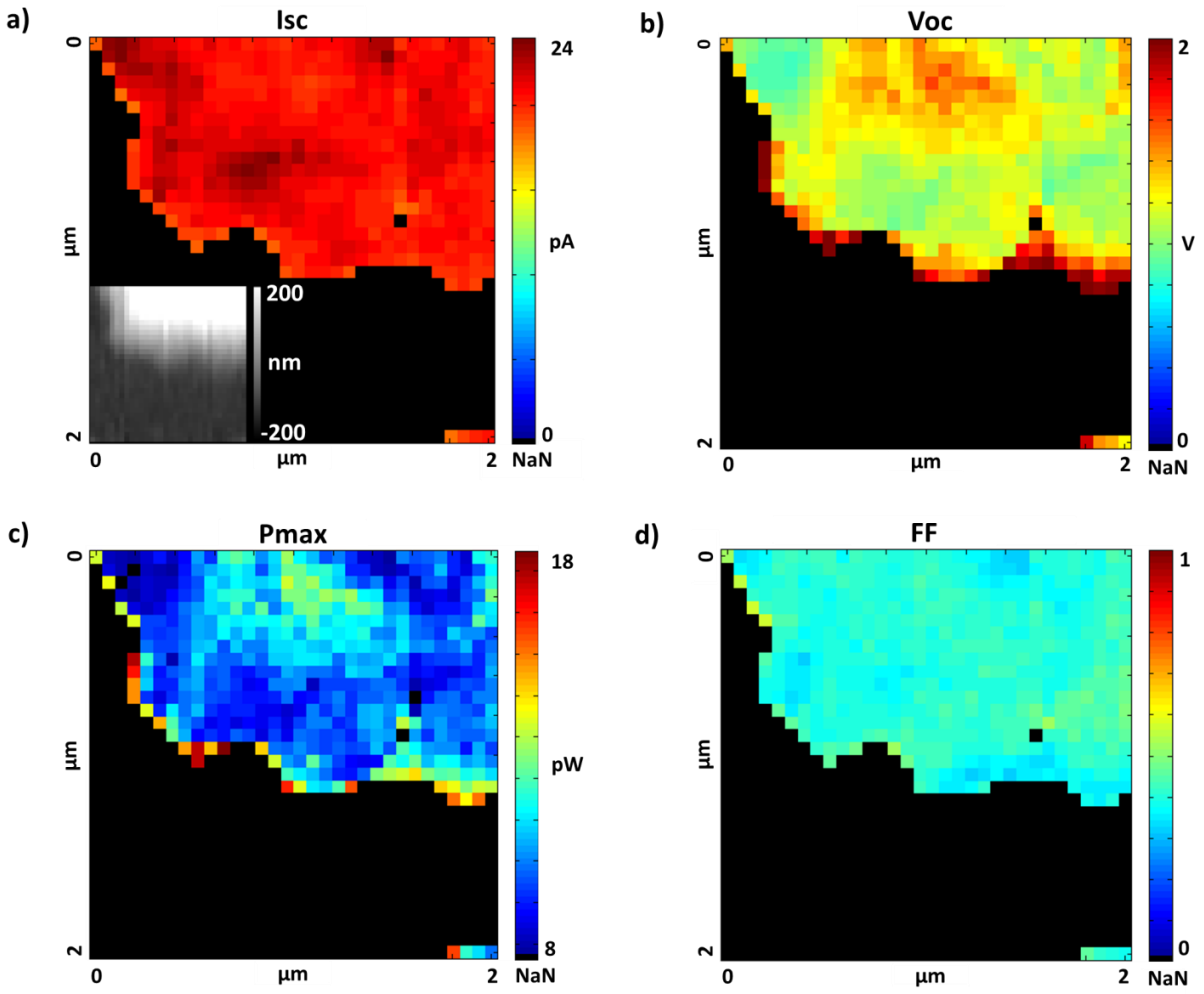

Figure 4: (a) Maps of short circuit current (I_{SC}) – topography as inset (grey scale), (b) apparent open circuit voltage (Vo), (c) maximum power (P_{MAX}) and (d) fill factor (FF), constructed with data collected over a 2 µm x 2 µm area at the edge of a µ-cell upon 100% illumination to the unfiltered Lambda DG-4 xenon arc lamp.

Visualizing I/V results from this newly considered perspective uniquely identifies the spatial variability, as well as correlations, between photovoltaic performance metrics. For example, in this case, I_{SC} often anticorrelates with Vo. The calculated maximum power scales most closely with Vo, though, while a weaker but still perceptible correlation is apparent for I_{SC} in the nearly uniform calculated fill factor. It is noteworthy that finer contrast, and/or additional PV performance metrics, can easily be determined by implementing sophisticated I/V curve fitting

routines, accounting for shunt and/or series resistances, incorporating thermal effects, etc. But the most striking comparison in all four images is obviously the clear contrast on the μ-cell compared to the underlying insulating substrate. Furthermore, finer features are apparent spatially, but not remotely resolved by the 62.5 nm pixels.

Given a tip-contact area on the order of 5-10 nm, higher pixel densities could be acquired to improve the spatial resolution. This conversely makes confident-correlations to specific nanoscale features even more challenging, though, for two main reasons: First, the tip position must continually be relocated and then fixed, often requiring re-approaching and withdrawing at each location, contributing to positional error (especially as most AFM systems are principally optimized for scanning instead of moving intermittently). Second, acquiring a high density of I/V spectra is slow, and hence susceptible to thermal drift and thus positional inaccuracies. For instance the data acquisition for Figure 4, with impressive but insufficient spatial resolution of ~60 nm, required ~90 minutes (~5.3 sec per pixel). By leveraging multidimensional and/or high speed AFM approaches instead, such as the photoconductive AFM spectroscopy (pcAFMs) approach described below, higher efficiency and spatial resolution investigations of nanoscale PV effects are feasible.

2.4.2 Photoconductive AFM spectroscopy

The pcAFMs method leverages Nanoscale Conductance Mapping (NCM) [30], which operates by acquiring multiple consecutive cAFM images, similar to Continuous Imaging Tunneling Spectroscopy imaging [46]. Each image is acquired with a distinct DC bias, incremented or decremented with every new frame as shown in Figure 5(top). Considering the current contrast for any given image pixel as a function of image frame (i.e. voltage) thereby yields spatially

localized I/V spectra, sketched in Figure 5(base) to determine the conductance for 2 distinct grains. Since each frame (i.e. voltage) is acquired in seconds or minutes, instead of hours to days for point by point I/V acquisition similar to Figure 4 but with an equivalent 256x256 pixel density, NCM thus enables essentially drift-free registry of topographic and I/V contrast. As implemented here, spatially resolved photocurrent spectroscopy is correspondingly achieved, and uniquely employed to map PV performance measures with high spatial resolution.

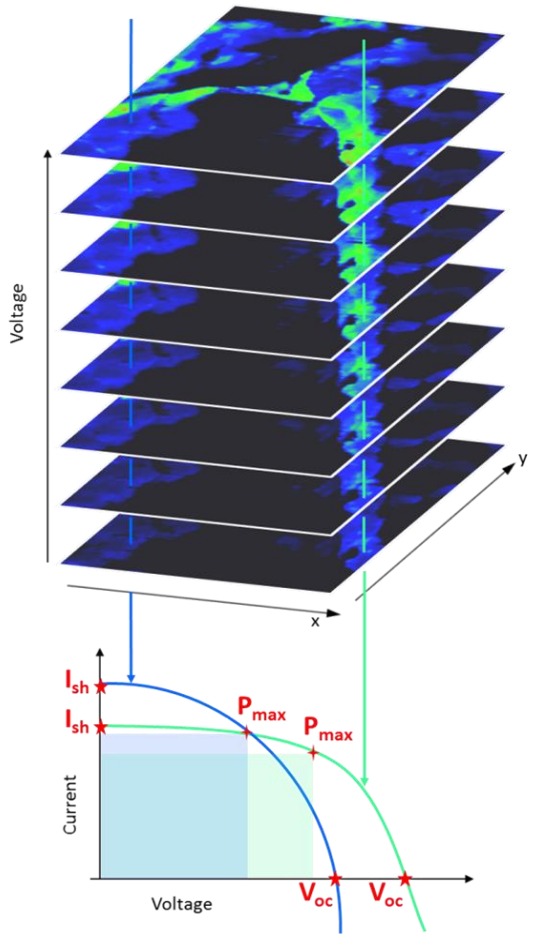

Figure 5: Sketch of photocurrent AFM spectroscopy (pcAFMs) based on a series of consecutive pcAFM images. Each image was acquired with incrementally higher applied voltages. An array of photocurrent versus voltage spectra is easily extracted for each pixel in the image stack, allowing photoconduction and other photovoltaic performance measures to be quantified and mapped.

Of course moderate spatial drift inevitably still occurs for the consecutive images. Given ~4 to 9 nm/min linear drift for the measurements presented here, this caused a continuous ~20-40 nm mis-registry per pixel from one image to the next. This was corrected by simple pixel translations for each image based on freely available software implementing feature tracking (e.g. the virtual stack alignment tool in ImageJ/FIJI software [47]). More sophisticated drift corrections such as rigid rotations and scaling, or even spatially nonlinear drift, can also be implemented. Conventional I/V arrays, on the other hand, are extremely susceptible to spatial drift, both because they take orders of magnitude longer to acquire with equivalent lateral densities, and since high spatial resolution topography data is not simultaneously mapped, accentuating the benefits of the pcAFMs approach presented herein.

Analyzing the array of all full I/V spectra, after truncating edge pixels with incomplete I/V ranges (thus up to 65,536 points in the absence of any spatial drift), thereby allows mapping of conductivity, turn-on voltages, non-linear coefficients, etc., with the same nanoscale spatial resolution as is inherent to the initial cAFM images. Voltage resolution is obviously determined by the number of image frames and voltage range. For the PV islands investigated here, a stack of 21 images with 250 mV steps from 0 to +5 Vtip are sufficient to identify nanoscale variations in the local PV performance. This is clearly under-sampled in the voltage domain compared to the point by point I/V spectra of Figure 3. However, the smooth I/V response measured at any one location compared to the variable, nonlinear, or even abrupt changes in I/V signals from one pixel to the next strongly justifies prioritizing spatial resolution over the number voltage steps. Of course even higher fidelity I/V data could always be acquired with more images (voltages), though at the expense of overall experiment durations.

For example, Figure 6 presents 15 consecutive current maps of a single µ-cell during 160 mW/cm2 illumination, acquired in a total time of just 90 minutes (256 lines per image at a 1 Hz line rate). Here a negative bias is applied to the ITO, resulting in forward biasing of the solar cell. A photocurrent of at least 100 pA is already detectible in isolated regions with -2 Volts, while appreciable photoconductivity is measured over at least 50% of the µ-cell by -4 Volts. Even with applied biases as strong as -5 Volts, as much as 30% of the µ-cell area does not exhibit any photocurrent. In fact, the presence of extended inactive regions within any given µ-cell is found to be a regular feature for the polycrystalline CdS-CdTe cells studied here. Such effects could partially explain the differences between theoretical and maximum achieved efficiencies for these cells [4].

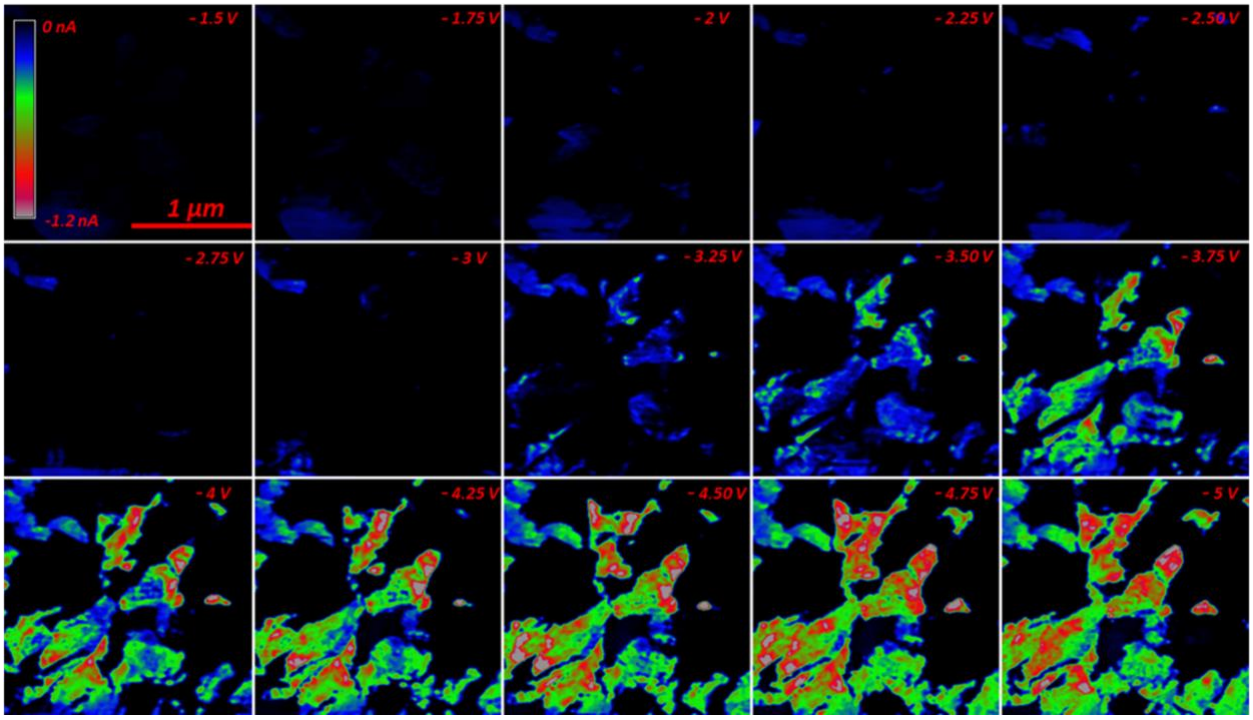

Figure 6: Montage of current images at distinct applied voltages as labeled, representing a subset of 21 total images for the same 2 µm x 2 µm area during 160 mW/cm^2 illumination.

For comparison, equivalent NCM was performed on 4 separate but nearby µ-cells (with comparable performance expected), both with and without any optical illumination. Figures 7, 8, and 9 summarize these results, with the drift corrected topography of each of the 4 separate island regions displayed in the top rows of Figure 7 and Figure 8, while conductance maps derived from the NCM data of Figure 6 and equivalent datasets are shown in the bottom rows, respectively. Figure 7 represents AFM tip biasing (Vtip) both in the dark (left) and during illumination (right, the specific data from Figure 6), revealing a strong enhancement due to photoexcitation with the local photoconduction rising to as high as 600-800 pS.

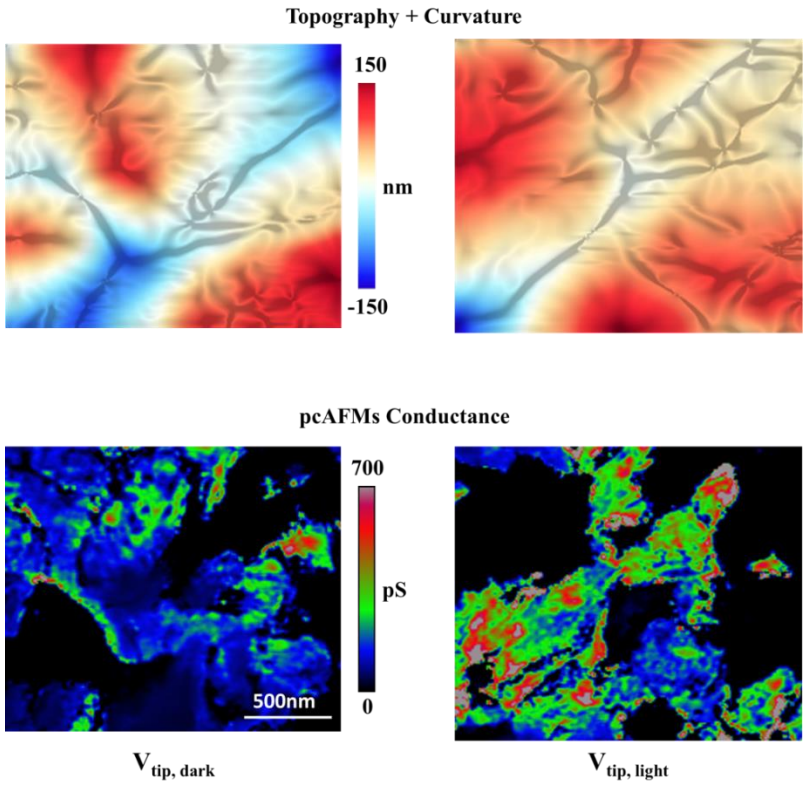

Figure 7: Comparison of topography (top row, in nm) and photoconduction calculated from pcAFMs (base, in picoSiemens), when the AFM tip is biased (Vtip) both in the dark (left) and during illumination (right). Topography (color contrast) is shown with local curvature superimposed by desaturating the image contrast according to the magnitude of curvature (i.e. peaks and valleys, where pcAFMs is most likely to exhibit artifacts if they exist at all.

As a control, images are also shown when oppositely biasing the transparent conductive oxide (Vtco) in Figure 8, for dark (left) and light (right) conditions (note the 10x smaller current contrast). As expected, the differences due to illumination are negligible and the absolute conductivity is small (<100 pS) in this purposefully oppositely biased micro solar cell. Figure 9 displays overlays of histograms for the 4 distinct conductance maps in Figures 7 and 8 with a logarithmic scale, highlighting the strong shift in conductance for the active quadrant of photoexctiation (Vtip) as well as a preponderance of essentially inactive regions in every case (~30-45% of each imaged area).

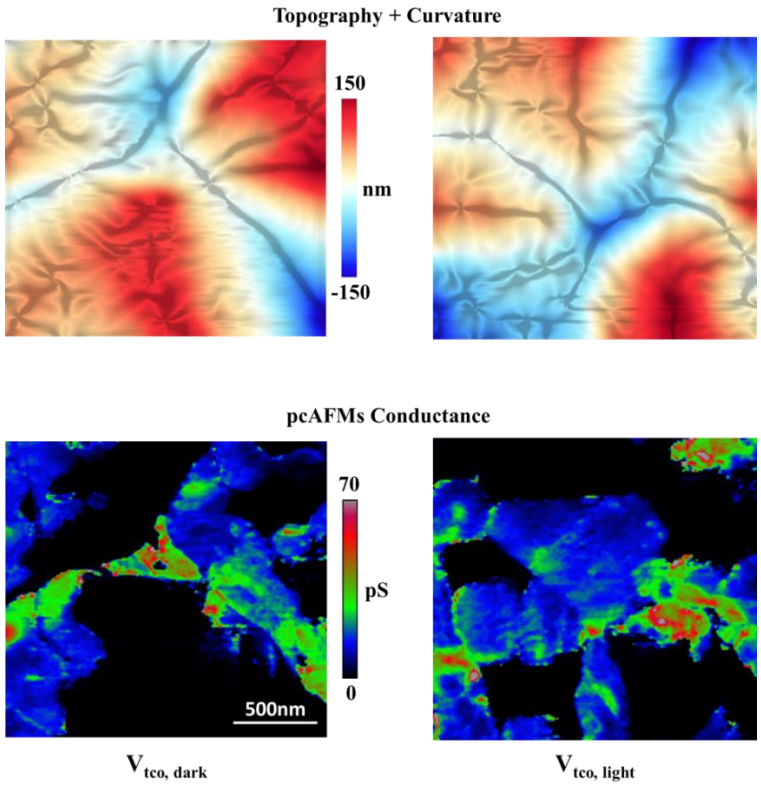

Figure 8: Comparison of topography (top row, nm) and pcAFMs resolved photoconduction (pS, note 10x enhanced scale compared to Figure 7) when the transparent conductive electrode is biased (Vtco) instead of the tip, both in the dark (left) and during illumination (right). Topography is again presented with the effects of local curvature superimposed by desaturating the image contrast according to local curvature.

The apparently inactive regions are clearly isolated to certain areas of the specimen, which sometimes but do not always correlate with specific grains according to the surface topography. Such contrast might instead result from artifacts related to distinct tip-sample contact areas as a result of the possibly convoluted tip and surface geometry common to all SPM methods. To consider this possibility, the local curvature was calculated based on two dimensional derivatives of the topography images. Its magnitude is depicted in the top rows of Figures 7 and 8 by linearly desaturating the topographic image contrast. These results identify that the relatively enhanced or diminished conductance occurs for arbitrary sample curvatures, and are absolutely independent of the local topography. Instead, it is postulated that they may result from local changes in composition or crystal structure. Most likely, though, is that the inactive regions are caused by non-ohmic or even electrically isolated (disconnected) grains with respect to either possible underlying grains, or the back transparent conducting electrode. This is supported by the sharp and seemingly faceted edges of many of the electrically inactive areas, suggesting a clear connection with microstructure. In this case, certain grain and grain boundary orientations, and ultimately current percolation pathways within the polycrystalline μ-cells, are therefore responsible for the observed spatially dependent solar cell performance, a topic of ongoing research.

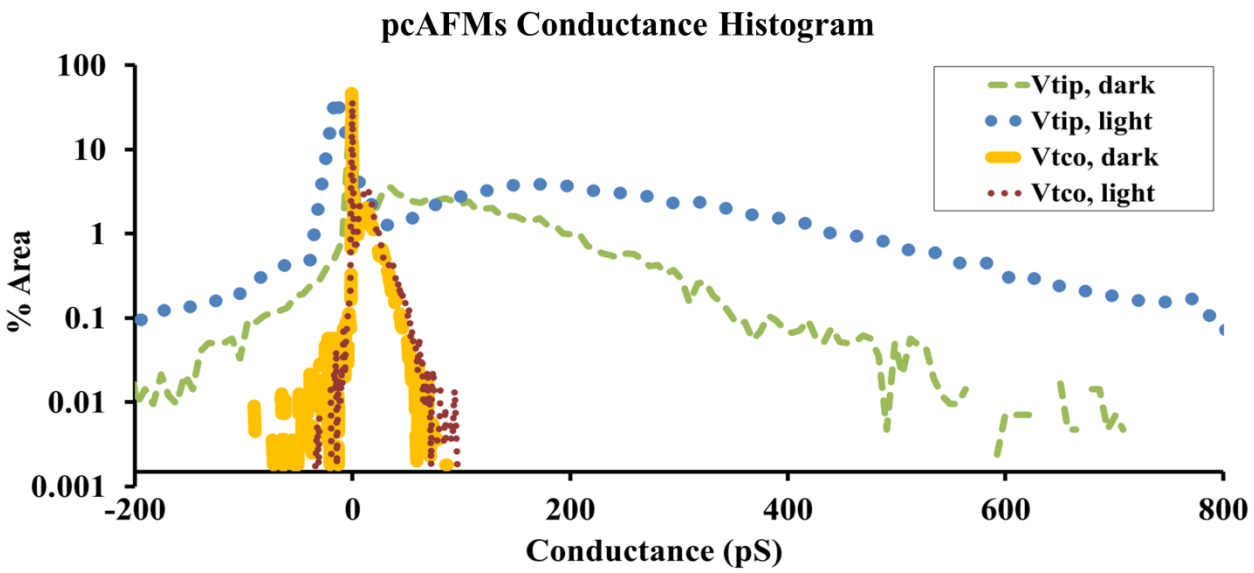

Figure 9: Overlays of NCM histograms for four separate but nearby µ-cells during photoexcitation, either when the AFM tip is biased (V_{tip}, mimicking normal solar cell operation) or when the transparent conductive electrode is biased (V_{tco}), both in the dark and with 160 mW/cm^2 illumination.

Leveraging the enhanced spatial resolution of pcAFMs, Figure 10 displays the calculated I_{SC} (a), Vo (b), P_{MAX} (c) and FF (d) for the active photovoltaic response summarized in the right column of Figure 7. Mean short circuit currents of 2 pA, open circuit voltages of 0.7 V, maximum powers of 0.5 pW, and fill factors of 0.3 are resolved. Comparing these images with those of Figure 4, which were equivalently calculated but conventionally acquired using point by point I/V measurements (with 1024 times fewer pixels and the possibility of substantially more spatial drift since the imaging required substantially longer to complete), truly nanometer scale variations in the local photovoltaic performance are now uniquely and efficiently resolvable.

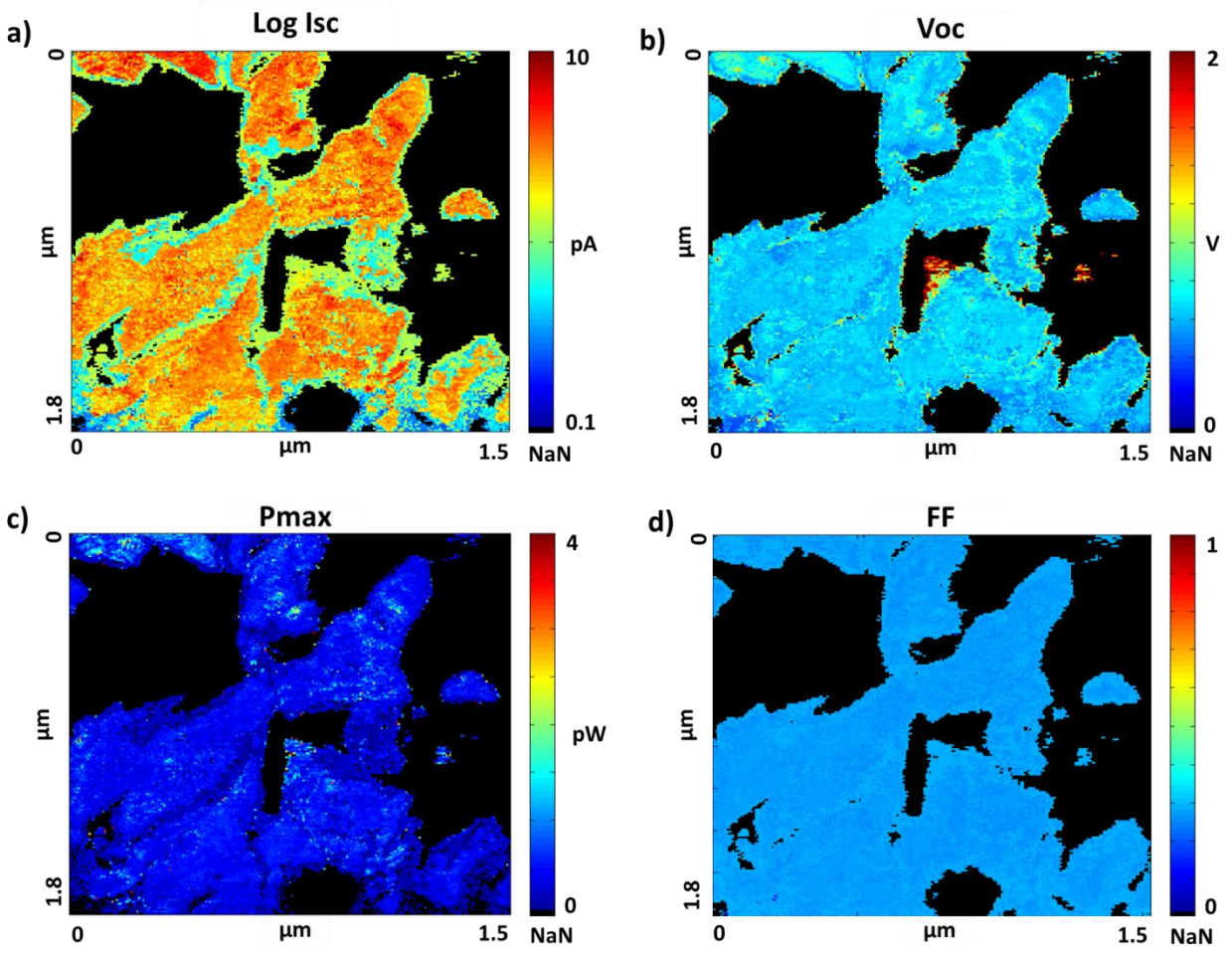

Figure 10: pcAFMs-resolved maps of I_{SC} (a), V*o* (b), P_{MAX} (c) and FF (d) upon 1.6 Sun illumination when the AFM tip is biased (V_{tip}) on the same 2 µm x 2 µm spot as considered for Figure 6.

2.5 Conclusion

The photovoltaic performance of solar cells has been uniquely probed at the nanoscale by a new approach, pcAFMs, coupling photoconductive AFM and I/V spectroscopy. The technique efficiently maps photovoltaic performance measures that are traditionally explored at the macroscale but have not been reported at the nanoscale. These in situ illumination experiments specifically identify that microstructure strongly influences the open circuit voltage, short circuit current, maximum power, and fill factor of the microfabricated CdS-CdTe polycrystalline solar

cells investigated here. The results are additionally proven to be independent of surface topography and curvature. Preferential photoconduction for certain grains, grain boundaries, and percolation pathways is clearly resolved, confirming the importance of microstructural control for the optimization of ultimate solar cell properties down to the nanoscale. Such findings warrant further investigations by this multidimensional SPM approach that is particularly suited for specimens where uniformity or pinholes complicate conventional (macroscopic) I/V measurements, as well as for micro- and nano-structured or heterogeneous electronic materials and devices.

2.6 References

1. Chu T L and Chu S S. Thin film II–VI photovoltaics. *Solid-State Electron.* 1995 **38** 533-49, 10.1016/0038-1101(94)00203-R

2. Cohen-Solal C, Barbe M, Afifi H and Neu G. Thin film CdTe solar cells. *J. Cryst. Growth* 1985 **72** 512-24, 10.1016/0022-0248(85)90199-X

3. Feng Z C, Chou H C, Rohatgi A, Lim G K, Wee A T S and Tan K L. Correlations between CdTe/CdS/SnO2/glass solar cell performance and the interface/surface properties. *Journal of Applied Physics* 1996 **79** 2151, 10.1063/1.361041

4. Green M A, Emery K, Hishikawa Y, Warta W and Dunlop E D. Solar cell efficiency tables (version 43). *Progress in Photovoltaics: Research and Applications* 2014 **22** 1-9, 10.1002/pip.2452

5. Shockley W and Queisser H J. Detailed Balance Limit of Efficiency of p-n Junction Solar Cells. *Journal of Applied Physics* 1961 **32** 510, 10.1063/1.1736034

6. First Solar I 2014 First Solar Builds The Highest Efficiency Thin Film PV Cell On Record.

7. Karpov V G, Compaan A D and Shvydka D. Effects of nonuniformity in thin-film photovoltaics. *Applied Physics Letters* 2002 **80** 4256, 10.1063/1.1483118

8. Wolden C A, Kurtin J, Baxter J B, Repins I, Shaheen S E, Torvik J T, Rockett A A, Fthenakis V M and Aydil E S. Photovoltaic manufacturing: Present status, future prospects, and research needs. *Journal of Vacuum Science & Technology A: Vacuum, Surfaces, and Films* 2011 **29** 030801, 10.1116/1.3569757

9. Morales-Acevedo A. Analytical model for the photocurrent of solar cells based on graded band-gap CdZnTe thin films. *Solar Energy Materials and Solar Cells* 2011 **95** 2837-41, 10.1016/j.solmat.2011.05.045

10. Cruz-Campa J L, Zubia D, Zhou X, Ward D, Sanchez C A, Chavez J J, Aguirre B A, Anwar F, Marrufo D and Spoerke E D. Record breaking solar cells: ZnxCdTe graded bandgap nanoarrays. November 2012

11. Aguirre B A. Growth and analysis of micro and nano CdTe arrays for solar cell applications *Department of Electrical and Computer Engineering* 2014 PhD
12. Bonnell D A and Kalinin S V 2013 *Scanning Probe Microscopy for Energy Research: Materials, Devices, and Applications*: World Scientific Publishing Company Incorporated)
13. Binnig G, Rohrer H, Gerber C and Weibel E. Surface Studies by Scanning Tunneling Microscopy. *Phys. Rev. Lett.* 1982 **49** 57-61, 10.1103/PhysRevLett.49.57
14. Akari S, Luxsteiner M C, Glockler K, Schill T, Heitkamp R, Koslowski B and Dransfeld K. Photovoltaic Characterization of Wse2 with the Scanning Tunneling Microscope. *Ann Phys-Leipzig* 1993 **2** 141-8, 10.1002/andp.19935050206
15. Glembocki O J, Snow E S, Marrian C R K, Prokes S M and Katzer D S. Nanoscale photovoltaic imaging using the scanning tunneling microscope. *Ultramicroscopy* 1992 **42-44** 764-70, 10.1016/0304-3991(92)90355-n
16. Pavlov A and Pavlova Y. Investigation of the surface topography of light emitting nanostructures of porous Si and the related photovoltaic effect by photoassisted scanning tunnelling microscopy. *Thin Solid Films* 1997 **297** 132-4, 10.1016/s0040-6090(96)09427-8
17. Coffey D C, Reid O G, Rodovsky D B, Bartholomew G P and Ginger D S. Mapping local photocurrents in polymer/fullerene solar cells with photoconductive atomic force microscopy. *Nano letters* 2007 **7** 738-44, 10.1021/nl062989e
18. Pingree L S, Reid O G and Ginger D S. Electrical scanning probe microscopy on active organic electronic devices. *Adv. Mater.* 2008 **21** 19-28, 10.1002/adma.200801466
19. Douhéret O, Lutsen L, Swinnen A, Breselge M, Vandewal K, Goris L and Manca J. Nanoscale electrical characterization of organic photovoltaic blends by conductive atomic force microscopy. *Appl. Phys. Lett.* 2006 **89** 032107--3, 10.1063/1.2227846
20. Dante M, Peet J and Nguyen T-Q. Nanoscale Charge Transport and Internal Structure of Bulk Heterojunction Conjugated Polymer/Fullerene Solar Cells by Scanning Probe Microscopy. *The Journal of Physical Chemistry C* 2008 **112** 7241-9, 10.1021/jp712086q
21. Coffey D C and Ginger D S. Time-resolved electrostatic force microscopy of polymer solar cells. *Nature materials* 2006 **5** 735-40, 10.1038/nmat1712
22. Huey B D, Lisjak D and Bonnell D A. Nanometer-Scale Variations in Interface Potential by Scanning Probe Microscopy. *J. Am. Ceram. Soc.* 1999 **82** 1941-4, 10.1111/j.1151-2916.1999.tb02023.x
23. Sadewasser S, Glatzel T, Schuler S, Nishiwaki S, Kaigawa R and Lux-Steiner M C. Kelvin probe force microscopy for the nano scale characterization of chalcopyrite solar cell materials and devices. *Thin Solid Films* 2003 **431-432** 257-61, 10.1016/s0040-6090(03)00267-0
24. Palermo V, Ridolfi G, Talarico A M, Favaretto L, Barbarella G, Camaioni N and Samorì P. A Kelvin Probe Force Microscopy Study of the Photogeneration of Surface Charges in All-Thiophene Photovoltaic Blends. *Adv. Funct. Mater.* 2007 **17** 472-8, 10.1002/adfm.200600122
25. Giridharagopal R and Ginger D S. Characterizing Morphology in Bulk Heterojunction Organic Photovoltaic Systems. *The Journal of Physical Chemistry Letters* 2010 **1** 1160-9, 10.1021/jz100100p
26. Moseley J, Moutinho H, Romero M, Jones K, Yanfa Y, Al-Jassim M and Ahrenkiel R 2013 Structural, chemical and luminescent investigation of MBE- and CSS-deposited CdTe thin-films for solar cells*16-21 June 2013)* p 2003-6

27. Moutinho H R, Moseley J, Romero M J, Dhere R G, Jiang C S, Jones K M, Duenow J N, Yan Y and Al-Jassim M M 2013 Grain boundary character and recombination properties in CdTe thin films*16-21 June 2013)* p 3249-54
28. Yang X, Loos J, Veenstra S C, Verhees W J, Wienk M M, Kroon J M, Michels M A and Janssen R A. Nanoscale morphology of high-performance polymer solar cells. *Nano letters* 2005 **5** 579-83, 10.1021/nl048120i
29. Hoppe H, Niggemann M, Winder C, Kraut J, Hiesgen R, Hinsch A, Meissner D and Sariciftci N S. Nanoscale Morphology of Conjugated Polymer/Fullerene-Based Bulk-Heterojunction Solar Cells. *Adv. Funct. Mater.* 2004 **14** 1005-11, 10.1002/adfm.200305026
30. Bosse J L, Grishin I, Kolosov O V and Huey B D. Multidimensional SPM applied for nanoscale conductance mapping. *J Mater Res* 2013 **28** 3311-21, 10.1557/jmr.2013.365
31. Moutinho H R, Dhere R G, Jiang C S, Al-Jassim M M and Kazmerski L L. Electrical properties of CdTe/CdS solar cells investigated with conductive atomic force microscopy. *Thin Solid Films* 2006 **514** 150-5, 10.1016/j.tsf.2006.03.003
32. Reid O G, Rayermann G E, Coffey D C and Ginger D S. Imaging Local Trap Formation in Conjugated Polymer Solar Cells: A Comparison of Time-Resolved Electrostatic Force Microscopy and Scanning Kelvin Probe Imaging. *J. Phys. Chem. C* 2010 **114** 20672-7, 10.1021/jp1056607
33. Pingree L S, Rodovsky D B, Coffey D C, Bartholomew G P and Ginger D S. Scanning Kelvin probe imaging of the potential profiles in fixed and dynamic planar LECs. *Journal of the American Chemical Society* 2007 **129** 15903-10, 10.1021/ja074760m
34. Lee M M, Teuscher J, Miyasaka T, Murakami T N and Snaith H J. Efficient hybrid solar cells based on meso-superstructured organometal halide perovskites. *Science (New York, N.Y.)* 2012 **338** 643-7, 10.1126/science.1228604
35. Noh J H, Im S H, Heo J H, Mandal T N and Seok S I. Chemical management for colorful, efficient, and stable inorganic-organic hybrid nanostructured solar cells. *Nano letters* 2013 **13** 1764-9, 10.1021/nl400349b
36. Kutes Y, Ye L, Zhou Y, Pang S, Huey B D and Padture N P. Direct observation of ferroelectric domains in solution-processed CH3NH3PbI3 Perovskite Thin Films. *The Journal of Physical Chemistry Letters* 2014 **5** 3335-9, 10.1021/jz501697b
37. Grinberg I, West D V, Torres M, Gou G, Stein D M, Wu L, Chen G, Gallo E M, Akbashev A R, Davies P K, Spanier J E and Rappe A M. Perovskite oxides for visible-light-absorbing ferroelectric and photovoltaic materials. *Nature* 2013 **503** 509-12, 10.1038/nature12622
38. Seidel J, Fu D, Yang S-Y, Alarcón-Lladó E, Wu J, Ramesh R and Ager J W. Efficient Photovoltaic Current Generation at Ferroelectric Domain Walls. *Physical Review Letters* 2011 **107** 126805, 10.1103/PhysRevLett.107.126805
39. Chang J A, Rhee J H, Im S H, Lee Y H, Kim H J, Seok S I, Nazeeruddin M K and Gratzel M. High-performance nanostructured inorganic-organic heterojunction solar cells. *Nano letters* 2010 **10** 2609-12, 10.1021/nl101322h
40. Gratzel M. Photoelectrochemical cells. *Nature* 2001 **414** 338-44, 10.1038/35104607
41. Aguirre B A, Zubia D, Ordonez R, Anwar F, Prieto H, Sanchez C A, Salazar M T, Pimentel A A, Michael J R, Zhou X, McClure J C, Nielson G N and Cruz-Campa J L. Selective Growth of CdTe on Nano-patterned CdS via Close-Space Sublimation. *Journal of Elec Materi* 2014 **43** 2651-7, 10.1007/s11664-014-3104-7

42. Otsuka Y, Naitoh Y, Matsumoto T and Kawai T. A Nano Tester: A New Technique for Nanoscale Electrical Characterization by Point-Contact Current-Imaging Atomic Force Microscopy. *Japanese Journal of Applied Physics* 2002 **41** L742-L4, 10.1143/jjap.41.l742
43. De Wolf P, Snauwaert J, Clarysse T, Vandervorst W and Hellemans L. Characterization of a point-contact on silicon using force microscopy-supported resistance measurements. *Applied Physics Letters* 1995 **66** 1530, 10.1063/1.113636
44. Kelley T W and Frisbie C D. Point contact current–voltage measurements on individual organic semiconductor grains by conducting probe atomic force microscopy. *Journal of Vacuum Science & Technology B: Microelectronics and Nanometer Structures* 2000 **18** 632, 10.1116/1.591251
45. Xiao W, Dunford W G and Capel A 2004 A novel modeling method for photovoltaic cells(vol 3): IEEE) p 1950-6
46. Hamers R J, Tromp R and Demuth J 1993 *Scanning Tunneling Microscopy*: Springer) pp 97-100
47. Lowe D G. Distinctive image features from scale-invariant keypoints. *International Journal of Computer Vision* 2004 **60** 91-110, 10.1023/B:VISI.0000029664.99615.94

Chapter 3: Nanoscale Planarization, Cross Sectional Milling, and Electrical Characterization of CdTe Thin Films via Atomic Force Microscopy

3.1 Abstract

Focused ion beam milling is the most common modern method for preparing specific features for microscopic analysis, even though concomitant ion deposition and amorphization remain persistent challenges especially when they modify the local materials properties of interest. Atomic Force Microscopy, on the other hand, should be able to mechanically mill specific regions at the nanoscale without chemical or high energy ion damage, due to its resolution, directionality, and fine load control. Accordingly, AFM-NanoMilling is used to planarize polycrystalline CdTe thin film solar cells, with a resulting decrease in the RMS roughness by an order of magnitude, even better than for a FIB polished surface. AFM-based maps of the short circuit current during exposure to 15 equivalent suns of broadband illumination reveals substantially stronger contrast following such purely mechanical milling, uniquely enabling direct correlations between the local photovoltaic performance and the polycrystalline microstructure according to EBSD measurements of the same area. Extending this concept to oblique milling, smooth shallow-angle cross-sections are also uniquely prepared, revealing a gradual decrease in the average short circuit current and maximum power, but a relatively consistent open circuit voltage, for diminishing thicknesses of the CdTe absorber. AFM-based nano-milling therefore provides a unique method for selective area smoothing and/or sectioning of specimens while preserving their functionality, enabling novel correlations between e.g. nanoscale properties according to advanced AFM measurements with the local microstructure according to grain orientation mapping via electron back scattering diffraction.

3.2 Introduction

In addition to conventional methods of specimen polishing and cross-sectioning such as mechanical grinding [1], sputtering [2], areal ion milling [3], or focused ion beam (FIB) milling [4], it has occasionally been reported that AFM is also able to remove surface material through purely mechanical [5], thermal-mechanical [6], and other probe based micro-machining methods [7 - 9]. To date, though, few have leveraged these capabilities with advanced SPM modes such as conductive AFM imaging. The first conducting tomographic images were only recently been reported, applied for three-dimensional nano-scale images of conductance in resistive switching memories and carbon nanotube interconnects [10]. We are separately applying such concepts for nanoscale tomographic investigations of solar cells with *in situ* illumination [11].

AFM based nanomilling, either for planarizing or sectioning, is achieved via purely mechanical means, specifically a combination of pressure, a robust and sharp AFM probe, and shear loading. This is crucial for avoiding any adverse effects on local mechanical, electronic, magnetic, or other properties, which frequently suffer from ion implantation [12] or sub-surface amorphization [13] in the cases of focused or large area ion milling [14]. AFM nano-milling, on the other hand, is shown here to be able to prepare highly planar and even shallow angle cross section, specimens optimized for functional property mapping such as AFM-based imaging of photovoltaic performance parameters which are barely possible after FIB-polishing.

AFM nanomilling is best performed with robust diamond probes using forces on the orders of microNewtons to tens of microNewtons. These are unsurprisingly much higher loads than is typical for simple imaging, since the objective of most versions of scanning probe microscopy is to minimally interact with the specimen instead of purposefully modifying it. The milling rate

naturally depends on the mechanical properties of the specimen, as will any resulting changes in microstructure, defects, and/or properties. In the case of CdTe, layers ranging from 1-50 nm have been removed in a single pass of the tool, i.e. during one image frame.

Of course AFM is based on sensing mechanical interactions between a sharp tip and sample, in the case of contact mode by monitoring the deflection of an integrated cantilever. For standard 'constant-force' imaging (right side of Figure 11), a fixed (and low) set-point deflection (def_{sp}) is maintained with a feedback loop that piezo-electrically shifts the relative z-position of the sample in response to any changes in the deflection (i.e. height). To achieve planarization, on the other hand, 'constant-height' mode [15, 16] is implemented in which the probe is raster scanned in a single plane and the lever freely deflects (Δ_{def}) more or less when encountering protruding or recessed surface features (left side of Figure 11). This causes faster or slower local milling, respectively, since via Hooke's law the force applied by the probe at any given milling position ('F_m') varies linearly with the relative height deviations from the planar scan trajectory. This assumes that the resulting deflections remain in the linear range (i.e. Hooke's law still applies), which is reasonable for the <300 nm maximum topographic features encountered compared to the >100 um long cantilevers. With nominal spring constants <100 N/m the lever stiffness is also sufficiently small compared to the compliance of the diamond probe and CdTe specimen that tip-sample indentation is minimized, which would otherwise cause forces applied e.g. on the top of a protrusion to scale sub-linearly with the feature height. In any case, some combination of indentation, shear, and wear mechanisms cause the surface to mill, necessarily the focus of an entirely separate study.

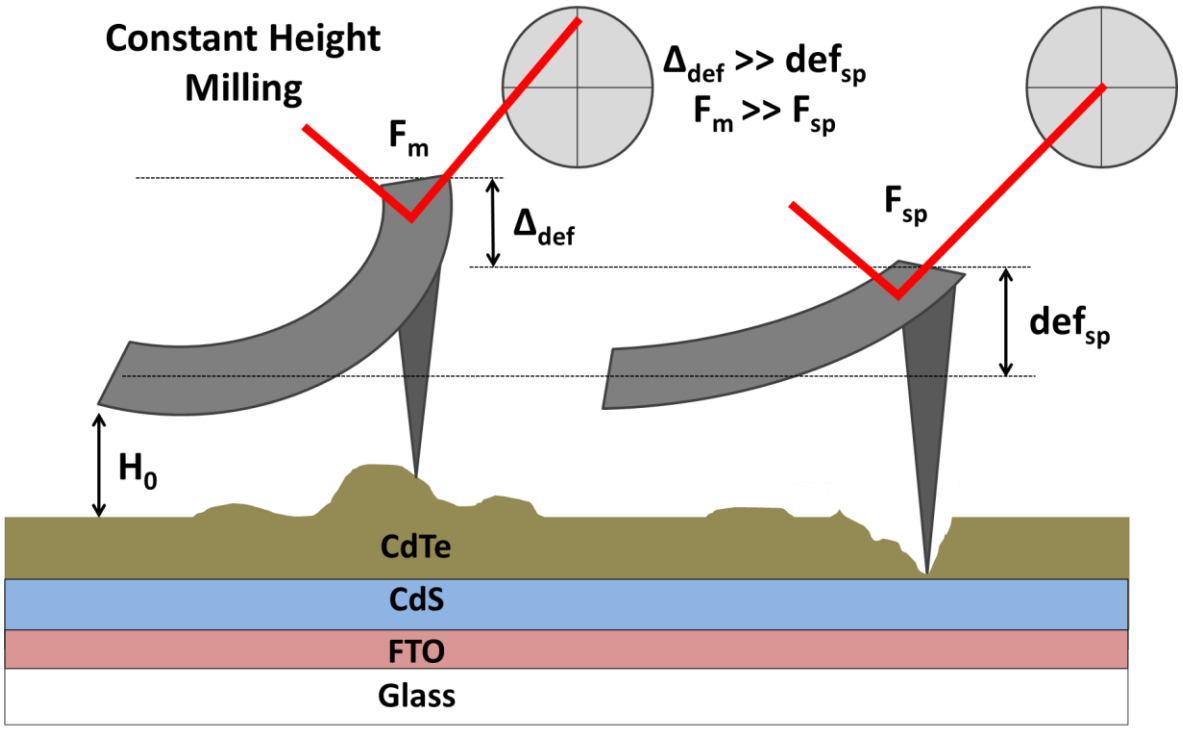

Figure 11: Schematic of AFM-NanoMilling via constant height imaging, where the AFM probe is scanned in a fixed plane (H_0) with the feedback loop disabled, causing the milling force (F_m) applied by the tip at any location to scale linearly with the local surface height since this causes essentially equivalent lever deflections (Δ_{def}).

Practically, a constant-Force image with a low, non-milling set-point load (F_{sp}) is first acquired in order to identify the overall topography in the field of view and hence to determine an appropriate leveling plane. AFM-Nanomilling (AFM-NM) then progressively smooths the surface by simply disabling or minimizing the feedback loop while repeatedly scanning with the lever at a fixed height (e.g. H_o). More complex milling patterns of course are possible by actively varying the applied load as a function of position, and/or through patterned motion of the probe [5, 17, 18]. But because the interaction is 'focused' at the probe apex, once the surface has sufficiently milled to the scanning plane, no further sample modifications occur, i.e. no further

damage occurs unlike e.g. ion milling schemes where prolonged exposure continues to damage the sample due to un-focused ion exposure.

3.3 Materials and Methods

All smoothing/milling work and photocurrent measurements are performed using an MFP-3D AFM (Asylum Research, Santa Barbara, CA) operated in air. Current detection is achieved with an Asylum Research ORCA cantilever holder, providing current results from 20 nA down to a noise floor of ~1 pA. Heavily doped, conducting diamond-coated silicon probes (Nanoworld CDT-NCHR, Soquel, CA, USA) with a nominal 400 kHz resonant frequency and 80 N m^{-1}nominal spring constant are used for both mechanical ablation and photocurrent collection. This system is mounted on an optical microscope (Nikon TE-2000, Melville, NY) with a 40× objective lens (Plan Achromat, 0.65 numeric aperture), enabling simultaneous photocurrent imaging from the top during illumination from below through the FTO/glass cathode. The light source is a focused, unfiltered MK-R 12 V LED (CREE, Durham, NC) with an approximate illumination intensity of 1.5 $W.cm^{-2}$ (equivalent to 15 suns but not AM1.5G spectrum) as measured with a silicon reference cell calibrated separately with a 300 W Sol2A solar simulator (Oriel Instruments, Irvine, CA). Ambient light is minimized by experimenting in a dark room. However, a ~5 mW infrared (IR) super-luminescent diode (860 nm) is used by the AFM to detect probe deflection throughout the experiments. This is not expected to influence the photoconductivity measurements, because the overhanging cantilever and probe partially shadow the interrogated region of the specimen from this continuous background of low intensity IR photons. Furthermore, the CdTe absorption edge is below 860 nm [19].

Closed-space sublimation technique was used for the fabrication of samples which have market comparable device performance for open circuit voltage and efficiency (0.8V, 12.3%, respectively). 120 nm of n-type cadmium sulfide was deposited on a fluorinated-tin oxide (FTO) glass substrate. Next, a ~1.8 micron thick p-type cadmium telluride, which functions as the bulk of light absorption, was deposited on the cadmium sulfide. $CdCl_2$ heat treatment followed this, since samples without any activation treatment result in very low efficiencies (0.1%). Also, $CuCl_2$ treatment was performed, which results in heavy doping of the back surface of CdTe and serve as a hole-blocking layer. The back electrode, consisting of a layer of carbon and nickel, is removed after macroscopic measurements in preparation for AFM studies.

3.4 Results and Discussion

Applying this procedure to an as-grown thin film solar cell with exposed polycrystalline CdTe, Figures 12a-b present low-load, contact-mode, AFM topography images before and after AFM-NM smoothing/planarization for a single 15 μm by 15 μm area. Bright and dark contrast indicates granular protrusions and depressions as much as ±150 nm for the as-processed CdTe surface (a), while the milled surface (b) has maximum features of only ±15 nm (note a 10x contrast magnification is necessary to observe any topographic features compared to the initial surface). The RMS roughness for these images correspondingly diminishes by an order of magnitude, from ~87 nm to ~9 nm. Most important, however, are Figures 12c-d. These display the simultaneously acquired photocurrent upon 15 suns of illumination without any applied bias, i.e. maps of the short circuit current (I_{SC}) generated by the operational solar cell.

The photocurrent in the initial case (c) peaks as high as 110 pA, is extremely discontinuous (speckled), and the signal magnitude and speckle density appears to couple somewhat to the

granular surface structure. Comparisons with (a) indicate that higher photocurrents are apparent at many topographic crevices, most likely locations of grain boundaries, either suggesting an actual increased short circuit current at such interfaces, or resulting from a sensitivity to topographic artifacts due to inconsistencies in the tip-sample contact area.

After milling approximately 300 nm into the specimen, on the other hand, a remarkable correlation appears between the short circuit current (d) and clear microstructural features. Homogeneous instead of speckle-dominated contrast appears within single grains, with distinct crystallites exhibiting almost discrete I_{SC} magnitudes ranging from 10 to 110 pA, This indicates high photocarrier mean free paths compared to the sub-µm grain size, otherwise gradients across large grains would most likely result. Meandering grain boundaries between arbitrarily oriented grains are no longer bright either, supporting the supposition that their apparently higher short circuit currents in (c) are topographic artifacts, not unique interfacial properties. Many regions, often seemingly sub-granular, are bounded by sharp, linear interfaces though, suggestive of planar defects such as twin boundaries or stacking faults intersecting the specimen surface. Most of these linear interfaces, as well as the general grain boundaries in the film, effectively act as barriers or sinks for photoconductivity, since the properties of the solar cell are highly localized to individual grains or sub-grains. It is also notable that the highest performing grains comprise less than 25% of the overall area, providing a clear opportunity for manufacturing higher efficiency solar cells by identifying the fundamental explanation for the order of magnitude variation in performance from one region to another.

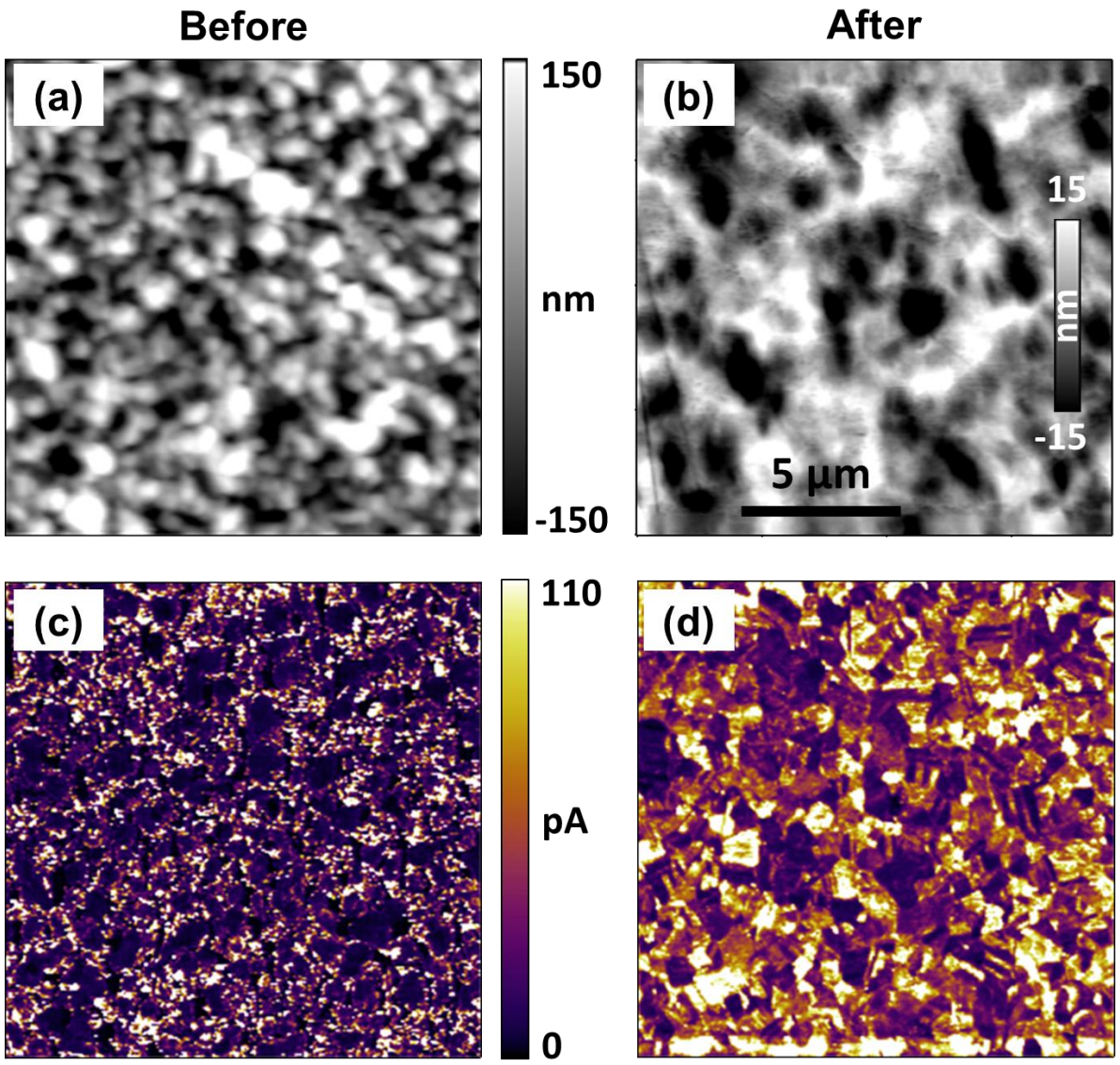

Figure 12: Topography of a 15 µm x 15 µm area on a CdTe thin film before (a) and after (b) planarization via AFM-NM (note 10x contrast enhancement in b), above the corresponding photocurrent images (c and d, respectively) collected upon ~1.5 W.cm^{-2} illumination through a transparent-conducting cathode (FTO/glass) with a positionable conductive AFM probe anode from above.

Focusing first on the dramatically different results for the initial and milled surfaces, 3 possible explanations must be considered. The first is that the initial CdTe surface may be oxidized or otherwise passivated from ambient exposure for ~1-6 months before imaging, interfering with

the collection of photogenerated holes by the conducting tip. Upon AFM-NM, 'fresh' CdTe is exposed which does not have such a limitation. In this event, though, photocurrent maps of a milled area such as (d) would degrade as a function of environmental exposure time, which has not been observed even after 3 months of ambient exposure. The second possibility is that a poor-performing top layer exists as a result of specimen fabrication in general, even though cells processed identically to those investigated here exhibit impressive 12-15% efficiencies. Still, if there is an effective inhomogeneous and non-conductive 'crust,' such results may provide unique insight into its extent and ultimately lead to a manufacturing solution to such a clear problem for overall solar cell efficiency. The third explanation is that the results upon AFM-milling simply lack the image artifacts caused by the substantially varying tip-sample contact areas in (a) and (c). There is certainly no uniform correlation between topography and I_{SC} once planarized in (b) and (d). Regardless, these images prove that AFM-NM provides both a significant reduction in roughness, valuable for reducing topographic artifacts in other functional AFM measurements, as well as previously unavailable insight into materials properties at and near a surface.

Further extending this concept, AFM-NM was performed with a sample mounted with a slight tilt angle (α) as sketched in Figure 13a to create a shallow angle cross-section through the entire thickness of the ~1.8 μm CdTe film. During these constant-height (fixed plane) scans, as the tip gradually climbs the specimen slope (right to left in the diagram), the applied load correspondingly rises and should mill proportionally faster according to our hypothesis of an essentially linear milling rate with force. Indeed this occurs, resulting in a cross section that geometrically exposes the ~1.8 μm thick CdTe film over a lateral distance of ~20 μm as shown in the 3-dimensional rendering of the surface topography after milling (c). Remounting the specimen so the primary sample surface is again level (b) for follow-on standard (constant force)

imaging, the uniform slope in the milled region is especially apparent (d). This sectioning technique is obviously extremely convenient for AFM measurements since the sample does not have to be separated into multiple specimens (as in FIB 'lift out' cross sections), and does not have to be remounted or transferred to other instruments (though can be). For measurements such as the photoconductive investigation conducted herein, selective shallow angle windows additionally allow the effects of topographic artifacts to be separated from surface or depth dependent properties, since exposed surface, smooth material up to the surface, and sub-surface areas can all be imaged in the same field of view.

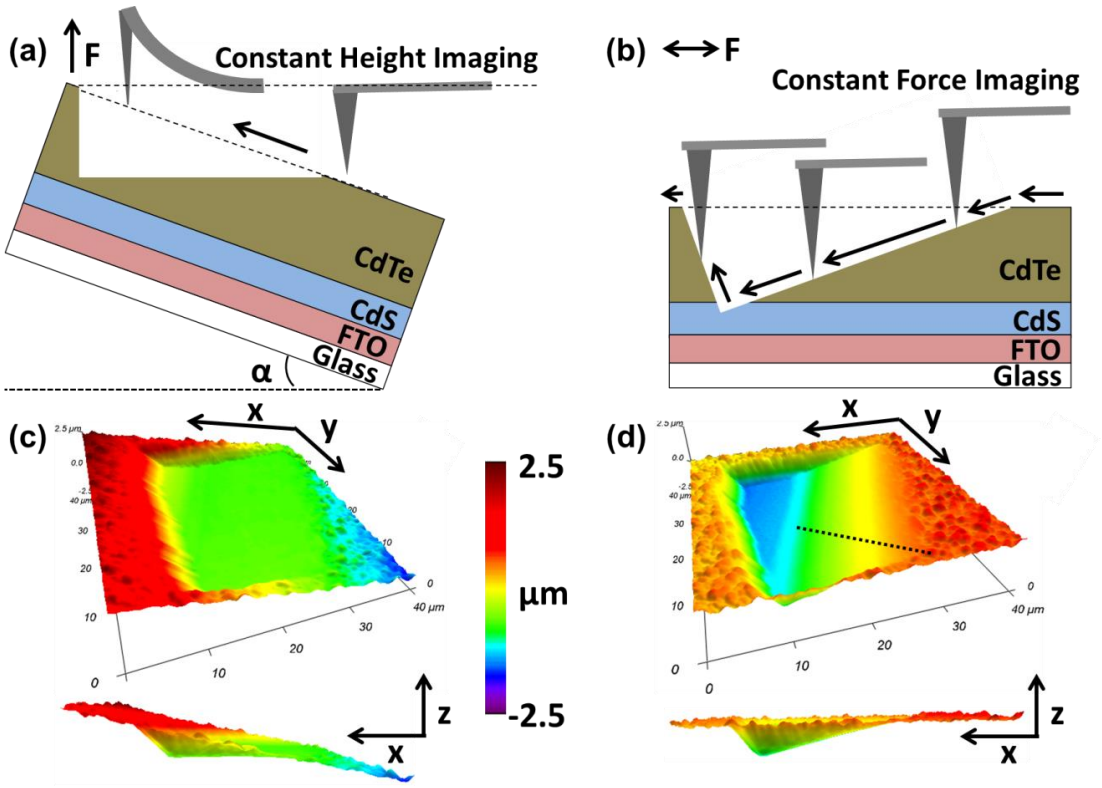

Figure 13: Schematic of small-angle cross section prepared by AFM-NM of a specimen tilted by (α) where constant-height imaging causes increased milling as the slope is encountered (a). This creates a smooth milled region, apparent when 3-d rendered (c, 40 µm by 40 µm) and especially for a cross-sectional perspective (base). Upon remounting without any specimen tilt (b), the continuous height gradient and hence the cross-sectional perspective for the planar opening is revealed (d).

For instance, Figure 14 presents 20 consecutive photoconductive AFM spectroscopy (pcAFMs) current maps [20] from a 15 µm by 30 µm area within the milled region as indicated in Figure 13d. All images were acquired during ~1.5 W.cm^{-2} illumination, but each at different bias voltage, between 0 and 950 mV in steps of 50 mV as indicated. Repeating each voltage condition twice, once for dark (mostly featureless images) and once for light conditions, ultimately required ~170 minutes to collect all 40 images (256 lines per image, 1 Hz line rate). To better visualize the progression of the current response as the CdTe solar cell locally approaches open circuit (V_{OC}) conditions (typically 700-800 mV), image contrast for the entire montage is displayed in a logarithmic scale representing 1 - 100 pA. A maximum photocurrent of ~3 nA is in fact detected at the top most film surface (upper right of each image) for short circuit conditions (0 mV). This is because the current polarity becomes negative as expected beyond the open circuit voltage for any given location (i.e. no longer generating power, not shown here since this is beyond the range of normal solar cell operation).

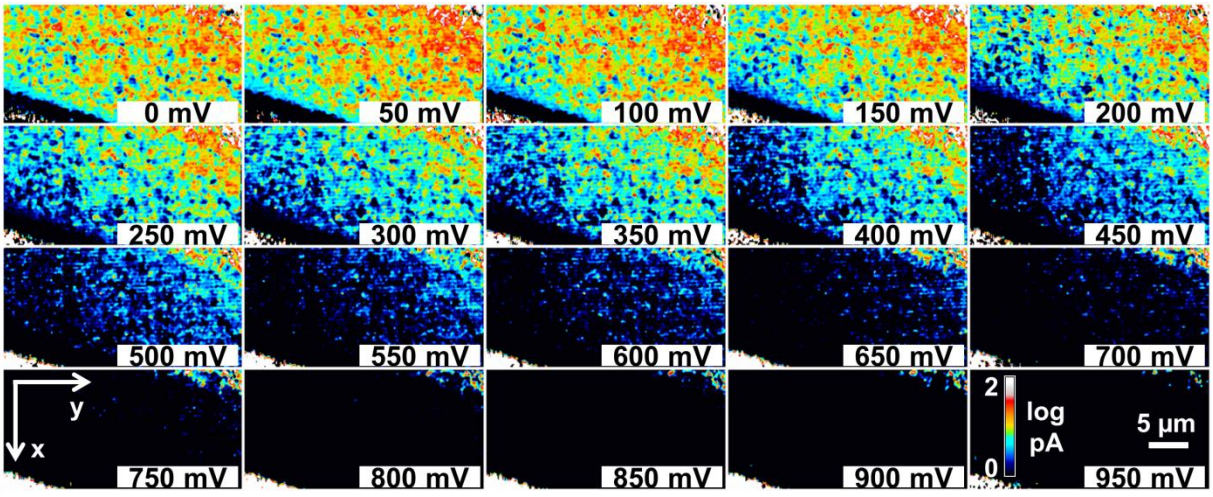

Figure 14: Montage of pcAFMs current images (Light-Dark), all for the same 30 µm × 15 µm area during ~1.5 W.cm^{-2} illumination, but each at distinct applied voltages as labeled. Note the logarithmic current scale, representing currents from 1 pA (black) to 10 nA (white).

Analyzing the contrast (photocurrent) for the n^{th} pixel from each image as a function of the image frame (applied bias) then provides a customary current/voltage spectrum for that location, from which the local short circuit current (I_{SC}), maximum power (P_{MAX}), and open circuit voltage (V_{OC}) can be determined [21]. Repeating this for all 32004 resolved pixels (after cropping to accommodate specimen drift) results in the photovoltaic performance maps of Figure 15, with spatial resolution of 0.014 μm^2/pixel. Average cross sections are also presented of these signals (d-f, respectively), climbing the milled slope along a 20.8 μm traverse within the overlain rectangular regions. The plots are displayed with an accompanying gradient in the baselines to clarify the bottom (B) from the top (A) of the CdTe. Note that I_{SC} and P_{MAX} are displayed in logarithmic scales to better visualize the strong shift in locally measured photovoltaic performance across the various layers of the solar cell.

The milling is sufficiently deep that a layer of highly conductive fluorinated tin oxide (FTO), the transparent conducting cathode at the base of the solar device (also known as the front contact), is physically exposed in the lower left corner. It progressively whitens with bias in Figure 14 since it is essentially a weakly resistive path to ground. A CdS layer deposited on the FTO (to the right in the images) next appears as a dark band of contrast for each of the photovoltaic performance maps of Figure 15. This is because there is no absorber (CdTe) present and hence no photoconduction.

Most important, though, is the PV performance through the thickness of the CdTe layer, from the base (point B) through 1.8 μm to the initial surface (A). Again noting the log scales, both I_{SC} and P_{MAX} decrease strongly as the thickness of the absorber is reduced until the CdS interface is reached. V_{OC}, on the other hand, remains essentially constant throughout the film as expected,

again until the CdS is reached. There is substantial spatial variation for all 3 of these performance metrics, however, tied to microstructure as with Figure 13.

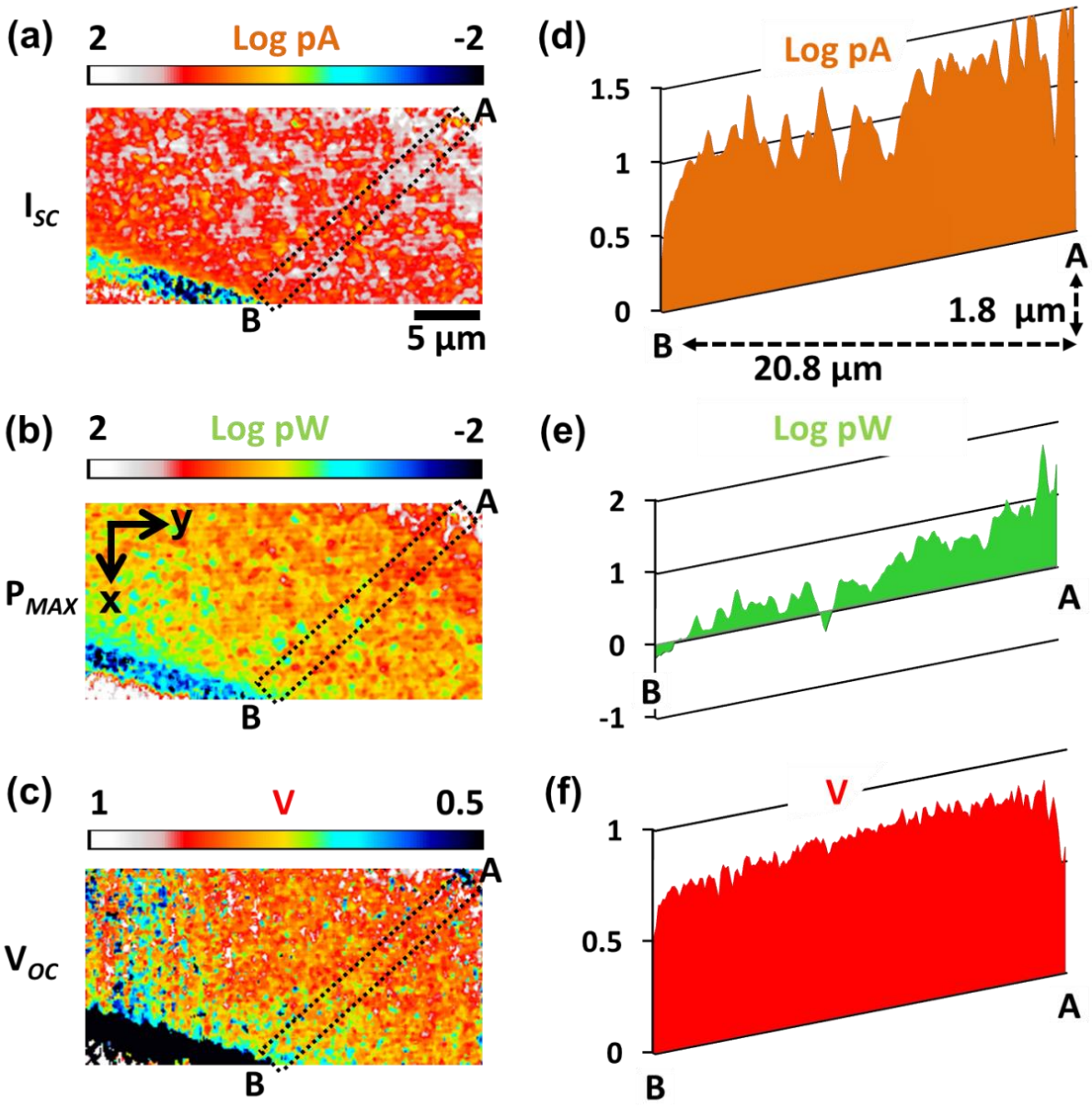

Figure 15: pcAFMs resolved maps of (a) I_{SC}, (b) P_{MAX} and (c) V_{OC} maps on a 15 µm × 30 µm area upon ~1.5 W.cm^{-2} illumination when TCO is biased. Truncated scales for each image are as shown. Full scale plots of cross-sections are shown in d, e and f, as dotted lines between points A and B, orthogonal to milling direction.

To better assess the influence of microstructure in these results, electron backscatter diffraction (EBSD) is applied on similar but thinner (~200 nm) polycrystalline CdTe solar cells with the objective of correlating locally resolved PV properties with the orientations of columnar grains. The as-prepared roughness of the high quality CdTe films is too great for optimal EBSD mapping, however, necessitating a planarization procedure typically conducted by FIB smoothing. Of course TEM-based Kikuchi analysis could be performed instead, though this requires even more substantial specimen thinning. Accordingly, Figure 16a presents a low magnification secondary electron SEM image of a FIB 'shaved' polycrystalline CdTe thin film. Between the unmodified surface regions at left and right, essentially unavoidable vertical streaks are apparent associated with heterogeneities in the FIB milling process due to the film roughness and microstructure. Zooming in by a factor of 4 (b), an EBSD orientation map is overlain on the SEM image. Figures 16c and d present AFM topography and simultaneous I_{SC} images of the same area, respectively. Clearly, there is little if any current response in this FIB-exposed region, most likely due to Ga ion implantation, sub-surface amorphization, etc. influencing the local electrical and optical properties.

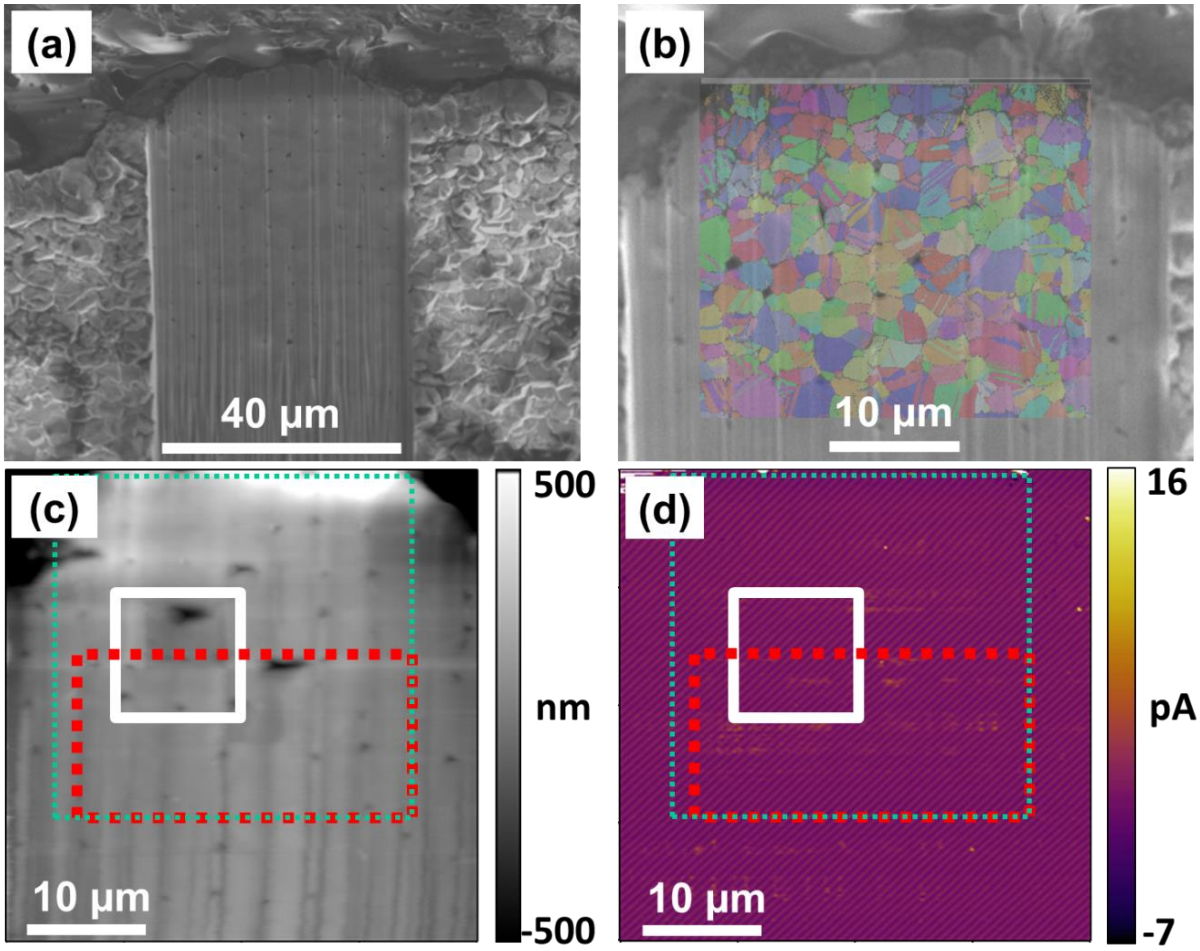

Figure 16: a) SEM image of vertical FIB shaved region smoothing the topography of as grown CdTe thin film, b)Higher magnification SEM image overlaid with EBSD data of the same smooth region, c) AFM topography image collected on the same smooth region as (b), d) simultaneous AFM photocurrent image on the same smooth region as (b).

AFM-NM of the 100 µm^2 square region overlain in Figure 16c, on the other hand, mills through the presumed FIB-induced damage layer to once again reveal striking current contrast in both dark (c) and light (d) conditions. While substantial surface roughness still remains, the properties of individual grains, and especially planar interfaces, are now apparent. More substantially, these directly vary for specific grain orientations, and strongly shift at certain grain boundaries including clear twin boundaries.

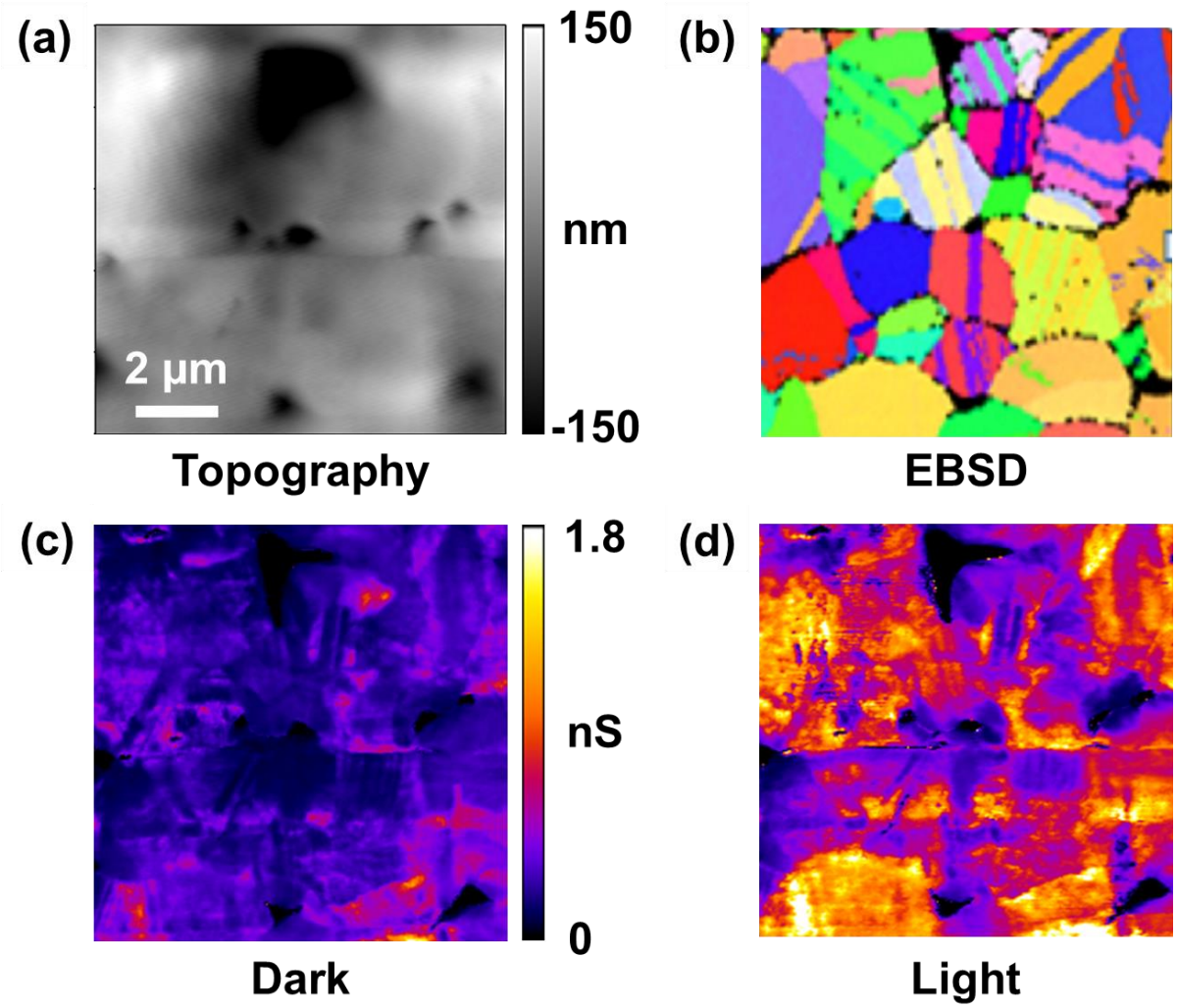

Figure 17: AFM topography (a), EBSD crystallographic orientation map (b), pcAFMs constructed conductance maps in dark (c) and upon 1.6 suns of illumination (d) of the same FIBed region presented in Figure 6a with a white square, after AFM scratching of the surface.

Figure 18 presents similar results after more thorough planarization by AFM-NM in the rectangular region overlain in Figure 16c. The AFM topography after this smoothing is shown in Figure 18a, with an RMS roughness of ~30nm (excepting pits of even greater depth). Notably this is only slightly better than the FIB-shaved surface (~45nm RMS roughness, again excepting any major pits) on average, while the I_{SC} image of Figure 18b is substantially improved

compared to Figure 16d, confirming that ion milling indeed damages the photovoltaic properties of CdTe specimens.

With even fewer topographic artifacts for this planarized surface, and possibly completely beyond the range of ion-milling induced damage, the correlations between grains, interfaces, and short circuit current are striking. The various dotted overlays guide the eye to regions of particular correlation, though similar examples abound. Planar defects are particularly apparent within the largest dotted overlay near the image centers, with I_{SC} even identifying far more interfaces than EBSD can resolve. This is either because: i) these interfaces are simple stacking faults that cannot be distinguished by EBSD and unexpectedly exhibit I_{SC} contrast, or they separate twins which are too small to spatially resolve with EBSD compared to the truly nanoscale resolution provided by AFM based measurements.

A thorough analysis of PV performance, grain orientations, and full grain boundary types and orientations is underway in separate work, necessitating AFM and EBSD images of far greater areas for statistical significance. Preliminarily, however, the short circuit current does not seem to directly correlate with any particular grain orientation. Instead, certain grain boundary compositions or orientations, along with possibly unresolved composition changes or defects within certain grains, are most likely controlling the local photovoltaic response. This is substantially mediated by the highly interconnected photoconduction pathways present in such polycrystalline films. Moreover, it may be further complicated by the possible presence of sub-surface grains (not resolved here) which additionally enhance or impede photocarrier pathways.

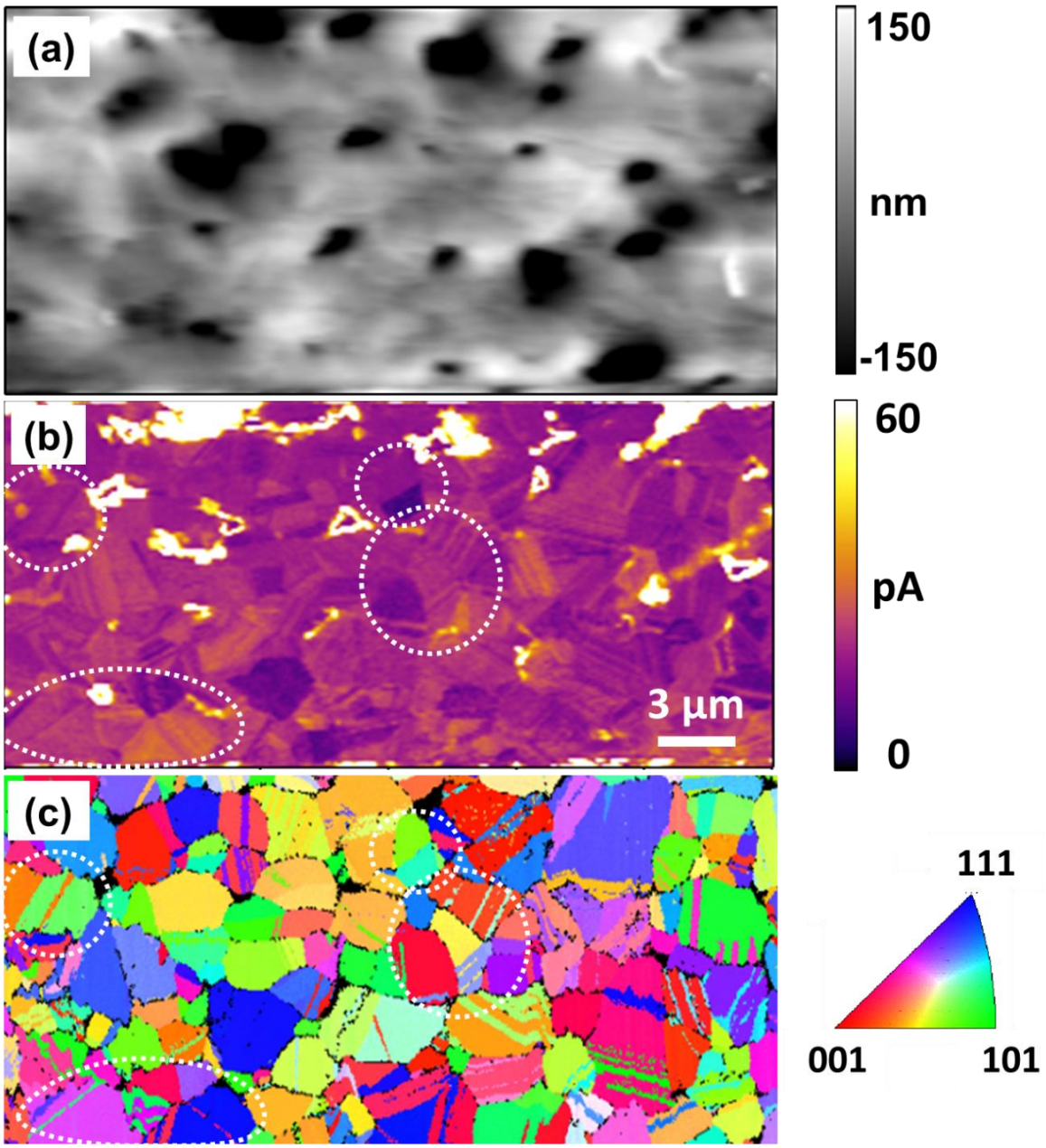

Figure 18: AFM topography (a), photocurrent (b) images of the previously FIBed, later AFM smoothed region marked by the red rectangle in Figure 16, the corresponding EBSD crystallographic orientation map (c) of the same region after collected between FIB and smoothing.

3.5 Conclusion

To conclude, constant height AFM milling is a useful technique that could replace conventional sample preparation methods in some cases. With this approach, it is possible to easily create smooth, horizontal and/or shallow angle slanted surfaces within thin films of appropriate mechanical properties. One such example is shown in the case of a CdTe thin film based solar cell, where a smooth and slanted surface is created to study the change of crucial PV performance metrics through the thickness. I_{SC} and P_{MAX} are observed to be very high at the as grown top surface and tend to deteriorate suddenly as milled beneath this surface. V_{OC} is observed to be consistent through the thickness with a slight decrease towards the bottom of the film. It is also shown that, fresh surfaces of previously FIB treated and damaged samples can be exposed with recovered electrical properties, providing very clear grain contrasts that can be easily correlated to results gained through other characterization methods such as EBSD.

3.6 References

1. Rowe, W. Brian. Principles of modern grinding technology. William Andrew, 2013.

2. Baker, M. A., et al. "A comparison of in situ polishing and ion beam sputtering as surface preparation methods for XPS analysis of PVD coatings." Thin Solid Films 377 (2000): 473-477.

3. Watt, F., A. A. Bettiol, J. A. Van Kan, E. J. Teo, and M. B. H. Breese. "Ion beam lithography and nanofabrication: a review." International Journal of Nanoscience 4, no. 03 (2005): 269-286.

4. Giannuzzi, L. A., and F. A. Stevie. "A review of focused ion beam milling techniques for TEM specimen preparation." Micron 30.3 (1999): 197-204.

5. Gozen, B. Arda, and O. Burak Ozdoganlar. "A rotating-tip-based mechanical nano-manufacturing process: nanomilling." Nanoscale research letters 5, no. 9 (2010): 1403-1407.

6. Tseng, Ampere A. "Removing Material Using Atomic Force Microscopy with Single-and Multiple-Tip Sources." Small 7, no. 24 (2011): 3409-3427.

7. Kim, Yun, and Charles M. Lieber. "Machining oxide thin films with an atomic force microscope: pattern and object formation on the nanometer scale." Science 257.5068 (1992): 375-377.

8. Tseng, Ampere A., Shyankay Jou, Andrea Notargiacomo, and T. P. Chen. "Recent developments in tip-based nanofabrication and its roadmap." Journal of Nanoscience and Nanotechnology 8, no. 5 (2008): 2167-2186.

9. Tseng, Ampere A. "Three-dimensional patterning of nanostructures using atomic force microscopes." Journal of Vacuum Science & Technology B 29, no. 4 (2011): 040801.

10. Celano, Umberto, Ludovic Goux, Attilio Belmonte, Karl Opsomer, Alexis Franquet, Andreas Schulze, Christophe Detavernier et al. "Three-dimensional observation of the conductive filament in nanoscaled resistive memory devices." Nano letters 14, no. 5 (2014): 2401-2406.

11. Justin Luria, Yasemin Kutes, Andrew Moore, Lihua Zhang, Eric A. Stach, Bryan D. Huey, "Charge Transport in CdTe Photovoltaics Revealed by Conductive Tomographic Atomic Force Microscopy", PNAS, 2015, in process

12. Rubanov, S., and P. R. Munroe. "FIB-induced damage in silicon." Journal of Microscopy 214.3 (2004): 213-221.

13. Rajsiri, Supphachan, Brian Kempshall, Stephen Schwarz, and Lucille Giannuzzi. "FIB damage in silicon: Amorphization or redeposition?."Microscopy and Microanalysis 8, no. S02 (2002): 50-51.

14. Huey, B. D., and R. M. Langford. "Low-dose focused ion beam nanofabrication and characterization by atomic force microscopy." Nanotechnology 14.3 (2003): 409.

15. Wiesendanger, Roland. Scanning probe microscopy and spectroscopy: methods and applications. Cambridge University Press, 1994.

16. Brown, N. M. D. "Scanning tunneling microscopy and spectroscopy-theory, techniques, and applications: (Edited by Dawn A. Bonnell). VCH Publishers (UK) Ltd.(1993), 436 pp. ISBN 089573-768-X." (1994): 1012-1013.

17. Jin, X., and W. N. Unertl. "Submicrometer modification of polymer surfaces with a surface force microscope." Applied physics letters 61.6 (1992): 657-659.

18. Notargiacomo, A., V. Foglietti, E. Cianci, G. Capellini, M. Adami, P. Faraci, F. Evangelisti, and C. Nicolini. "Atomic force microscopy lithography as a nanodevice development technique."Nanotechnology 10, no. 4 (1999): 458.

19. Bell, R. O. "Review of optical applications of CdTe."Revue de physique appliquee 12.2 (1977): 391-399.

20. Y. Kutes, Y. Zhou, J. L. Bosse, J. Steffes, N. P. Padture, and B. D. Huey. "Nanoscale Mapping of Photovoltaic Performance Parameters of Perovskite Solar Cells" Nano Letter, Submitted, 2015

21. Y. Kutes, B. A. Aguirre, J. L. Bosse, J. L. Cruz-Campa, D. Zubia, B. D. Huey, "Mapping photovoltaic performance with nanoscale resolution" Progress in Photovoltaics, Accepted, 2015

Chapter 4: Nanoscale Solar Cell Performance as a Function of Position and Depth through a CdTe Solar Cell by Conductive Tomographic Atomic Force Microscopy

4.1 Abstract

Microstructural defects can significantly affect the performance of polycrystalline thin film solar cell technologies. It is crucial to characterize these devices with techniques that can provide images of conduction pathways with the requisite resolution, as opposed to the common macro scale tests. Atomic force microscopy is unique in its ability to correlate local film structure with local properties. Accordingly, two recently developed AFM techniques are applied to a polycrystalline CdTe based thin film solar cell to characterize its performance metrics in a multi-dimensional fashion. Milling achieved via a diamond coated conducting AFM probed is coupled with an electronic property mapping technique that yield electrical information throughout the whole volume of a thin film, rendering subsurface features accessible. Resulting 2 and 3-d maps of the performance metrics reveal substantial variations that correlate with the thin-film microstructural features such as grains, grain-aggregates, intra-granular stacking faults and twin and grain boundaries. The insights gained into the microstructure-localized PV mechanisms from these studies are prerequisite for knowledge-driven design and optimization of these materials, leading to commercially competitive devices.

4.2 Introduction

The performance of polycrystalline solar cells is typically determined at the macroscopic scale, even though their localized dependence on the absorber microstructure has long been a concern [1-3]. The micro- and nano- scale features of typical thin film solar cells such as CdTe, CIGS, or

dye-sensitized systems make this extremely challenging, however. While many analytical and microscopy methods have contributed to the fundamental understanding of materials and microstructure for current and next generation solar cells, atomic force microscopy (AFM) methods are unique in their ability to directly measure local photovoltaic properties under standard operating conditions at the nanoscale, such as the photocurrent, carrier mobility, recombination rate, or photovoltage [4-6]. Such results have been instrumental in identifying the effect of activation treatments on the conductivity of CdTe grains and grain boundaries [7], photoinduced charging rates that may be related to external quantum efficiency measurements for polymer blend solar cells [5], high resolution maps of performance parameters for CdTe and for $MAPbI_3$ [8, 9] as well as the existence of ferroelectric domains within high quality $MAPbI_3$ films [10].

Unfortunately, AFM directly probes a surface and thus cannot typically resolve sub-surface features, which is a problem for solar cells where three dimensionally interconnected conduction networks may be crucial to the ultimate device performance. Recently, however, AFM conduction measurements have been combined with AFM-based specimen milling to test interconnects as a function of depth [11 - 13]. A photo-Conducting Tomographic variation of Atomic Force Microscopy (CT-AFM) [14] is implemented here, to investigate the photovoltaic (PV) performance of CdTe solar cells through their thickness. CT-AFM involves progressively mechanically milling into the depth of a specimen with a conductive diamond AFM probe, while simultaneously measuring the developing topography along with functional materials properties such as any photocurrents generated with in-situ illumination and/or biasing. In this study, milling is halted periodically through the depth for more extensive measurements of traditional photovoltaic performance parameters including the short circuit current (I_{SC}), true open circuit

voltage (V_{OC}), and maximum power (P_{MAX}). In this manner, the properties of an operating solar cell are uniquely measured and analyzed with nanoscale resolution in all 3 dimensions, providing a new perspective on the significant microstructural dependence of the local performance of CdTe-based thin film photovoltaics.

4.3 Materials and Methods

All AFM measurements are performed using an MFP-3D AFM (Asylum Research, Santa Barbara, CA) operated in air. Current detection is achieved with an Asylum Research ORCA cantilever holder, providing current results from 20 nA down to a noise of 1 pA. Doped conducting diamond-coated silicon probes (Nanoworld CDT-NCHR, Soquel, CA, USA) with a nominal 400 kHz resonant frequency and 80 N m^{-1} nominal spring constant are used for both mechanical milling and photocurrent collection. This system is mounted on an optical microscope (Nikon TE-2000, Melville, NY) with a 40× objective lens (Plan Achromat, 0.65 numeric aperture), enabling simultaneous photocurrent imaging from the top during illumination from below through the FTO/glass cathode. The light source is a focused, unfiltered MK-R 12 V LED (CREE, Durham, NC) with an approximate broadband illumination intensity of 1.5 $W.cm^{-2}$ (equivalent to 15 suns but not AM1.5G spectrum) as measured with a silicon reference cell calibrated separately with a 300 W Sol2A solar simulator (Oriel Instruments, Irvine, CA). Ambient light is minimized by experimenting in a dark room. However, a ~5 mW infrared (IR) super-luminescent diode (860 nm) is used by the AFM to detect probe deflection throughout the experiments. This is not expected to influence the photoconductivity measurements in any case, because the overhanging cantilever and probe essentially shadow the interrogated region of the

specimen from this continuous background of low intensity IR photons. Furthermore, the CdTe absorption edge is below 860 nm [15].

Closed-space sublimation (CSS) is used to fabricate the nearly manufacturing grade CdTe solar cells, which perform comparable to market-grade devices with a macroscopically tested open circuit voltage and efficiency of 0.8V and 12.3%, respectively. A 120 nm layer of n-type cadmium sulfide is first deposited on a fluorinated-tin oxide (FTO) coated glass substrate. A ~1.8 μm thick p-type cadmium telluride functioning as the primary light absorber is next deposited on the CdS. A common activation step follows, heat treating the cell with $CdCl_2$, without which performance is poor (very low efficiencies of ~0.1%),. A standard $CuCl_2$ treatment is next, resulting in a heavily doped CdTe 'back' surface that serves as a hole-blocking layer. The back electrode, a polycrystalline layer of carbon and nickel, is removed after macroscopic testing for AFM studies of the now exposed CdTe.

The as grown CdTe thin film surface possesses a relatively high RMS roughness on the order of ~100 nm due to varying growth rates for distinct orientations of the sub-micron-sized grains in the polycrystalline film. The specimen is therefore initially planarized over a ~30μm by 30μm field of view using AFM-based NanoMilling [16], removing as much as 300 nm from the most protruding initial structures and resulting in an rms roughness of <10 nm. This essentially eliminates the possibility of convoluting locally measured currents with topographic artifacts. Separate studies show that this process does not impair current imaging [16], and there is no discernible sub-surface damage when comparing cross-sectional TEM of as-prepared versus AFM-NM planarized regions [14].

4.4 Results and Discussion

Figure 19 outlines the basic experimental configuration, with a polycrystalline CdTe(p-type)/CdS(n-type) solar cell mounted for photoconductive AFM and/or nanomilling during simultaneous illumination from below through the transparent substrate (glass) and conducting anode (fluorinated tin oxide). Local currents (dark conditions) and/or photocurrents (during illumination) are collected by a conducting diamond coated silicon AFM probe, which serves as a milling tool, and a positionable cathode, with a contact area on the order of ~100 nm^2 maintained throughout the experiment according to the dimensions of the finest resolved features.

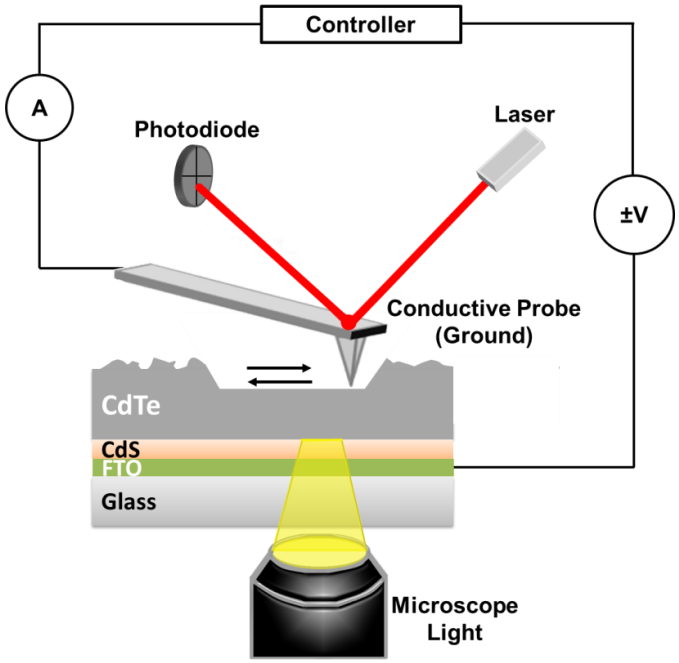

Figure 19: Schematic of a generic photoconductive AFM configuration, where the CdTe/CdS solar cell is illuminated from below through a transparent-conducting anode (FTO/glass) while measuring local current from above with the AFM probe serving as a positionable cathode. Sketch shows the CdTe absorber layer being gradually ablated frame by frame by CT-AFM while photocurrent is collected simultaneously. In between each CT-AFM ablation, pcAFMs is performed to collect local current data by the same conductive probe frame by frame as a function of applied voltage.

All PhotoConductive AFM mapping is performed with 1.5 $W.cm^{-2}$ of broadband illumination via a high intensity broadband LED, i.e. equivalent to ~15 suns (though not an AM1.5G spectrum). Although a complete study of local nonlinear absorption effects is ongoing, qualitatively the photocurrent maps are similar to those acquired with 1 sun, except with a substantially improved signal to noise ratio. Simple conductive AFM is also always completed in dark conditions after every pcAFM scan, to account for any 'background' current signal due to the semiconducting (CdTe, CdS) or even conducting (FTO) nature of the various thin film layers.

AFM-based nanomilling is achieved by applying a force on the order of ~13.2 μN during continuous scanning of a single area to progressively mill into a specimen. Tens to hundreds of images are acquired in this process, depending on the mill rate (nominally ~8 nm/frame) and target depth (2 μm here), resulting in a scan-shaped pit in the sample.

A cycle of 4 distinct experimental conditions is continually repeated for CTAFM. First, I_{SC} is directly imaged by mapping local photocurrents during illumination, without any applied bias between tip and sample (Figure 20a). Second, the same measurement is repeated in the same area (but at a slightly greater depth due to ongoing milling), with an applied tip bias of 0.7 Volts (Figure 20b). This is near the mean open circuit voltage according to macroscopic measurements of the same film, which allows efficient determination of a quasi-open circuit voltage ('qV_{OC}') based on the literally first order approximation of current being linearly proportional to bias where I_{SC} is the intercept for V=0. Each of these measurements is repeated in dark conditions as well (Figures 20c-d). Based on 216 continuous images (54 distinct depth steps), this simple procedure therefore efficiently provides dark corrected (subtracted) maps of I_{SC} (Fig 20e), and a

reasonable approximation of V_{OC} (Figure 20f), with minimal steps in depth (~40 nm for each property map) through an entire CdTe/CdS/FTO solar cell stack.

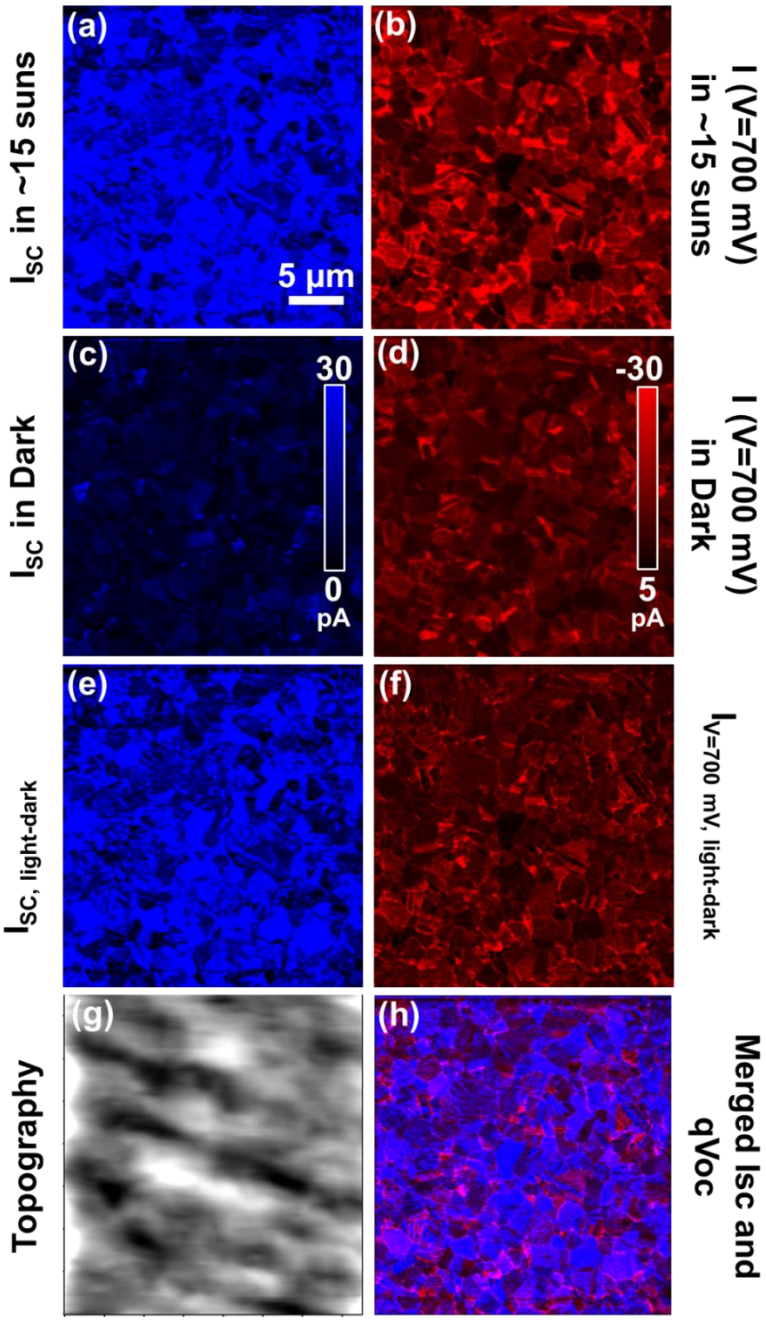

Figure 20: Representative images of I_{SC} (a) and current at V_{app}=700 mV (b) upon ~15 suns of illumination, I_{SC} (c) and current at V_{app}=700 mV (d) in dark, $I_{SC\ light} - I_{SC\ dark}$ (e) and $I_{light} - I_{dark}$ at V_{app}=700 mV (f), topography (g) and merged display of I_{SC} and qV_{OC}.

Figure 20g presents the I_{SC} superimposed with the quasi V_{OC} in a different color scheme. This uniquely reveals that these signals are in many cases complementary, particularly with grain boundaries acting as primary transport pathways near V_{OC} and grains contributing to I_{SC} with distinct but relatively homogeneous photocurrents. A high density of planar defects are also clearly resolved, in some cases apparently contributing to enhanced short circuit currents, and in many cases acting as barriers adjacent to regions with extraordinarily different open circuit voltages. Notably, these results are essentially completely decoupled from the surface topography (Figure 20h, acquired simultaneously with Figure 20a and similar but for the depth to height images corresponding to Figures 20b-d).

Figure 21 displays a 3-dimensional perspective of all 54 superimposed, dark-corrected I_{SC} and q V_{OC} images acquired while milling through the depth of the CdTe solar cell. This tomographic data volume is presented to display the initial surface, parts of the XZ and YZ cross-sections, and an oblique XYZ cross section in order to reveal the 3-dimensional nature of the measured photovoltaic properties. As with Figure 20, bright contrast signals either a high I_{SC} (blue), or a low V_{OC} (red). The images are obviously collected from top-to-bottom, until the FTO (anode) is reached. At zero bias applied to the specimen, i.e. short circuit conditions (I_{SC}), the probe injects electrons to the sample (collects holes). As with the 2-d images of just the top layer (Figure 20), I_{SC} is typically homogeneous for any given grain but varies dramatically among distinct and even adjacent grains. Sub-granular repeating band-shaped features are also clearly resolved especially for the cross-sectioned faces of the volume of data, apparently oriented according to their mother grain. Based on first principles calculations combined with HRTEM measurements, similar features were hypothesized to be closely spaced lamellar twins [17] of wurtzite structure instead of sphalerite according to cross sectional TEM [14]. Bright red regions, which represent

locations with a low quasi- V_{OC}, are observed to mostly occur at grain boundaries. This provides direct proof that grain-boundaries in CdTe serve as primary pathways for photoelectrons to transit to the n-type CdS layer, as proposed previously based on EBIC [18] and conducting AFM [19, 20].

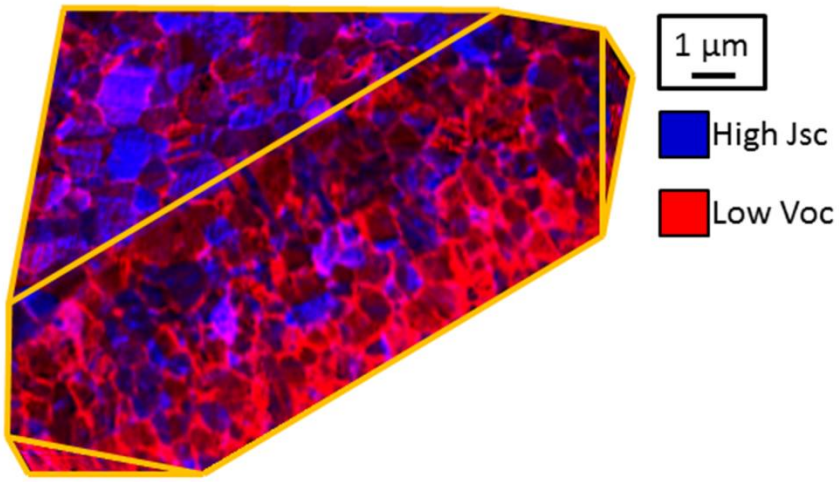

Figure 21: 3-D tomographic (CT-AFM) image of short circuit current (I_{SC}, blue) combined with simultaneously acquired quasi open circuit voltage (quasi- V_{OC}, red). Rectangular bulk is presented as sliced at an angle, exposing the interior of the volume ablated and imaged, revealing band-like stacking faults with more positive (high I_{SC}) and grain boundaries revealing a more negative (low V_{OC}) character.

Of course in reality photocurrents are not linearly proportional to the applied bias, so it is possible with more thorough experiments to more accurately determine photovoltaic properties than the quasi-V_{OC} presented above. Therefore, much more comprehensive pcAFMs measurements are reported from 3 distinct depths through the specimen [8, 16]. These are based on 42 consecutive pcAFM images in a single area, but under low load (non-milling) conditions, each with a distinct applied bias from 0 to 1V in 50 mV steps and again toggling between illuminated and dark measurements. In this manner, full dark-corrected I/V spectra are acquired

per pixel, analyzed here to determine high resolution maps of the short circuit current (I_{SC}), the true open circuit voltage (V_{OC}), and the maximum power (P_{MAX}), all at three sample depths.

Figure 22 demonstrates the first such measurement (depth A in Figure 23a), presenting I_{SC}, V_{OC} and P_{MAX} for the entire milled area. As with Figures 20 and 21, I_{SC} exhibits banded intra-granular contrast (Figure 22a). V_{OC} is more continuous within individual grains than in Figures 20 and 21, since it is more accurately determined, though once again some contrast can be correlated to grain boundaries and planar defects (Figure 22b). As the variations in V_{OC} are relatively slight compared to order-of-magnitude changes in I_{SC} for distinct microstructural features, and since according to Figures 20 and 21 they are often complementary, P_{MAX} almost mimics I_{SC} but with more extreme relative variations (Figure 21c). Figure 21d displays the correlation coefficient (R^2) representing the quality of the fitting used to calculate these 3 parameters for every single I/V curve in the 153 x 238 pixel dataset, with 88% of the fits above 0.85.

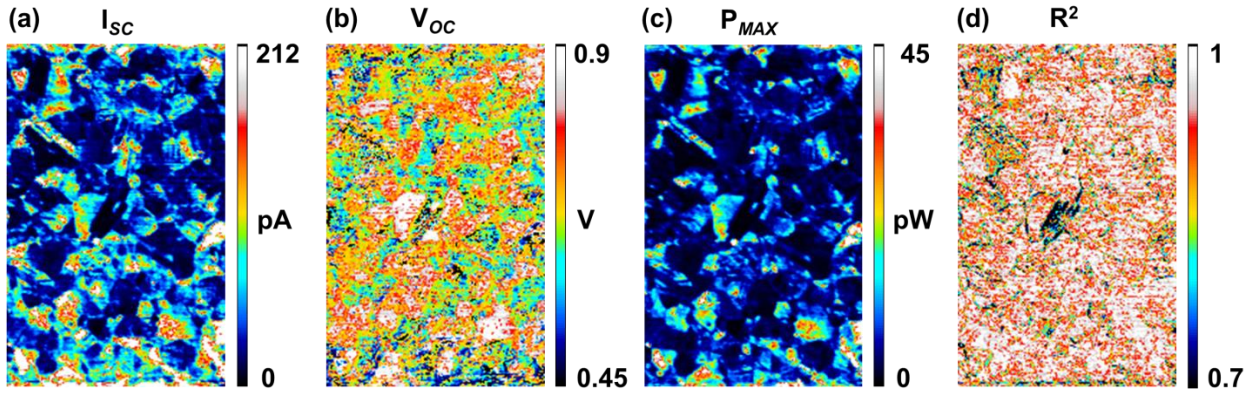

Figure 22: pcAFMs constructed maps of I_{SC} (a), V_{OC} (b) and P_{MAX} (c) for the topmost level A (~400 nm deep) over a 18 µm x 28 µm area, within the ablated CdTe thin film, along with the map of correlation coefficient R^2 (d).

Property performance maps for short circuit current, open circuit voltage and maximum power, as illustrated in Figure 22a-d, are constructed for two more distinct depths (maps not shown here)

within the CdTe film and the corresponding histograms of these maps from three distinct depths are presented in Figure 23b-d. A schematic of the ablated CdTe film as a part of the solar cell and the approximate depths at which pcAFMs is performed are shown in Figure 23a, labeled as A, B and C, respectively, as a function of increasing depth. Figure 23b presents the trend in I_{SC} versus the percent area of the scanned area as a function of depth. From this data, the top layer A is observed to have slightly lower open circuit voltage than the successive depths which show a very similar behavior to each other. Recombination of charge carriers might be a reason for the lower collected currents in the thicker film. For the rest of the film; however, thickness is observed to slightly effect I_{SC}, as the number of pixels covering higher I_{SC} values at level B, recede to lower values at level C. When this is compared to the V_{OC} histograms presented in Figure 23d, it can be deduced that the reducing photovoltage from level B to C, might be causing lower I_{SC} values. V_{OC} distributions at levels A and B are basically very similar, A is looking slightly better than B, displaying more area percentage with a larger right peak at higher V_{OC} values. Finally, when P_{MAX} distributions of A, B and C are compared, level A is clearly the winner as it displays a long tail over the highest maximum power values. The maximum power produced is observed to decreases with decreasing film thickness.

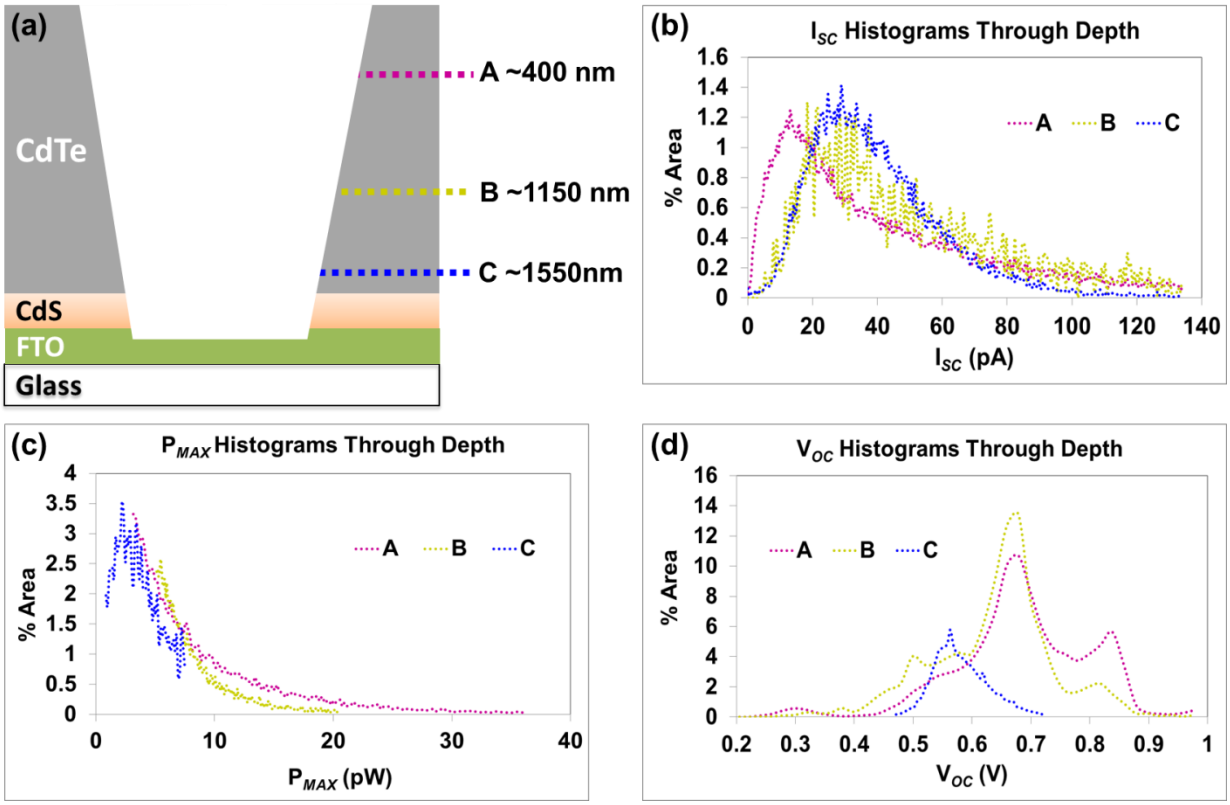

Figure 23: Schematic of the ablated CdTe thin film, shown within solar cell architecture and the corresponding approximate positions of surfaces A, B and C within the film thickness (a). Comparison of the through depth histograms of maps of I_{SC} (b), P_{MAX} (c) and V_{OC} (d), constructed at depths A, B and C via pcAFMs technique.

As mentioned earlier, the V_{OC} images that are collected during CT-AFM measurements are upon the application of a 700 mV bias to the AFM tip, which corresponds to near average (before) V_{OC} of the solar cell specimen. At this bias condition, some features such as grain boundaries are already past the open circuit conditions but the majority of the area is near-V_{OC}. By combining the I_{SC} information of each pixel from the same area, a simple linear fit is applied to each pixel since two data points on this line fit is known. By extending this line fit to cross the x-axis, a quasi-V_{OC} (qV_{OC}) value can be calculated and mapped for the same region. After the calculation

of the quasi-V_{OC} values for each pixel, 2-d histograms of I_{SC} and qV_{OC} are constructed for each frame of the CT-AFM stack for a total of 54 frames. Figure 24 demonstrates such 2-d histograms of I_{SC} in a logarithmic scale versus qV_{OC} as the y and x axes, respectively, with a color scale showing the population corresponding to each I_{SC}/V_{OC} pair. The 2-d histogram of each frame is observed to display a peak area and the behavior of this peak as a function of film thickness can be easily observed with this analysis method.

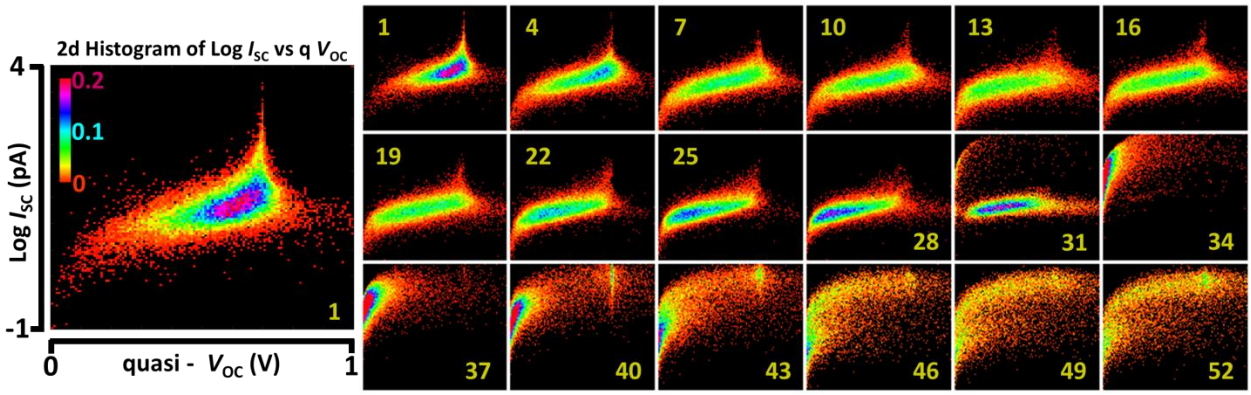

Figure 24: 2-d histogram of log I_{SC} versus quasi-V_{OC} obtained from the 1st frames of the I_{SC} / V_{OC} CT-AFM stacks, displayed larger (left) to present the corresponding x, y and z scales of the 18 frame montage of 2-d histograms of log I_{SC} vs qV_{OC} (right), taken out of a 54 frame stack.

The large 2-d histogram presented at left belongs to the 1st frames of I_{SC} /qV_{OC} CT-AFM stack and displays the x, y and z scales for the 18 frame montage shown on the left of the rest of the combined CT-AFM stack that comprises of 54 frames total. The montage starts with the first frame and goes on by skipping 2 frames at a time for the sake of saving space. Last two frames are also not included for the same purpose. The montage clearly displays the behavior of the I_{SC}/V_{OC} peak, as it moves from left to right as a function of depth. In general, a what seems to be an artifact exists in all frames of the stack, which looks like a tail right at the applied bias (V_{app} =

700 mV). The peak starts somewhere on the right, gets evenly distributed and then moves towards the left up until the 32nd frame, when the bottom electrode starts to get exposed and the measurements start to get thrown off by this highly conductive layer. The peak, along with most of the data points gets squeezed right next to the y-axis which corresponds to no photovoltage and which appears to be a high photocurrent. Though, this is just regular current from the exposed FTO, which is not dependent on illumination. The data points that are scattered along the V_{OC} axis in frame 34 on are probably remains of CdTe or CdS as the milling rate tend to be inconsistent/inhomogeneous towards the junction. The peak due to FTO fades away by showing a decrease along y-axis from frame 34 on, probably due to the milling of FTO layer as well and glass being exposed. These last frames may not be very reliable to draw conclusions from.

Figure 25a and b are separate presentations of I_{SC} (in log scale) and qV_{OC} of the peak, respectively, followed in Figure 24 as a function of depth. Each graph is composed of 54 data points that correspond to 54 ablated layers/frames, presented along with calculated standard deviations. As also observed in Figure 6, exposing of FTO layer at frame 32 causes the apparent short circuit levels to rise abruptly. This also corresponds to the drastic fall of qV_{OC} at frame 32, observed in Figure 25b. Overall, calculated qV_{OC} tends to decrease with film thickness, whereas the short circuit current stays level until FTO is exposed.

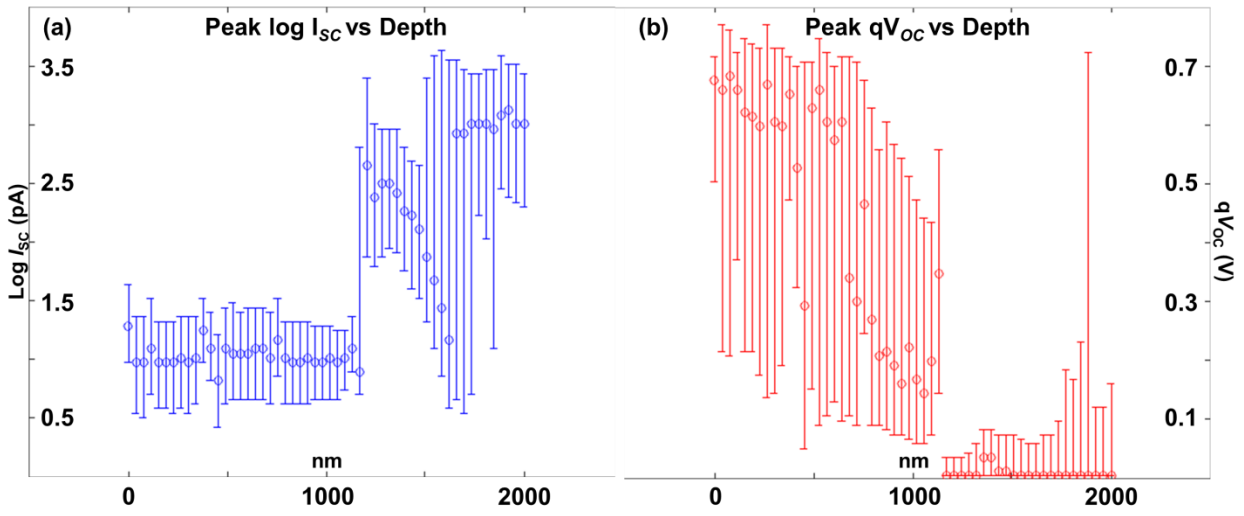

Figure 25: Graphs of I_{SC} (a) and qV_{OC} (b) of the peak population, respectively, as a function of depth.

4.5 Conclusion

In summary, the photovoltaic performance of a CdTe thin film is investigated by multi-parametric approaches made available by two recently developed AFM techniques; namely CT-AFM and pcAFMs. CT-AFM measurements uniquely revealed the 3-d microstructure and electrical behavior throughout the volume of a CdTe film, revealing a high density of intra-grain, planar features that are observed to be good hole transport channels. Same technique revealed the role of grain boundaries near open circuit condition as electron pathways. pcAFMs applied at three distinct depths in between CT-AFM measurements provided nanoscale maps of PV performance parameters as a function of depth revealing trends that could be used for absorber layer thickness optimization. Finally, an efficient way to calculate qV_{OC} values is presented and 2-d histograms of peak I_{SC}/V_{OC} are investigated as a function of depth, which can closely be related to power generation trends of the cell as a function on absorber material thickness.

Overall, the insights gained into the microstructure-localized PV mechanisms from these studies are prerequisite for knowledge-driven design and optimization of these materials, leading to commercially competitive devices.

4.6 References

1. Sites, James R., J. E. Granata, and J. F. Hiltner. "Losses due to polycrystallinity in thin-film solar cells." *Solar energy materials and solar cells*55, no. 1 (1998): 43-50.
2. Li, H., et al. "Enhanced electrical properties at boundaries including twin boundaries of polycrystalline CdTe thin-film solar cells." *Physical Chemistry Chemical Physics* 17.17 (2015): 11150-11155.
3. Al-Jassim, M. M., Y. Yan, H. R. Moutinho, M. J. Romero, R. D. Dhere, and K. M. Jones. "TEM, AFM, and cathodoluminescence characterization of CdTe thin films." *Thin Solid Films* 387, no. 1 (2001): 246-250.
4. Coffey, David C., and David S. Ginger. "Time-resolved electrostatic force microscopy of polymer solar cells." Nature materials 5, no. 9 (2006): 735-740.
5. Coffey, David C., Obadiah G. Reid, Deanna B. Rodovsky, Glenn P. Bartholomew, and David S. Ginger. "Mapping local photocurrents in polymer/fullerene solar cells with photoconductive atomic force microscopy." Nano letters 7, no. 3 (2007): 738-744.
6. Hoppe, H., Th Glatzel, M. Niggemann, A. Hinsch, M. Ch Lux-Steiner, and N. S. Sariciftci. "Kelvin probe force microscopy study on conjugated polymer/fullerene bulk heterojunction organic solar cells." Nano letters 5, no. 2 (2005): 269-274.
7. Moutinho, H. R., R. G. Dhere, C-S. Jiang, M. M. Al-Jassim, and L. L. Kazmerski. "Electrical properties of CdTe/CdS solar cells investigated with conductive atomic force microscopy." Thin Solid Films 514, no. 1 (2006): 150-155.
8. Y. Kutes, B. A. Aguirre, J. L. Bosse, J. L. Cruz-Campa, D. Zubia, B. D. Huey, "Mapping photovoltaic performance with nanoscale resolution" Progress in Photovoltaics, Accepted, 2015
9. Y. Kutes, Y. Zhou, J. L. Bosse, J. Steffes, N. P. Padture, and B. D. Huey. "Nanoscale Mapping of Photovoltaic Performance Parameters of Perovskite Solar Cells" Nano Letter, Submitted, 2015
10. Kutes, Yasemin, Linghan Ye, Yuanyuan Zhou, Shuping Pang, Bryan D. Huey, and Nitin P. Padture. "Direct observation of ferroelectric domains in solution-processed $CH_3NH_3PbI_3$ perovskite thin films." The Journal of Physical Chemistry Letters 5, no. 19 (2014): 3335-3339.
11. Celano, Umberto, Ludovic Goux, Karl Opsomer, Martina Iapichino, Attilio Belmonte, Alexys Franquet, Ilse Hoflijk, Christophe Detavernier, Malgorzata Jurczak, and Wilfried Vandervorst. "Scanning probe microscopy as a scalpel to probe filament formation in conductive bridging memory devices." Microelectronic Engineering 120 (2014): 67-70.
12. Celano, Umberto, and Wilfried Vandervorst. "Scaning probe tomography for advanced material characterization." In Integrated Reliability Workshop Final Report (IIRW), 2014 IEEE International, pp. 1-5. IEEE, 2014.

13. Celano, Umberto, Ludovic Goux, Attilio Belmonte, Guido Giammaria, Karl Opsomer, Christophe Detavernier, Olivier Richard et al. "Progressive vs. abrupt reset behavior in conductive bridging devices: A C-AFM tomography study." In Electron Devices Meeting (IEDM), 2014 IEEE International, pp. 14-1. IEEE, 2014.
14. Justin Luria, Yasemin Kutes, Andrew Moore, Lihua Zhang, Eric A. Stach, Bryan D. Huey, "Charge Transport in CdTe Photovoltaics Revealed by Conductive Tomographic Atomic Force Microscopy", PNAS, 2015, In process
15. Bell, R. O. "Review of optical applications of CdTe."Revue de physique appliquee 12.2 (1977): 391-399.
16. Y. Kutes, J. Luria, B. D. Huey, "Nanoscale Planarization, Cross Sectional Milling, and Electrical Characterization of CdTe Thin Films via Atomic Force Microscopy", - ACS Nano, 2015 – In preparation
17. Yan, Y., M. M. Al-Jassim, K. M. Jones, S-H. Wei, and S. B. Zhang. "Observation and first-principles calculation of buried wurtzite phases in zinc-blende CdTe thin films." Applied Physics Letters 77, no. 10 (2000): 1461-1463.
18. Li, Chen, Yelong Wu, Jonathan Poplawsky, Timothy J. Pennycook, Naba Paudel, Wanjian Yin, Sarah J. Haigh et al. "Grain-boundary-enhanced carrier collection in CdTe solar cells." Physical review letters 112, no. 15 (2014): 156103.
19. Visoly-Fisher, Iris, Sidney R. Cohen, and David Cahen. "Direct evidence for grain-boundary depletion in polycrystalline CdTe from nanoscale-resolved measurements." Applied physics letters 82, no. 4 (2003): 556-558.
20. Li, H., X. X. Liu, Y. S. Lin, B. Yang, and Z. M. Du. "Enhanced electrical properties at boundaries including twin boundaries of polycrystalline CdTe thin-film solar cells." Physical Chemistry Chemical Physics 17, no. 17 (2015): 11150-11155.

Chapter 5: Nanoscale Mapping of Photovoltaic Performance Parameters of Perovskite Solar Cells

5.1 Abstract

Perovskite solar cells (PSCs) based on thin films of organolead trihalide perovskites (OTPs) hold unprecedented promise for low-cost, high-efficiency photovoltaics (PVs) of the future. While PV performance parameters of PSCs, such as short circuit current (I_{SC}), open circuit voltage (V_{OC}), and maximum power (P_{MAX}), are always measured at the macroscopic scale, it is necessary to probe those parameters at the nanoscale to gain key insights into the fundamental PV mechanisms and their localized dependence on the OTP thin-film microstructure. Here we have used photoconductive atomic force microscopy spectroscopy (pcAFMs) to create, for the first time, nanoscale-resolution maps of PV performance parameters of planar PSCs based on methylammonium lead triiodide ($CH_3NH_3PbI_3$ or $MAPbI_3$) thin films. These maps reveal substantial variations in the PV performance parameters that correlate with the thin-film microstructural features such as intra-grain planar defects, grains, grain-aggregates, and the interfaces between them. The insights gained into the microstructure-localized PV mechanisms from these studies are essential for guiding the microstructural tailoring of OTP films for improved bulk PV performance in future PSCs.

5.2 Introduction

Perovskite solar cells (PSCs) that use solution-processed hybrid organolead trihalide perovskites (OTPs) as thin-film light absorbers are of tremendous interest of late [1-5]. The unprecedented rise in the power conversion efficiency (PCE) of PSCs from 3.8 % [4] to 20.1 % [5] within a short period of time (six years), and the promise of low-cost fabrication of PSCs, is fueling this

interest. The most well-studied OTP for PSCs is methylammonium lead triiodide ($CH_3NH_3PbI_3$ or $MAPbI_3$), which is relatively easy to solution-process. $MAPbI_3$ thin films in planar PSCs are typically polycrystalline, with average grain sizes ranging from a hundred nanometers to a few microns [6-8]. $MAPbI_3$ belongs to a class of 'soft' organic-inorganic hybrid perovskites that have low formation energy [9], and depending on the solution-processing method used to deposit the thin films are known to have variable crystallinity and defect concentration within grains [6, 7, 10 – 12]. In fact, within the same $MAPbI_3$ thin film there can be grain-to-grain variability in crystallinity, defect concentrations, and orientation [7, 13-15]. Consequently, the local properties of $MAPbI_3$ thin films are likely to be variable at the microstructure level, which in turn is likely to influence the local photovoltaic (PV) performance parameters. However, the measurement of PV performance parameters is invariably performed at the macroscopic scale, on areas ranging from ~0.1 to ~1 cm^2 [7], which essentially averages the local variability in the $MAPbI_3$ properties at the microstructure level. While several scanning probe methods, such as Kelvin probe force microscopy (KPFM) [7, 16, 17, 18], conductive atomic force microscopy (cAFM) [18], and piezoresponse force microscopy (PFM) [19], have been used to characterize the local properties of $MAPbI_3$ thin films, direct local measurements of PV performance parameters at the nanoscale are lacking. These measurements are likely to provide key insights into the local microstructural effects on the PV performance, and are essential for guiding the microstructural tailoring of OTP films for high-efficiency PSCs of the future.

In this context, photoconductive AFM spectroscopy (pcAFMs) is an ideal tool for probing local PV response at the nanoscale. The pcAFMs technique is based on AFM, and it leverages the nanoscale conductance mapping (NCM) [20] technique. NCM operates similar to continuous imaging tunneling spectroscopy (CITS) [21], where a sequence of conductive AFM images in a

single region are acquired, each at a distinct voltage within a current (*I*) - voltage (*V*) range of interest. Extended to photoconduction measurements by simultaneous specimen illumination, this approach allows the acquisition of solar-cell *I-V* data efficiently with true nanoscale spatial resolution [22]. Here, pcAFMs is applied to planar PSCs based on $MAPbI_3$ perovskite thin films to map, for the first time, the crucial PV performance parameters — short-circuit current (I_{SC}), open-circuit voltage (V_{OC}), and maximum power point (P_{MAX}) — at the nanoscale, revealing profound inter- and intra-granular variations in the local PV properties of PSCs.

5.3 Materials and Methods

For the fabrication of the film sample, fluorinated tin oxide (FTO)-coated glass was patterned using HCl-(25%)-etching with Zn powder, and cleaned by soaking in a basic bath (5 wt % NaOH in ethanol) overnight. After washing with deionized water and ethanol, a compact TiO_2 electron-transport layer (ETL) was deposited on top of the patterned FTO/glass by spray pyrolysis at 450 ˚C. The perovskite thin film deposition method is based on procedures reported previously [7, 23]. A 42 wt% precursor solution of MAI (Dyesol, Queanbeyan, Australia) and PbI_2 (Acros Organics, Pittsburgh, PA) (MAI: PbI_2 = 1:1, molar ratio) was prepared by dissolving the mixture in a mixed solvent of 1-N-methyl-2-pyrrolidinone (NMP):γ-butyrolactone (GBL) (7:3, by weight). The precursor solution was then spin-coated on the compact TiO_2-coated FTO/glass at 4500 rpm for 10 s. The substrates were immediately transferred into a stirring diethyl ether (Fisher Chemical, Pittsburgh, PA) bath for 2 min. The film was then taken out and dried rapidly by using a nitrogen jet. The as-dried film was then thermally annealed at 150 °C for 5 min in nitrogen atmosphere, and it was characterized soon after.

Figure 26 is a schematic diagram showing a planar PSC mounted in a pcAFMs configuration for measuring local PV performance parameters during illumination from the bottom through the transparent-conducting cathode (FTO/glass). The compact TiO_2 serves as the ETL, and the conductive AFM probe serves as the anode. The hole-transport layer (HTL) is absent in this PSC configuration. The displayed surface topography is a 3-D representation of a 3 μm × 3 μm region of the $MAPbI_3$ films, acquired by contact mode AFM, revealing a smooth but polycrystalline morphology with a root-mean-square (RMS) roughness of ~6.6 nm.

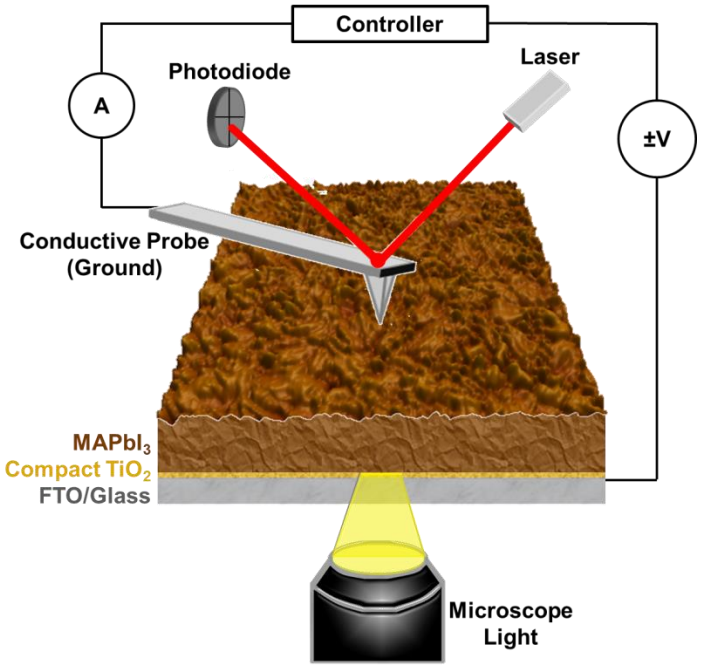

Figure 26: Schematic diagram of the pcAFMs configuration, where the PSC is illuminated from below through a transparent-conducting cathode (FTO/glass) while measuring local current with a positionable conductive AFM probe anode from above. This diagram includes a 3-D rendered, 3 μm × 3 μm, topographic AFM image of a $MAPbI_3$ perovskite thin film, along with a schematic cross section of the PSC containing a compact TiO_2 ETL, but no HTL.

All pcAFMs measurements were performed using an MFP-3D AFM (Asylum Research, Santa Barbara, CA) operated in air. Current detection was achieved with an Asylum Research ORCA

cantilever holder, providing current results from 20 nA down to a noise floor of ~1 pA. Conducting PtIr-coated silicon probes (Bruker, Billerica, MA) with a work function of ~5 eV, a nominal resonant frequency of 13 kHz, and a nominal spring constant of 0.2 $N.m^{-1}$ were employed for all AFM measurements. This system is mounted on an optical microscope (Nikon TE-2000, Melville, NY) with a 40× objective lens (Plan Achromat, 0.65 numeric aperture), enabling simultaneous pcAFMs imaging from the top during illumination from below through the FTO/glass cathode. The light source is a focused, unfiltered MK-R 12 V LED (CREE, Durham, NC) with an approximate illumination intensity of 0.07 $W.cm^{-2}$ (equivalent to 0.7 suns but not AM1.5G spectrum) as measured with a silicon reference cell calibrated separately with a 300 W Sol2A solar simulator (Oriel Instruments, Irvine, CA). Ambient light is minimized by experimenting in a dark room. However, a ~5 mW infrared (IR) super-luminescent diode (860 nm) is used by the AFM to detect probe deflection throughout the experiments. This is not expected to influence the photoconductivity measurements, because the overhanging cantilever and probe partially shadow the interrogated region of the specimen from this continuous background of low intensity IR photons. Furthermore, the $MAPbI_3$ absorption edge is well below 860 nm [24, 25].

5.4 Results and Discussion

Figure 27a is a 3 μm x 3 μm AFM image (contact mode) showing the representative smooth surface topography for the $MAPbI_3$ thin film. Bright and dark contrast indicates protrusions and depressions in the range ±15 nm, respectively, revealing an overall root mean square (RMS) roughness of ~5 nm and grain sizes up to ~500 nm, with 'wrinkled' surfaces suggesting faceting and/or intersection of planar defects (twins, stacking faults) with the surface. Figures 2b and 2c

are I_{SC} contrast images of the same area (same current scale), in dark and under light, respectively, showing significant differences. While the distribution of dark- I_{SC} is homogeneous and essentially negligible (<10 pA), the light- I_{SC} distribution is remarkably location dependent and heterogeneous.

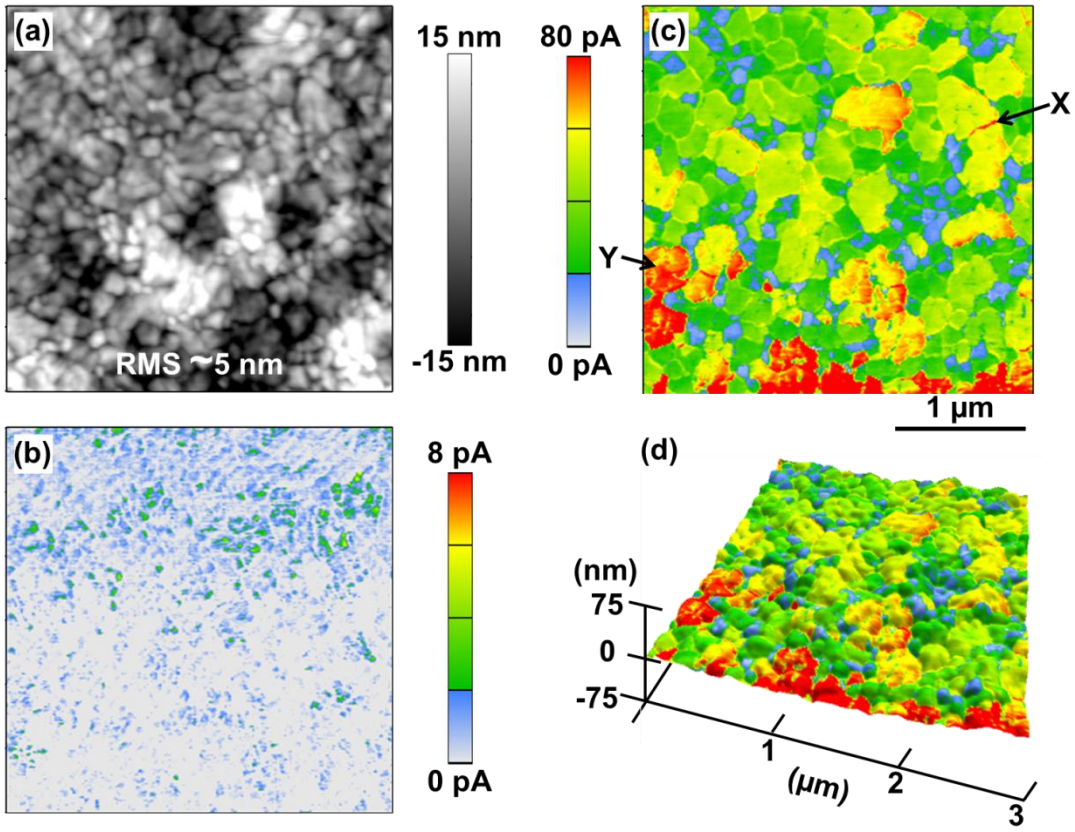

Figure 27: 2-D images of 3 µm × 3 µm region of a HTL-free $MAPbI_3$-based planar PSC (same magnification): (a) topography, (b) dark I_{SC}, and (c) I_{SC} under 0.07 $W.cm^{-2}$ illumination. (d) 3-D representation of the topography, overlaid by the I_{SC} color contrast collected over the same area, revealing the microstructure-specific response. Same current scale for (c) - (d).

To better visualize the highly granular I_{SC} response under light, the current image of Fig. 27c is overlaid on a 3-D map of the topography (Fig. 27d) using the same color contrast as in Fig. 27c. These images (Figs. 27c-27d) demonstrate clearly the heterogeneity of the I_{SC} distribution across

the area, and highlight the remarkable fact that only about half of the PSC area generates most of the I_{SC}. Individual grains with different crystallographic orientations having different I_{SC} is understandable considering anisotropy in absorption, transport, and/or band alignment, along with the non-textured (random) nature of the $MAPbI_3$ perovskite grains for the thin films studied here [7]. However, closer inspection of Figs. 27c-27d reveals that interconnected aggregates of several adjacent grains, not just individual grains, exhibit similar low (blue) or high (orange/yellow) I_{SC}. Moreover, there is little or no gradient in these I_{SC} values within individual grains or grain-aggregates. This indicates that photocarriers are sufficiently mobile, and that the electron-hole recombination is minimized, to laterally traverse up to ~500-nm without significant scattering or degradation in the carrier concentration.

On the other hand, transport is clearly hindered by certain boundaries between grains or grain-aggregates, which effectively funnels current through local high-conductivity regions comprising certain interconnected grains, grain boundaries, and/or other planar defects. The grain boundary identified as region X in Fig. 27c is one such example with an enhanced I_{SC}, as compared to the adjacent grains exhibiting lower I_{SC}. Conversely, Region Y exhibits a lower I_{SC} compared to the surrounding area. This opposing behavior is observed despite similar topographic depressions at each location, suggesting that topography-related artifacts, which must always be considered in AFM-based measurements, are negligible in this case. Instead, some grain boundaries and/or buried interfaces simply act as effective barriers to transport. Other interfaces serve as low-resistance collectors for photocarriers generated within individual grains and/or interconnected grain-aggregates, essentially gathering photocarriers from throughout the surrounding area. This highlights an important area for future fundamental research, isolating and identifying the

character and composition of beneficial as well as detrimental current pathways in order to engineer improved performance in PSCs.

This hypothesis of a network of low- and high-conductivity channels, coupled with high carrier mobilities and/or diffusion lengths, is further supported by the general observation that apparently smaller grains or grain-aggregates in Fig. 27c exhibit a relatively low I_{SC} response of 5-30 nA (blue). The discrete I_{SC} for larger areas rises through 30-60 pA (red), and up to 60-80 pA (orange/yellow) as their size approaches ~500 nm. Thus, when the conducting AFM probe (anode) is positioned within any of these regions of uniform but unique I_{SC}, it is likely that the measured signal represents a significant fraction of the photoconduction throughout the entire grain-aggregate, dictated by the surrounding interconnected low- and high-conductivity channels.

The heterogeneous photocurrent response for $MAPbI_3$ is further exemplified in Fig. 28 in individual *I-V* spectra (Fig. 28a) acquired for grains with distinctly different I_{SC} values: A (red), B (yellow), and C (blue). The locations are identified on topography (Fig. 28b) and I_{SC} maps (Fig. 28c), where these maps were acquired in a manner similar to that in Fig. 27, but at a different location on the same PSC. The *I-V* curves were recorded by measuring the current, while sweeping the probe bias between ±1 V in voltage steps of ~5.7 mV, both in dark (dotted) and under light (solid). Little variation in the dark current is observed in Fig. 28a, similar to what is seen in Fig. 27b. Upon illumination of the $MAPbI_3$ film, though, there are substantial grain-to-grain variations, not just in I_{SC}, but also in the apparent V_{OC} and fill factor (*FF*).

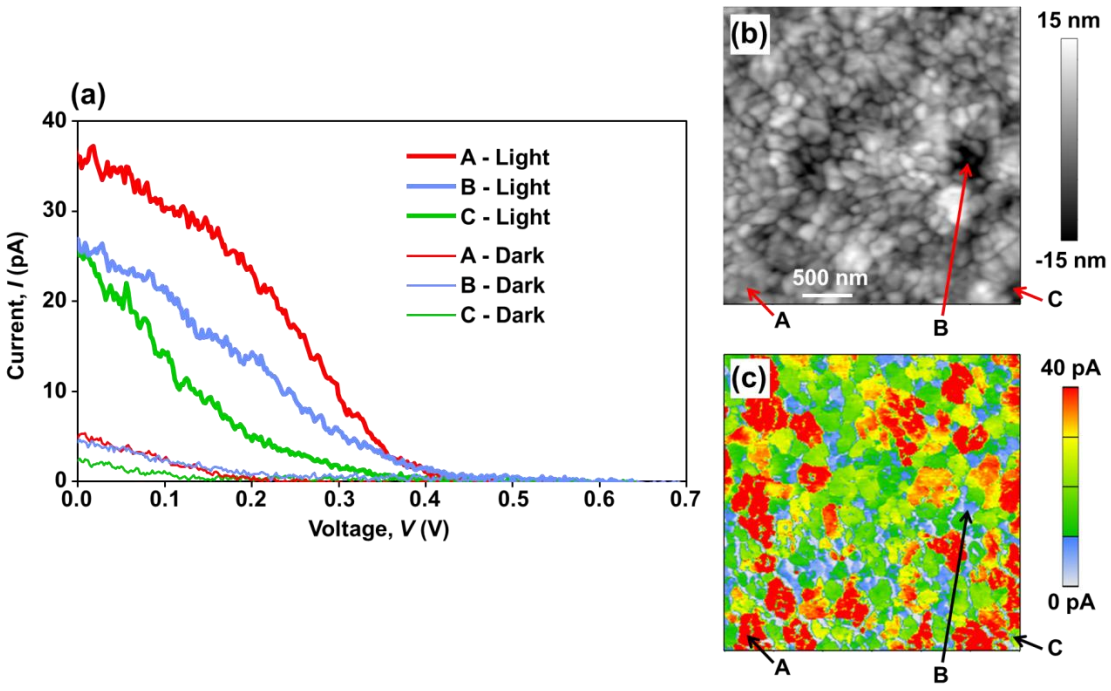

Figure 28: (a) Current measurements as a function of applied bias from +1 to 0 V in light and dark conditions for grains marked A, B and C in (b) AFM topographic image and (c) I_{SC} map of the same area.

To map these critical PV performance parameters more precisely, Fig. 29 presents 15 consecutive pcAFMs current maps from a different region (2.86 µm × 2.61 µm) in the same PSC. All images were acquired during ~0.07 W.cm^{-2} illumination, but each at different bias voltage, between 0 and 700 mV (well beyond V_{OC}) in steps of 50 mV as indicated. Repeating each voltage condition twice, once for dark and once for light conditions, ultimately required 128 minutes to collect all 30 images (256 lines per image, 1 Hz line rate). To better visualize the progression of the current response as the PSC locally approaches open-circuit conditions (typically 200-400 mV), image contrast for the entire montage is displayed in a logarithmic scale representing 0.01-100 pA. A maximum photocurrent of 93 pA is detected for short circuit

condition (0 mV), while beyond V_{OC} the current polarity becomes negative as expected but is not shown here since this is beyond the range of normal solar cell operation.

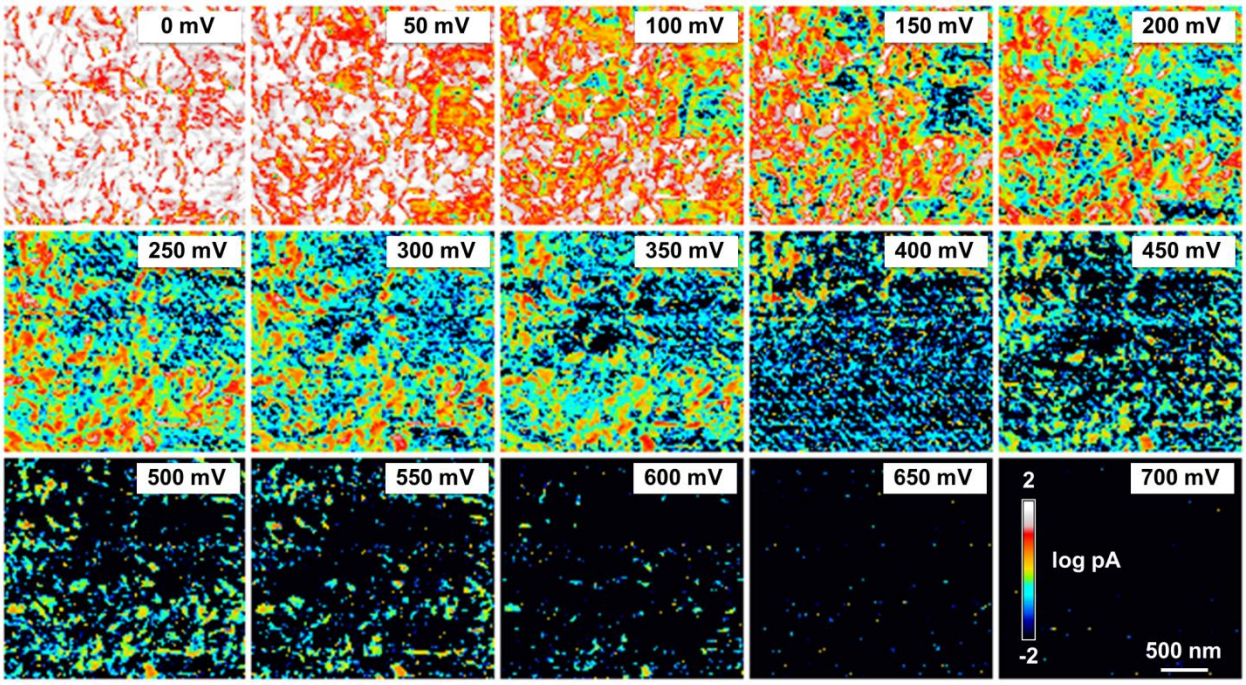

Figure 29: Montage of pcAFMs current images, all for the same 2.86 µm × 2.61 µm area during ~0.07 W.cm^{-2} illumination, but each at distinct applied voltages as labeled. Note the logarithmic current scale, representing currents from 0.01 pA (black) to 100 pA (white).

It is acknowledged that the measured currents may diminish as a function of bias and/or imaging time, due to unspecified damage either at the local position being probed or elsewhere along the 3-d complex transport network. To address this concern, Fig. 30 presents the simultaneously acquired height for the 15 frames in Fig. 29. There is no topographic damage except a barely visible smoothening (the RMS roughness smoothly shifts from 8.98 nm to 8.48 nm, *i.e.* <5.6%, across the entire montage), which is common in repeated AFM imaging and generally indicates gradual, minor surface and/or probe wear. Of course, electrochemical reactions, current induced heat, or ambient exposure could cause additional effects, but such issues are usually

accompanied by substantial changes in $MAPbI_3$ topography and the photovoltaic performance [26, 27], which clearly are not observed here.

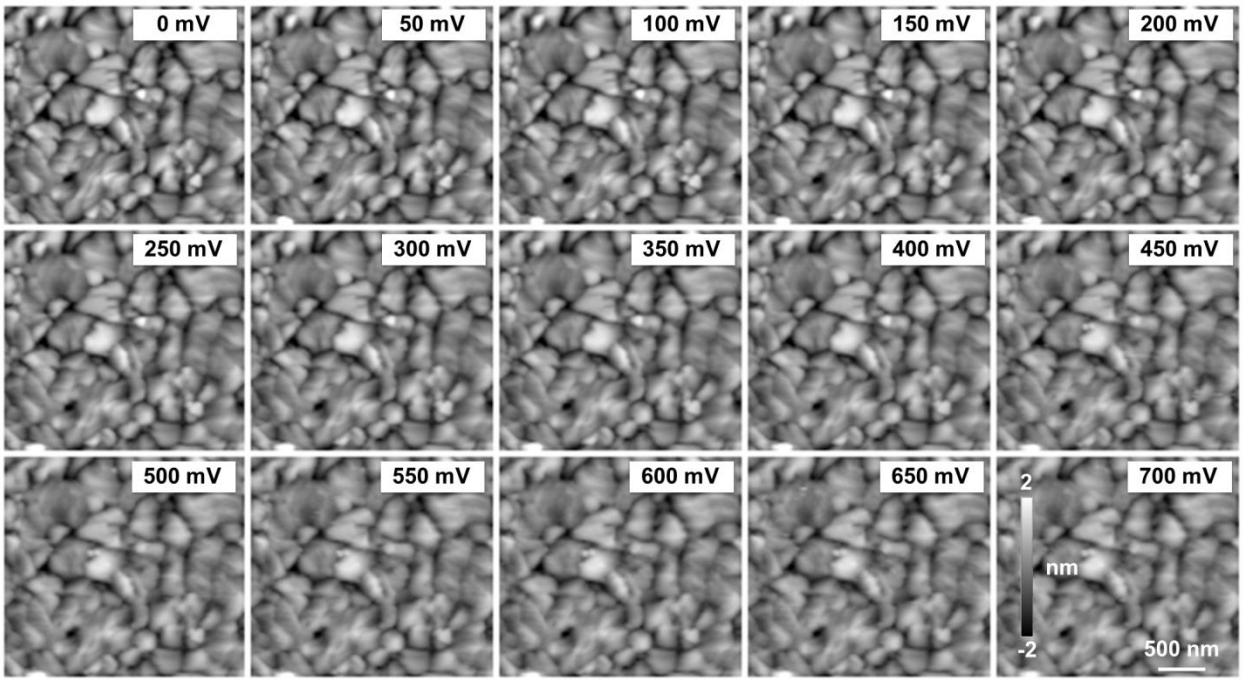

Figure 30: Montage of AFM height images at different applied bias voltages as labeled throughout the photocurrent measurements during ~0.07 W.cm^{-2} illumination, revealing negligible topographic damage throughout the ~2-h experiment.

Figure 31a redisplays the first topography image from Fig. 5 (0 mV), alongside maps of I_{SC} (Fig. 31b), V_{OC} (Fig. 31c), and P_{MAX} (Fig. 31d) for direct comparison. These maps of PV performance parameters are calculated from Fig. 29 by fitting the measured current (image contrast) versus applied voltage (image frame) with a 4th order polynomial at every image pixel in the pcAFMs dataset. The correlation coefficient R^2 is also mapped (Fig. 31e), evidencing reasonable fits. This approach provides up to 256 × 256 *I-V* curves [22] for the 3 μm × 3 μm images acquired here. After cropping edge pixels that drifted out of the field-of-view as a result of inevitable but minor thermal drift during the experiment, this reduced to 244 × 223 pixels (2.86 μm × 2.61 μm) of

fully resolved *I-V* spectra, and hence a total of 54,412 individual *I-V* curves.

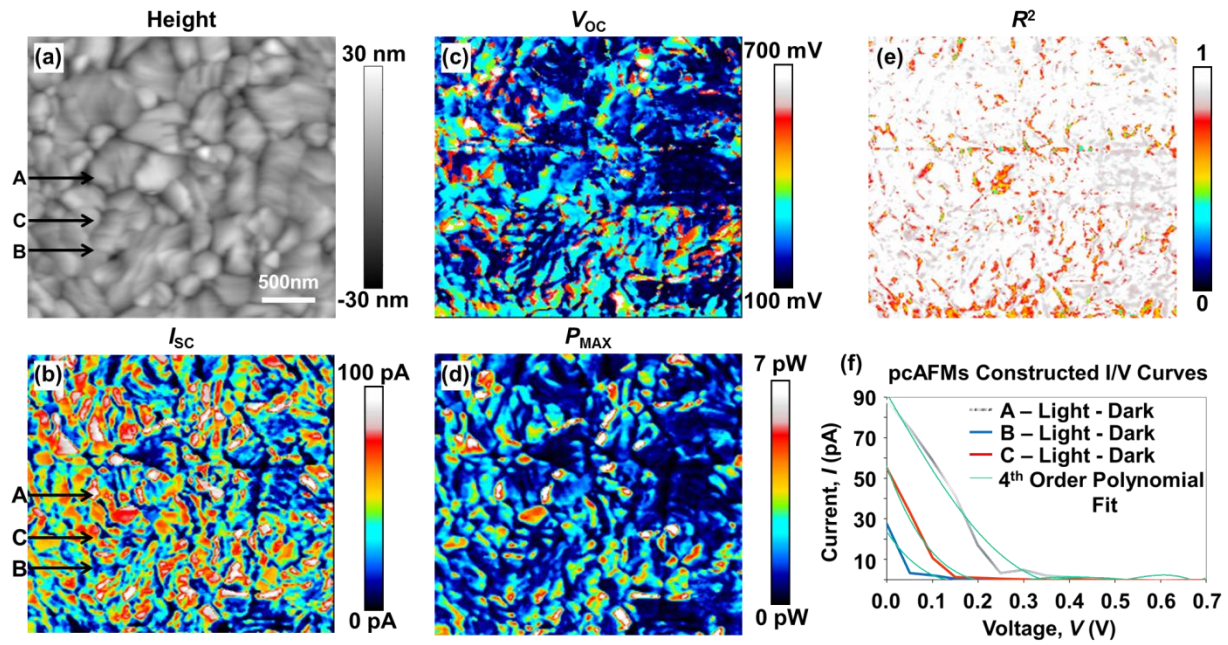

Figure 31: (a) Topography (height), and pcAFMs resolved maps of (b) I_{SC}, (c) V_{OC}, and (d) P_{MAX} on a 2.86 µm × 2.61 µm area upon ~0.07 W.cm^{-2} illumination when the PSC is biased. (e) The R^2 correlation coefficient map provides the measure of the quality of the polynomial fitting of the *I-V* data. (f) Three such *I-V* curves and their fits are shown for representative spots A, B, and C, marked in (a) and (b) taken from 54,412 total spectra in this pcAFMs experiment.

It is noteworthy that Figure 31 is based on data comparable to the conventionally acquired *I-V* curves shown in Figure 28, but is more efficient and at nanoscale spatial resolution, necessary for visualizing the fine spatial variations in the local PV performance of $MAPbI_3$-PSCs and other nanostructured photovoltaics. For example, representative pcAFMs-based *I-V* curves are shown from three different locations in Figure 31f, along with their corresponding 4th order polynomial fits. Of course, these curves are under-sampled in the voltage domain compared to the point-by-point *I-V* spectra presented in Figure 28 (by a factor of 8.8). However, the relatively smooth *I-V* response measured at any given location, as opposed to the abrupt changes in photovoltaic performance for features with nanoscale separations (*e.g.* adjacent grains or grain boundaries),

strongly justifies prioritizing spatial resolution over the number of voltage steps. Naturally, even higher fidelity *I-V* data could be acquired with more images (smaller voltage increments), and more sophisticated fitting/modeling schemes could be implemented, but the results presented herein demonstrate a reasonable balance for these first direct measurements of the PV performance parameters of PSCs at the nanoscale.

Analyzing the images in Figure 31 yields a mean I_{SC} of 38 pA, V_{OC} of 256 mV, and P_{MAX} of 2 pW, with good fitting (R^2>0.90) over more than 70% of the image. There is apparently a weak correlation between strong I_{SC} and high V_{OC}, whereas P_{MAX} essentially mirrors the I_{SC} contrast. Of course, these data cannot be directly compared with macroscopically measured PV performance parameters of $MAPbI_3$-based PSCs in the literature because those PSCs typically have a HTL and standardized measurements are performed under 1 sun (0.1 $W.cm^{-2}$, simulated AM1.5G solar spectrum). Nevertheless, Figure 31 is telling as it exhibits both a highly granular PV response, as well as grain-aggregates that are very photoactive frequently observed adjacent to others with poor performance. This evidences grain and/or grain-aggregate localization of low-resistance current pathways, not just for I_{SC} conditions as demonstrated with Figs. 27 and 28, but also throughout the power-generating *I-V* quadrant.

Furthermore, the film topography (Figure 31a) reveals that most grains, especially larger ones, comprise regular striations aligned in distinct orientations within any given grain. Such microstructural features are often reported in $MAPbI_3$ perovskite thin films [7, 8]. The corresponding I_{SC} and V_{OC} maps, when overlaid as color contrast on height maps as in Figs. 32a and 32b, respectively, often couples with these band-like features. In particular, the photovoltaic performance is regularly diminished at surface steps or depressions within grains. These often

periodic, band-like structures are hypothesized to represent the terminations of planar defects (twins, stacking faults) at the surface of grains. The V_{OC} behavior does not appear to correlate as strongly with these striations as I_{SC} does, though some are visible in the lower left of Fig. 32b. While an apparent decrease in I_{SC} and V_{OC} at deep topographic crevices like some grain boundaries is likely a common AFM artifact related to the contact area between the probe and the sample, the intra-granular contrast suggests distinctly different photovoltaic activity (in this case diminished) at planar defects, similar to recent results reported for CdTe [28, 29], and other polycrystalline solar cells [30].

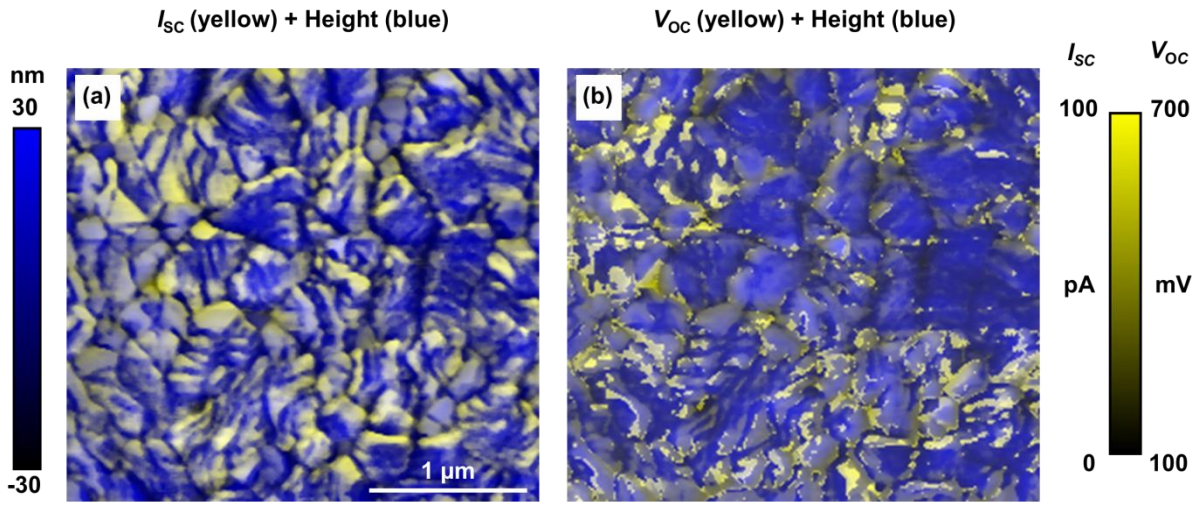

Figure 32: $MAPbI_3$ topography (blue) overlaid with color contrast from pcAFMs resolved maps of (a) I_{SC} (yellow) and (b) V_{OC} (yellow) evidencing inter- and intra-granular correlations between photovoltaic behavior and morphology.

5.5 Conclusion

In closing, pcAFMs has been used to map, for the first time, PV performance parameters of $MAPbI_3$-based HTL-free planar PSCs at the nanoscale. The PV performance parameters — I_{SC}, V_{OC}, and P_{MAX} — are all analyzed, revealing substantial variations between individual grains

and/or grain-aggregates. In the case of I_{SC}, interconnected aggregates of several adjacent grains, not just individual grains, have similar values, and remarkably only about half of the PSC area is found to generate most of the I_{SC}. The abrupt changes in the PV performance parameters from one location to another strongly indicate that transport of photocarriers is promoted by high conductivity pathways (grains, interfaces), which are often disconnected from neighboring regions by other grains and interfaces acting as barriers. Photocarriers in $MAPbI_3$ are also demonstrated to exhibit sufficiently high mobilities and diffusion-lengths such that their transport is unimpeded, at least across ~500-nm grains and/or grain-aggregates in the PSCs studied herein. Finally, periodic linear variations in I_{SC} and V_{OC} contrast are often observed within individual grains, likely due to the presence of planar defects (twins, stacking faults). Overall, the results presented here highlight the importance of measuring local PV performance parameters in PSCs and correlating them to the microstructure of the perovskite thin film. The insights gained from these unique studies into microstructure-localized PV mechanisms are essential for guiding the microstructural tailoring of OTP films for improved bulk PV performance in future PSCs.

5.6 References

1. Grätzel, M. *Nat. Mater.* **2014**, 13, 838-842.
2. Stranks, S. D.; Snaith, H. J. *Nat. Nanotech.* 2015, 10, 391-401.
3. Kim, H.-S.; Lee, C.-R.; Im, J.-H.; Lee, K.-B.; Moehl, T.; Marchioro, A.; Moon, S.-J.; Humphry-Baker, R.; Yum, J.-H.; Moser, J. E.; Grätzel, M.; Park, N.-G. *Sci. Rep.* 2012, 2, 591.
4. Kojima, A.; Teshima, K.; Shirai, Y.; Miyasaka, T. *J. Am. Chem. Soc.* **2009**, 131, 6050-6051.
5. Yang, W. S.; Noh, J. H.; Jeon, N. J.; Kim, Y. C.; Ryu, S.; Seo, J.; Seok, S. I. *Science* **2015,** 348, 1234-1237.
6. Chen, Q.; Zhou, H.; Hong, Z.; Luo, S.; Duan, H.-S.; Wang, H.-H.; Liu, Y.; Li, G.; Yang, Y. *J. Am. Chem. Soc.* **2014**, 136, 622-625.
7. Meng, Y.; Zhou, Y.; Zeng, Y.; Jiang, C.-S.; Padture, N. P.; Zhu, K. *Adv. Mater.*, **2015** (in press) DOI:adma201502586.

8. Zhou, Y.; Vasiliev, A. L.; Wu, W.; Yang, M.; Pang, S.; Zhu, K.; Padture, N. P. *J. Phys. Chem. Lett.* **2015**, 6, 2292-2297.
9. Coning, B.; Drijkoningen, J.; Gauquelin, N.; Babayigit, A.; D'Haen, J.; D'Olieslaeger, L.; Ethirajan, A.; Verbeeck, J.; Manca, J.; Mosconi, E.; Angelis, F. D.; Boyen, H.-G. *Adv. Energy Mater.* 2015, 5, 1500477.
10. Quarti, C.; Mosconi, E.; Angelis, F. D. *Phys. Chem. Chem. Phys.* **2015**, 17, 9394-9409.
11. Zhao, Y.; Zhu, K. *J. Phys. Chem. Lett.* **2014**, 5, 4175-4186
12. Huang, J.; Shao, Y.; Dong, Q. *J. Phys. Chem. Lett.* **2015**, *6*, 3218–3227.
13. de Quilettes, D. W.; Vorpahl, S. M.; Stranks, S. D.; Nagaoka, H.; Eperon, G. E.; Ziffer, M. E.; Snaith, H. J.; Ginger, D. S. *Science* **2015**, 348, 683-686.
14. Xiao, M.; Huang, F.; Huang, W.; Dkhissi, Y.; Zhu, Y.; Etheridge, J.; Gray-Weale, A.; Bach, U.; Cheng, Y.-B.; Spiccia, L. *Angew. Chem. Intl. Ed.*, **2014**, 126, 10056-10061.
15. Zhou, Y.; Yang, M.; Vasiliev, A. L.; Garces, H. F.; Zhao, Y.; Wang, D.; Pang, S.; Zhu, K.; Padture, N. P. *J. Mater. Chem. A* **2015**, 3, 9249-9256.
16. Jiang, C.-S.; Yang, M.; Zhou, Y.; Too, B.; Nanayakkara, S.; Luther, J.; Zhou, W.; Berry, J.; de Lagemaat, J. V.; Padture, N. P.; Zhu, K.; Al-Jassi, M. M. *Nat. Commun.* **2015**, 6, 8397.
17. Bergmann, V. W.; Weber, S. A. L. F.; Ramos, J.; Nazeeruddin, M. K.; Grätzel, M.; Li, D.; Domanski, A. L.; Lieberwirth, I.; Ahmad, S.; Berger, R. *Nat. Commun.* **2014**, 5, 5001.
18. Yun, J. S.; Ho-Baillie, Anita; Huang, S.; Woo, S. H.; Heo, Y.; Seidel, J.; Huang, F.; Cheng, Y.-B.; Green, M. A. *J. Phys. Chem. Lett.*, **2015**, 6, 875-880.
19. Kutes, Y.; Ye, L.; Zhou, Y.; Pang, S.; Huey, B. D.; Padture, N. P. *J. Phys. Chem. Lett.* **2014**, 5, 3335-3339.
20. Bosse, J. L.; Grishin, I.; Kolosov, O. V.; Huey, B. D. *J. Mater. Res.* **2013**, 28, 3311-3321.
21. Hamers, R. J.; Tromp, R.; Demuth, J. *Scanning Tunneling Microscopy: Springer*, **1993**, 97-100.
22. Kutes, Y.; Aguirre, B. A.; Bosse, J. L.; Cruz-Campa, J. L.; Zubia, D.; Huey, B. D. Prog. Photovoltaics, **2015** (in press) DOI: 10.1002/pip.2698
23. Zhou, Y.; Yang, M.; Wu, W.; Vasiliev , A. L.; Zhu, K.; Padture, N. P. *J. Mater. Chem. A* **2015**, 3, 8178-8184.
24. Zhou, Z.; Wang, Z.; Zhou, Y.; Pang, S.; Wang, D.; Xu, H.; Liu, Z.; Padture, N. P.; Cui, G. *Angew. Chem. Intl. Ed.* **2015**, 54, 9705-9709.
25. Hu, H.; Wang, D.; Zhou, Y.; Zhang, J.; Lv, S.; Pang, S.; Chen, X.; Liu, Z.; Padture, N. P.; Cui, G. *RSC Adv.* **2014**, 4, 28964-28967.
26. Matsumoto, F.; Vorpahl, S. M.; Banks, J. Q.; Sengupta, E.; Ginger, D. S. *J. Phys. Chem. C* **2015**, 119, 20810-20816
27. Tress, W.; Marinova, N.; Moehl, T.; Zakeeruddin, S. M.; Nazeeruddin, M. K.; Grätzel, M. *Energy Environ. Sci.* **2015**, 8, 995-1004
28. Luria, J.; Kutes, Y.; Moore, A.; Zhang, L.; Stach, E. A.; Huey, B. D., *Proceedings of the National Academy of Science.* **2015**, (submitted).
29. Li, H.; Liu, X. X.; Lin, Y. S.; Yang, B.; Du, Z. M. *Phys. Chem. Chem. Phys.* **2015**, 17, 11150-11155.
30. Kazmerski, L. L.; Russell, P. E.; Ireland, P. J.; Herrington, C. R.; Dick, J. R.; Matson, R. J.; Jones, K. M. *Grain boundaries in silicon solar cells*. No. SERI/TP-213-1761; CONF-820906-35. Solar Energy Research Institute, Golden, CO (USA), 1982.

Chapter 6: Direct Observation of Ferroelectric Domains in Solution-Processed $CH_3NH_3PbI_3$ Perovskite Thin Films

6.1 Abstract

A new generation of solid-state photovoltaics is being made possible by the use of organometal-trihalide perovskite materials. While some of these materials are expected to be ferroelectric, almost nothing is known about their ferroelectric properties experimentally. Using piezoforce microscopy (PFM), here we show unambiguously, for the first time, the presence of ferroelectric domains in high-quality β-$CH_3NH_3PbI_3$ perovskite thin films that have been synthesized using a new solution-processing method. The size of the ferroelectric domains is found to be about the size of the grains (∼100 nm). We also present evidence for the reversible switching of the ferroelectric domains by poling with DC biases. This suggests the importance of further PFM investigations into the local ferroelectric behavior of hybrid perovskites, in particular in situ photoeffects. Such investigations could contribute toward the basic understanding of photovoltaic mechanisms in perovskite-based solar cells, which is essential for the further enhancement of the performance of these promising photovoltaics.

6.2 Introduction

The past five years has witnessed a surge of interest in organometallic trihalide perovskites, which are at the heart of the new solid-state excitonic solar cells [1−3]. While these perovskites are a family of materials with the general formula $(RNH_3)MeX_3$ (R is an organic group, Me is Pb or Sn, and X is a halogen I, Br, or Cl), methylammonium (MA) lead triiodide ($CH_3NH_3PbI_3$ or $MAPbI_3$) in particular has attracted the most attention since it was first applied as light absorber in mesoscopic solar cells [4,5]. Since then the power conversion efficiency (PCE) of $MAPbI_3$-

based solar cells have shot up dramatically, which now exceeds 19% [6]. This rapid rise in the performance is the result of the innate desirable properties of $MAPbI_3$, including favorable direct band gap, large absorption coefficient, high carrier mobilities, and long carrier-diffusion lengths [4]. While the optical, electrical, electronic, and optoelectronic properties of $MAPbI_3$ perovskites have been studied in great detail [7−11], direct evidence of their ferroelectric properties is almost completely lacking. $MAPbI_3$ crystallizes in a tetragonal perovskite crystal structure (β-$MAPbI_3$) at room temperature, containing the polarizable organic cation $CH_3NH_3^+$ in 12-fold cuboctahedral coordination [12]. Perovskite β-$MAPbI_3$ belongs to the 4mm point group and I4/mcm space group, and thus, it is expected to be ferroelectric [12, 13]. In this context, Stoumpos et al. [12] have measured current (I)−voltage (V) response of bulk single crystals of β-MAPbI3 using the four-probe method, and they observe hysteretic behavior suggesting bulk ferroelectric behavior. However, β-$MAPbI_3$ thin films used in solar cells are known to comprise nano and microscale grains/domains of varying crystallinity [14] and thus, it is important to characterize and understand local ferroelectric domains in β-$MAPbI_3$ thin films, which could influence the performance of solar cells based on these perovskites in several ways. First, the ferroelectric effect induces polarization of the lattice, which in turn can enhance charge separation and concomitant longer carrier lifetimes [15]. Second, open circuit voltages above the band gap are possible due to the ferroelectric effect [16]. Finally, the commonly observed hysteresis and rate dependence in the photovoltaic response (current density−voltage or J−V) of $MAPbI_3$-based solar cells [17, 18] could be, in part, due to the ferroelectric effect. In this context, we have investigated smooth, dense β- $MAPbI_3$ thin films using piezo-force microscopy (PFM) [19] an ideal tool for probing local ferroelectric response at the domain scale. PFM is based on atomic force microscopy (AFM), where an AC electric field is applied to a scanning conducting

probe in contact with a ferroelectric thin film surface. Since all ferroelectric materials are also piezoelectric [13], the region in contact with the tip mechanically vibrates, which is simultaneously detected by the AFM during scanning. The phase difference between the piezoactuation and the applied AC field is then used to detect ferroelectric domain orientations, while the amplitude reveals domain wall positions. Superimposing a DC voltage on the domain-mapping AC signal can be used to switch the domains in situ during scanning [20]. Similarly, as employed here, poling can be achieved during scans applying continuous DC-biases (or pulse patterns), which are then alternated with zero DC-bias PFM domain mapping scans [19, 20]. In this manner, we have directly imaged domains and domains walls in β-$MAPbI_3$ thin films directly using PFM, and an attempt to switch the ferroelectric domains reversibly using scanning DC biases has been successful.

6.3 Materials and Methods

6.3.1 Hybrid Perovskite Film Synthesis

Methylammonium iodide ($CH_3NH_3PbI_3$ or $MAPbI_3$) was prepared using a process described elsewhere [25]. In a typical procedure, 24 ml of 33 wt% methylamine (CH_3NH_2) solution in anhydrous ethanol was reacted with 10 ml of 57 wt% hydroiodic acid (HI) in water, in 100 ml of ethanol (excess CH_3NH_2) in a dry Ar atmosphere at room temperature (all reagent grade chemicals obtained commercially from Sigma-Aldrich, St. Louis, MO). The solvent and the excess CH_3NH_2 were removed using a rotary evaporator, and the resulting MAI powder was washed and collected. To make a compact $MAPbI_3$ thin film, first, 30 wt% PbI_2 (Acros Organics) in N,N'-dimethylformamide (DMF; Sigma-Aldrich, St. Louis, MO) was spin-coated (6000 rpm, 40 s) onto fluorine-doped tin oxide (FTO) coated glass substrates to form a smooth PbI_2 thin film which was then dried. Second, 10 mg/ml MAI in 2-propanol was spin-coated

(6000 rpm, 40 s) onto the as-prepared PbI_2 layer, and it was then annealed at 150 ℃ for 1 min. MAI spin-coating and annealing processes were then repeated 3-4 times. The excess MAI was washed away using isopropanol, and the final thin films were annealed at 150℃ for 3 min to obtain a dark-colored β-$MAPbI_3$ perovskite. Typically thin films were prepared in ambient air (~40% RH) and they were stored in a dry box. Thin films were also prepared in a N_2-filled glovebox, but we did not observe any obvious difference between the two.

6.3.2 Characterization

The as-deposited β-$MAPbI_3$ thin films were characterized using X-ray diffraction (XRD; D8-Advance, Bruker, Karlsruhe, Germany) using Cu $K\alpha_1$ radiation (λ=1.5406 Å) with a 2θ range of 10°-60° and a step size of 0.02°. The surface of the as-deposited β-$MAPbI_3$ thin films was observed using a scanning electron microscope (SEM; LEO 1530VP, Carl Zeiss, Munich, Germany). The local roughness of the β-$MAPbI_3$ thin films was characterized using a conventional atomic force microscope (MFP-3D Origin, Asylum Research, Santa Barbara, CA).

Figure 33A is a schematic diagram showing a new solution processing method successive spin-coating/annealing (SSCA) - used in this study to prepare β-$MAPbI_3$ thin films. This method, which is a variation of the conventional two-step process used to synthesize β-$MAPbI_3$ thin films for planar solar cells [21], uses multiple iterations of rapid spin-coating of MAI on the PbI_2 layer and annealing steps. (See Supporting Information for all the experimental procedures involving synthesis, characterization, and PFM.)

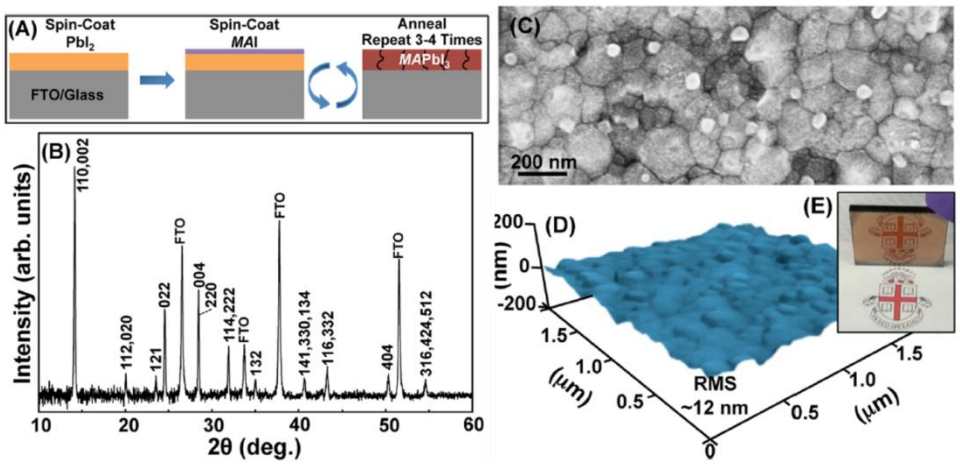

Figure 33: (A) Schematic diagram showing the SSCA solution-processing method. Characteristics of top surface of as-processed β-$MAPbI_3$ thin films: (B) indexed XRD pattern (peaks from FTO substrate are marked), (C) SEM micrograph, and (D) AFM scan (2 × 2 μm^2) showing RMS roughness of ~12 nm. (E) Photograph showing the mirror-like reflective nature of the smooth as-processed β-$MAPbI_3$ thin film (25 × 25 mm^2).

Figure 33B is an indexed X-ray diffraction (XRD) pattern of the resulting thin films (~100 nm thickness) showing phase-pure tetragonal β-$MAPbI_3$ perovskite. Figure 33C is a scanning electron micrograph (SEM) showing the dense, coarse-grained nature of the polycrystalline β-$MAPbI_3$ thin film. The grain size is estimated at ~100 nm, suggesting that most grains span the thickness of the thin film. The smooth surface topography in the β-$MAPbI_3$ thin film is clearly evident from the AFM image (noncontact mode) in Figure 33D, and analysis of local surface topography data reveals a RMS roughness of ~12 nm. Furthermore, the β-$MAPbI_3$ thin film surface looks mirror-like and "shiny" to the naked eye over a large area (Figure 33E). The desirable attributes in these β-$MAPbI_3$ perovskite thin films - phase-pure, high crystallinity, dense, coarse-grained, smooth - are due to the new SSCA protocol (Figure 33A), allowing us to perform careful PFM experiments. In SSCA, successive MAI spin-coating/annealing steps replace the dipping, or the single spin-coating, step in the conventional two-step process. The rapid spin-coating of the MAI solution allows quick drying of an extremely thin, dense film of

MAI. The subsequent heat-treatment (150 °C) results in the solidstate conversion reaction: PbI_2 + MAI → $MAPbI_3$. However, the amount of MAI is not sufficient for the conversion of the full thickness of the PbI_2 thin film, as evinced by the yellow color of the thin film observed after the first cycle (not shown here). Repeating the MAI spin-coating/annealing steps 3−4 times results in the full conversion of the entire PbI_2 thin film into phase-pure β-$MAPbI_3$. Thus, promoting solid-state reaction between MAI and PbI_2 step-by-step, while minimizing the presence of liquid solution during each repeat cycle, is key to obtaining high quality β-$MAPbI_3$ thin films reported here. In contrast, the conventional MAI solution single dipping, or spin coating, process for the fabrication of planar solar cells allows the conversion reaction to occur in the presence of the solution over a relatively long period of time, forming relatively rough thin films with interconnected β-$MAPbI_3$ particles and voids [21, 22].

6.3.3 Piezo-Force Microscopy (PFM)

PFM was performed with a different AFM (Cypher, Asylum Research, Santa Barbara, CA). A function generator (Agilent Technologies 33220A, Santa Clara, CA) was used to bias the tip with AC and/or DC signals, while the back electrode of the specimen was grounded. The synchronization channel was used as the reference signal for a lock in amplifier (HF2LI-MF, Zurich Instruments, Zurich, Switzerland) to determine and map the relative phase and amplitude of the cantilever deflection, i.e. the local piezoresponse. Typical driving frequencies were on the order of 500-1600 kHz with peak-peak AC biases of 2-4 V, while DC biases for poling ranged ±8 V. The measurements were performed with conductive diamond coated probes (Nanosensors CDT, NanoAndMore USA, Lady's Island, SC). Note that all PFM images are acquired with an AC signal only, while poling is separately achieved by scanning with DC biases only. The multiple images in Fig. 3 have been aligned using FIJI image processing software. All PFM

experiments were performed in ambient air (RH ~40%) the same day the thin films were prepared (vacuum packed for transportation). The thin films did decompose after several hours in ambient air, resulting in MAI and PbI_2, which showed no PFM contrast.

6.4 Results and Discussion

Figure 2A is a 1 × 1 μm^2 AFM image (contact mode) showing the representative topography for the β-$MAPbI_3$ thin film. Bright contrast indicates protrusions and depressions in the range ±20 nm, respectively, revealing grain sizes on the order of 100−200 nm, which is consistent with the SEM observations (Figure 33C). Figures 34B, C are simultaneously acquired PFM amplitude- and phase-contrast images, respectively. Ferroelectric domains in the β-$MAPbI_3$ thin films are clearly indicated by the complete 180° phase-contrast observed throughout Figure 34C (+90° to −90°). These out-of-phase and in-phase signals represent regions with piezoresponse vector components oriented into and out of the surface, respectively. Null contrast in the amplitude image (Figure 34B) identifies the intermediate domain wall locations.

PFM contrast can be susceptible to topographic artifacts, as with any AFM-based measurement technique. If similar contrast occurs only for specific slopes or curvatures, this usually indicates tip−sample convolution artifacts. Accordingly, the piezoresponse has been overlaid on a three-dimensional map of the topography (Figure 34D, E), where the color contrast displays the amplitude and phase of the piezoactuation vector with the same color scales as in Figure 34B,C, respectively. The piezoresponse (especially the phase) is clearly independent of the local magnitude and orientation of the sample slope and curvature. Thus, Figure 34 provides, for the first time, direct evidence for the presence of ferroelectric domains in β-$MAPbI_3$ perovskite thin films. The average domain size in the PFM images (Figures 34B and 34C) appears to be ~100

nm, which is about the average size of the grains (Figure 33C). The conductive probes (contact mode) used in PFM are not as sharp compared to those used in conventional AFM, somewhat limiting spatial resolution of a given surface morphology, though sub-10 nm contact areas are expected for flat regions based on the imaging conditions. With this in mind, individual domains appear to correspond with individual grains in the β-$MAPbI_3$ thin films.

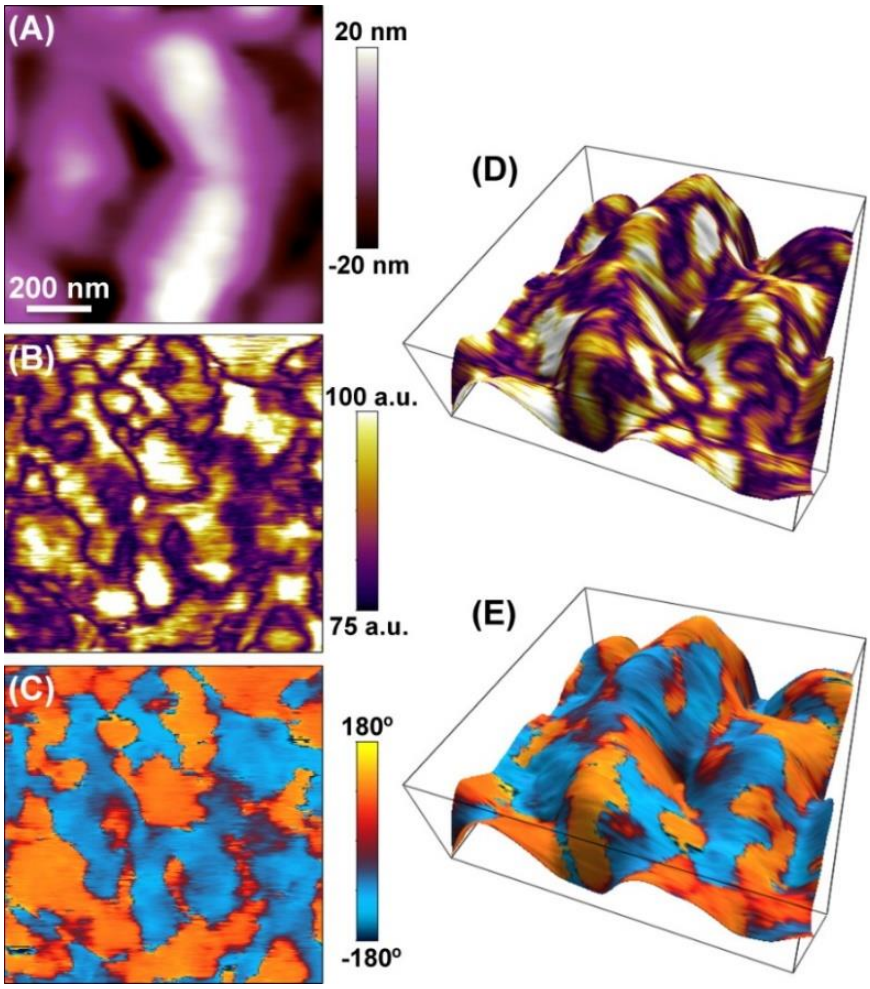

Figure 34: AFM and PFM images of as-processed β-$MAPbI_3$ thin film (1 × 1 μm^2): (A) AFM topography, (B) PFM amplitude, (C) PFM phase, (D) superimposed topography and amplitude, and (E) superimposed topography and phase.

Figure 35 presents results from an experiment aimed at poling the ferroelectric domains in a β-$MAPbI_3$ thin film. The top row in Figure 35 presents height images (topography) of a single 2.5 × 2.5 μm^2 area, repeatedly scanned with AFM. Underneath each topography image is a simultaneously acquired corresponding PFM piezoresponse map, each obtained after a prior scan that poled the same area with pure DC bias (as labeled). To present the ferroelectric domains most clearly, A·sin(φ) is displayed, where A is the amplitude and φ is the phase, in which case domains oriented into or out of the surface exhibit opposite amplitudes of piezoactuation (i.e., out of phase for the typical ±90° shift). The PFM images in Figure 35, which are positioned according to the prior poling DC bias in order to visually depict the poling sequence, are acquired without any applied DC bias to minimize capacitive artifacts [23].

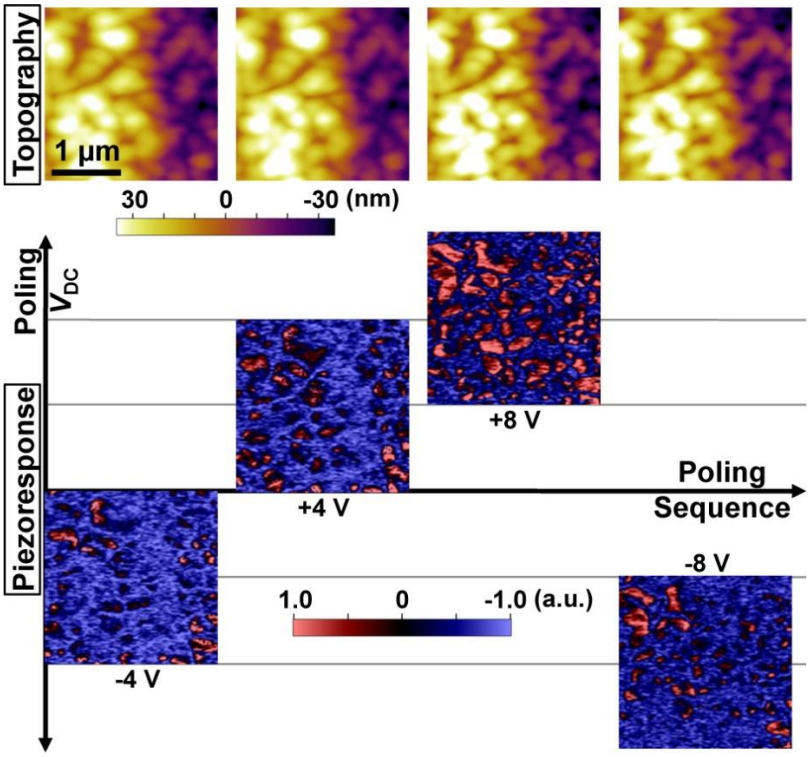

Figure 35: Four AFM topography images (top row) of a single 2.5 × 2.5 μm^2 area, with simultaneously acquired corresponding PFM images beneath mapping the A·sin(φ) piezoresponse, each after scanned DC poling at the biases indicated (VDC), evincing partial, reversible ferroelectric domain switching in as-processed β-$MAPbI_3$ thin film.

Throughout this experiment of more than eight consecutive scans, there is little evidence of specimen damage according to the nearly identical topography images (top row). This is despite the relatively soft nature of the β-$MAPbI_3$ thin films, which can be prone to deformation under the probe tip, especially in contact-mode imaging as required by PFM. The piezoresponse, on the other hand, is absolutely influenced by the poling DC bias magnitude and polarity. Compared to the initial image that followed DC poling with −4 V, several domains switch upon application of +4 V to the entire area. More domains then switch following the application of a larger DC bias of +8 V. After applying −8 V DC bias, many of these domains switch back to their original orientation. This is highlighted more clearly in the table-of-contents figure, which presents the difference in PFM phase contrast between these two extreme conditions (+8 V → −8 V). Of course, this applied DC bias is much larger than that used in the operation of perovskite-based solar cells, although the actual field applied across the film may be lower by a factor of two or more due to the tip−sample junction, as is common in PFM measurements. As has been recently reported in other materials [24], PFM-like contrast can sometimes occur due to electrochemical phenomena. This might be caused by, or lead to, modification of the specimen surface, local changes in the dielectric constant, ionic motion, etc. However, these mechanisms are typically accompanied by a significant change in topography, and/or relaxation of the topographic and/or PFM signals on the order of hundreds of seconds. Here, the topography remains unchanged throughout Figure 35 (top row). Furthermore, the time between DC poling and PFM imaging of any given region ranges from 2 to 1024 s from top to bottom of each consecutive scan, respectively. This is because full image acquisition times are on the order of 8 min, and sequential images are scanned in opposite y direction. Therefore, the evidence in Figure 35 supports the presence of ferroelectric domains in β-$MAPbI_3$ thin films. Furthermore, the ability

to manipulate the domain orientation could possibly be used to influence photovoltaic performance in future work. This experimental demonstration of the presence of ferroelectric domains in β-$MAPbI_3$ thin films and their reversible switching has several implications, some of which are discussed below. Based on some theoretical work, Frost et al. [15,18] hypothesize that polarized ferroelectric domains within the β-$MAPbI_3$ film may act as small internal p−n junctions, aiding the separation of photoexcited electron and hole pairs. They suggest that the segregated paths (“ferroelectric highways”) for electrons and holes provided by a distribution of these internal p−n junctions would reduce recombination as the charge carriers travel across the thin film [18]. They also postulate that these effects could be responsible for the observed hysteresis and degradation of the photovoltaic performance in β-$MAPbI_3$-based solar cells [18]. Note that these hypotheses are based on the existence of extremely small domains (several unit cells wide) [18]. However, the ferroelectric domains in β-$MAPbI_3$ thin films we observe in this first report are relatively large (∼100 nm). Further work is needed to see if finer sub-grain domains can be resolved in these hybrid perovskite thin films and if the hypothesized local p−n junctions exist. Juarez-Perez et al. [10] have demonstrated experimentally giant dielectric constant (GDC) effect in β-$MAPbI_3$ thin films, where an already high dielectric constant (low-frequency) of 1000 increases by a factor of 1000 under 1 sun illumination. The presence and switching of the ferroelectric domains could play an important role in unraveling the mechanisms responsible for the observed GDC effect in these thin films. Finally, Kim et al. [25] have performed a theoretical investigation of Rashba band splitting in β-$MAPbI_3$, where they show that polarization can be switched by external electric fields. This enables a controllable Rashba effect, providing the possibility of exploiting both spin and orbital freedom degrees in

photoinduced effects in β-MAPbI3 [25]. Thus, the reversible switching of ferroelectric domains in β-$MAPbI_3$ thin films demonstrated here could also have implications in this regard.

6.5 Conclusion

In summary, ferroelectric domains are observed directly for the first time in solution-processed, high-quality β-$MAPbI_3$ thin films using piezoforce microscopy. The domains are approximately equal in size to the grains (~100 nm). Reversible ferroelectric domain switching has also been achieved by poling with DC biases. These experimental results encourage further investigations into the local ferroelectric behavior of hybrid perovskites, in particular through in situ characterization of photoeffects, as well as exploring domain engineering. Such investigations could yield new insights into the fundamental photovoltaic mechanisms for perovskite-based solar cells, potentially suggesting routes to enhance the performance of this promising class of novel photovoltaics.

6.6 References

1. Service, R. F. Perovskite Solar Cells Keep on Surging. Science 2014, 344, 458.
2. Mcgehee, M. D. Materials Science: Fast-Track Solar Cells. Nature 2013, 501, 323−325.
3. Hodes, G. Perovskite-Based Solar Cells. Science 2013, 342, 317− 318.
4. Kim, H. S.; Im, S. H.; Park, N.-G. Organolead Halide Perovskite: New Horizons in Solar Cell Research. J. Phys. Chem. C 2014, 118, 5615−5625.
5. Snaith, H. J. Perovskites: The Emergence of a New Era for LowCost, High-Efficiency Solar Cells. J. Phys. Chem. Lett. 2013, 4, 3623− 3630.
6. Zhou, H.; Chen, Q.; Li, G.; Luo, S.; Song, T.-B; Duan, H.-S; Hong, Z.; You, J.; Liu, Y.; Yang, Y. Interface Engineering of Highly Efficient Perovskite Solar Cells. Science 2014, 345, 542−546.
7. Xing, G.; Mathews, N.; Sun, S.; Lim, S. S.; Lam, Y. M.; Gratzel,¨M.; Mhaisalkar, S.; Sum, T. C. Long-Range Balanced Electron and Hole-Transport Lengths in Organic-Inorganic CH3NH3PbI3. Science 2013, 342, 344−347.
8. Wolf, S. D.; Holovsky, J.; Moon, S.-J.; Lö per, P.; Niesen, B.; Ledinsky, M.; Haug, F.-J.; Yum, J.-H.; Ballif, C. Organometallic Halide Perovskites: Sharp Optical Absorption Edge and Its Relation to Photovoltaic Performance. J. Phys. Chem. Lett. 2014, 5, 1035−1039.

9. Savenije, T. J.; et al. Thermally Activated Exciton Dissociation and Recombination Control the Organometal Halide Perovskite Carrier Dynamics. J. Phys. Chem. Lett. 2014, 5, 2189−2194. (10) Juarez-Perez, E. J.; Sanchez, R. S.; Badia, L.; Garcia-Belmonte, G.; Kang, Y. S.; Mora-Sero, I.; Bisquert, J. Photoinduced Giant Dielectric Constant in Lead Halide Perovskite Solar Cells. J. Phys. Chem. Lett. 2014, 5, 2390−2394.
10. Tan, Z.-K.; et al. Bright Light-Emitting Diodes Based on Organometal Halide Perovskite. Nat. Nanotechnol. 2014, 9, 687−692.
11. Stoumpos, C. C.; Malliakas, C. D.; Kanatzidis, M. G. Semiconducting Tin and Lead Iodide Perovskites with Organic Cations: Phase Transitions, High Mobilities, and Near-Infrared Photoluminescent Properties. Inorg. Chem. 2013, 52, 9019−9038.
12. Lines, M. E.; Glass, A. M. Principles and Applications of Ferroelectrics and Related Materials; Oxford University Press: London, 2001.
13. Edri, E.; Kirmayer, S.; Henning, A.; Mukhopadhyay, S.; Gartsman, K.; Rosenwaks, Y.; Hodes, G.; Cahen, D. Why Lead Methylammonium Tri-Iodide Perovskite-Based Solar Cells Require a Mesoporous Electron Transporting Scaffold (But Not Necessarily a Hole Conductor). Nano Lett. 2014, 14, 1000−1004.
14. Frost, J. M.; Butler, K. T.; Brivio, F.; Hendon, C. H.; Schilfgaarde, M.; Walsh, A. Atomistic Origins of High-Performance in Hybrid Halide Perovskite Solar Cells. Nano Lett. 2014, 14, 2584− 2590.
15. Huang, H. T. Solar Energy: Ferroelectric Photovoltaics. Nature Photonics. 2010, 4, 134−135.
16. Snaith, H. J.; Abate, A.; Ball, J. M.; Eperon, G. E.; Leijtens, T.; Noel, N. K.; Stranks, S. D.; Wang, J. T.-W.; Wojciechowski, K.; Zhang, W. Anomalous Hysteresis in Perovskite Solar Cells. J. Phys. Chem. Lett. 2014, 5, 1511−1515.
17. Frost, J. M.; Butler, K. T.; Walsh, A. Molecular Ferroelectric Contributions to Anomalous Hysteresis in Hybrid Perovskite Solar Cells. APL Mater. 2014, 2, 081506. The Journal of Physical Chemistry Letters Letter 3338 dx.doi.org/10.1021/jz501697b | J. Phys. Chem. Lett. 2014, 5, 3335−3339
18. Gruverman, A.; Auciello, O.; Tokumoto, H. Imaging and Control of Domain Structures in Ferroelectric Thin Films via Scanning Force Microscopy. Annu. Rev. Mater. Sci. 1998, 28, 101−123.
19. Huey, B. D.; Premnath, R. N.; Lee, S.; Polomoff, N. A. High Speed SPM Applied for Direct Nanoscale Mapping of the Influence of Defects on Ferroelectric Switching Dynamics. J. Am. Ceram. Soc. 2012, 95, 1147−1162.
20. Burschka, J.; Pellet, N.; Moon, S. J.; Humphrey-Baker, R.; Gao, P.; Nazeeruddin, M. K.; Gratzel, M. Sequential Deposition as a Route¨ to High-Performance Perovskite-Sensitized Solar Cells. Nature 2013, 499, 316−319.
21. Xiao, Z.; Bi, C.; Shao, Y.; Dong, Q.; Wang, Q.; Yuan, Y.; Wang, C.; Gao, Y.; Huang, J. Efficient, High Yield Perovskite Photovoltaic Devices Grown by Interdiffusion of Solution-Processed Precursor Stacking Layers. Energy Environ. Sci. 2014, 7, 2619−2623.
22. Huey, B. D.; Ramanujan, C.; Bobji, M.; J. Blendell, J. E.; White, G.; Szoszkiewicz, R.; A. Kulik, A. The Importance of Distributed Loading and Cantilever Angle in Piezo-Force Microscopy. J. Electroceram. 2004, 13, 287−291.
23. Kalinin, S. V.; Jesse, S.; Tselev, A.; Baddorf, A. P.; Nina, B. The Role of Electrochemical Phenomena in Scanning Probe Microscopy of Ferroelectric Thin Films. ACS Nano 2011, 5, 5683−5691.

24. Kim, M.; Im, J.; Freeman, A. J.; Ihm, J.; Jin, H. Switchable S = 1/ 2 and J = 1/2 Rashba Bands in Ferroelectric Halide Perovskites. Proc. Natl. Acad. Sci. U. S. A. 2014, 111, 6900−6904.
25. Lee, M.M.; Teuscher, J.; Miyasaya, T.; Murakami, T.N.; Snaith, H.J. Efficient Hybrid Solar Cells Based on Meso-Superstructured Organometal Halide Perovskites. Science, 2012, 338, 643-647.

Chapter 7: Conclusion and Future Work

7.1 Introduction

In this thesis, advances are made in the nanoscale electrical characterization of photovoltaics by developing and implementing atomic force microscopy techniques. A few examples of these advances include high resolution mapping of crucial performance metrics of solar cells with a faster approach than existing methods, the utilization of AFM in an unconventional way for mechanical sample modifications, the development of planarization, nanomilling and oblique cross sectioning techniques in order to volumetrically investigate materials properties at the nanoscale, shedding light onto the charge transport mechanisms in CdTe solar cells, and finally, presenting evidence for the presence of switchable ferroelectric domains in high-quality hybrid perovskite thin films, all for the first time. Although the majority of this work focuses on CdTe/CdS based thin film solar cells, the studied approaches are ultimately applicable to a wide variety of solar devices as demonstrated with the emerging technology of hybrid perovskite cells, and may be adapted to characterization research in other semiconductor-based fields. Most of the work presented here were *unplanned* outcomes of the challenges encountered during the efforts made towards the *planned* research. Naturally, a significant amount of these challenges are still to be resolved. The following sections provide suggestions, potential future experiments, and analyses that can add significant insight to the already presented results, and will hopefully guide future researchers to plan their work around the most important questions.

7.2 Photoconductive AFM Spectroscopy

The major driving force behind developing the pcAFMs technique was to find a more efficient way to produce high resolution maps quickly, compared to the conventional point by point I/V

maps. In conventional measurements, the process of continually moving and stabilizing the AFM probe results in a slow process and hence susceptible to positional (thermal) drift, which in turn limits the practical spatial resolution (pixel density).

With pcAFMs [1], a series of conductive AFM (cAFM) images are collected, in dark and light conditions, each at a distinct applied DC bias incremented for each frame similar to CITS imaging with STM [2]. The local photocurrent for any given pixel position is easily extracted from each distinct image (voltage), which in this work is uniquely used to construct high spatial resolution property maps (conductivity=G, short circuit current= I_{SC}, open circuit voltage= V_{OC}, P_{MAX}). This method still requires a drift correction based on the stack of simultaneously collected topography data and this is done by the stack alignment tool in ImageJ/FIJI software [3]. After the images are aligned, distinct I-V curves are then constructed at each pixel and fit to a relevant model.

Two straightforward fitting techniques are used in this thesis; however, effort should be placed for more sophisticated fits in the future. In Figure 36, which presents the equivalent circuit for a solar cell, it is clear that these devices are prone to series and shunt resistances. These resistive losses that occur in the tip, junctions, and/or specimen (even including the possibility of local variations) are ignored in the majority of our models for the sake of simplicity.

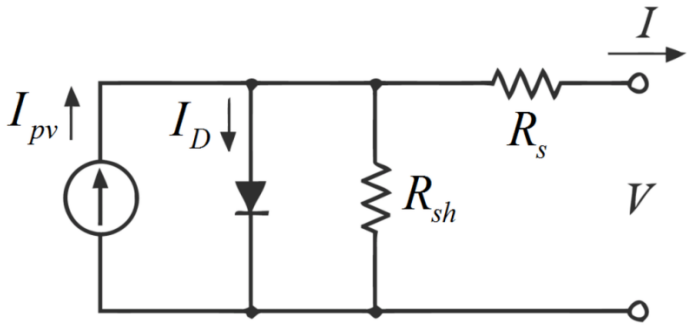

Figure 36: Equivalent circuit of a solar cell, I = Overall current, Iph = Photocurrent, Id = Diode current, Rsh = Shunt resistance, Rs = Series resistance, V = potential difference [4]

As an example, Figure 37 shows three distinct I/V behavior of solar cells upon illumination. Our pcAFMs analysis reveals a general I/V behavior similar to Figure 37c, which represents the case of a high series resistance. This behavior can be observed in Figure 38a, which shows three randomly selected examples of pcAFMs constructed I/V curves that are modeled by using 6th order polynomial fit.

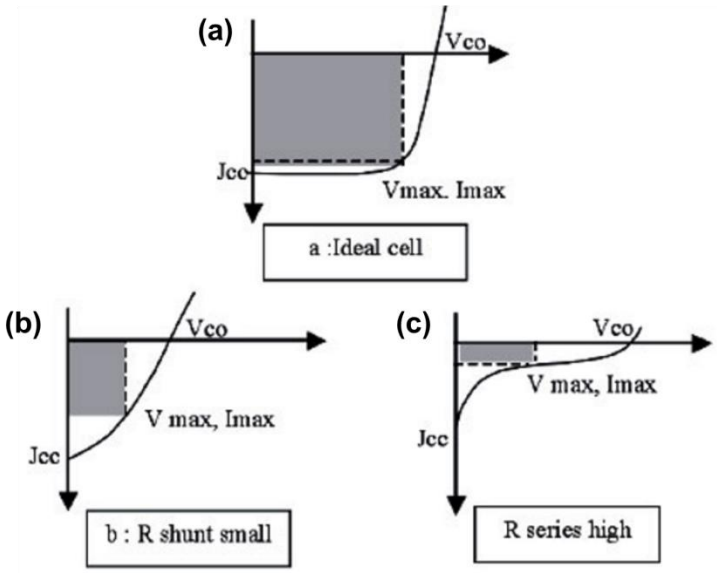

Figure 37: I/V Characteristics of a solar cell under illumination: ideal cell (a), small R_{sh} (b), high R_s (c) [5]

It is possible to estimate the shunt and series resistances by using the slopes of an I/V curve at short circuit and open circuit conditions, respectively. The estimated series resistance Rs is mapped by pcAFMs and shown in Figure 38e along with the corresponding I_{SC} and V_{OC} maps of the same 5 µm x 5 µm area. The effort to determine shunt resistance with the same method fell short. It is suggested that, after estimating R_s and R_{sh}, the raw data should be remodeled by inserting the resistance information in the modeling, which has not been done in this work.

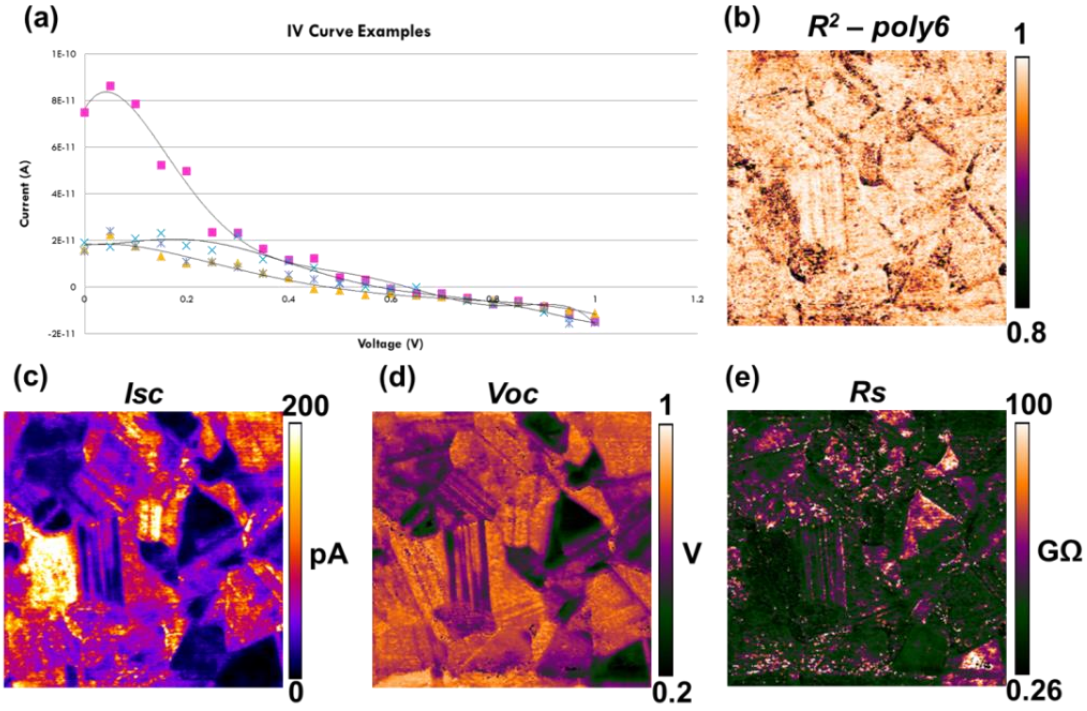

Figure 38: (a) pcAFMs constructed I/V curve examples, (b) Correlation coefficient, R^2, for a 6th order polynomial fit, pcAFMs constructed maps of (c) short circuit current (I_{SC}) (d) open circuit voltage (V_{OC}) and (e) series resistance (R_s)

In case the above method does not result in meaningful estimates, another technique to determine series resistance is based on the measurement of I/V curves at two different light intensities

giving $I_{SC\,1}$ and $I_{SC\,2}$ [6]. In this method, currents δI below $I_{SC\,1}$ and $I_{SC\,2}$ are picked on both I/V curves which correspond to voltages V_1 and V_2. The series resistance can then be calculated as;

$$Rs = \frac{V1 - V2}{Isc2 - Isc1}$$

For this work, it would mean modulating the light intensity twice at each applied voltage during pcAFMs, which in turn would result in three distinct current images collected at each voltage step, namely; current in dark, current upon $Intensity_1$ and current upon $Intensity_2$. After collecting this data stack and accounting for thermal drift, above equation can be applied at each pixel to mathematically calculate and map R_s spatially.

7.3 EBSD Mapping

A useful method to assess the local microstructure, composition, and orientation for correlation to AFM-based measurements, is electron microscopy. While scanning electron microscopy (SEM) and energy dispersive spectroscopy (EDS) are widely implemented to provide an overview of the surface and chemical composition, measuring local orientations is more challenging, with the most common approach being electron backscatter diffraction (EBSD).

EBSD is ideal for the CdTe based solar cells studied here due to the sub-micron grain size, well within the spatial resolution of modern EBSD systems. Most of all, it can be employed to specimens with limited sample preparation, unlike other orientation mapping methods such as TEM based Kikuchi analysis which necessitates specimen thinning, HRTEM requiring even thinner samples, or point diffraction patterns which do not easily allow the requisite mapping

capabilities important for the work proposed here. UConn has very recently acquired an EBSD facility and the work presented in Chapter 3 of this thesis has resulted in a sample preparation technique that can be used without having to deal with the adverse effects caused by FIB milling.

It is recommended to take advantage of the in-house facility to make back and forth sequential measurements in the following sequence: planarization, pcAFMs performance mapping, EBSD mapping, ~200 nm of CT- AFM milling and back to pcAFMs – EBSD and so on. These kinds of measurements would be similar to the already widely implemented analytical methods such as serial FIB [7], microtome cross-sectioning [8], or 3-d TEM studies [9], yet more functional when applied with AFM and its many variations to uniquely map materials functionalities through the depth of specimens, to investigate how much of an effect crystallographic orientations have on electrical performance, as well as whether the key focus should be on the 3-d connectivity of the elements in the thin film microstructure.

Also, it would be worth going after the EBSD and pcAFMs mapping of a single layer of CdTe crystals with varying orientations. This way, columnar grains that extend from one electrode to the other can be probed to study the actual contribution of grain orientations to the opto-electronic behavior. As an example, an EBSD map of such a film would look like Figure 39 and this could be achieved by nanomilling the CdTe film by using AFM, to a depth that only consists of a single layer of CdTe grains.

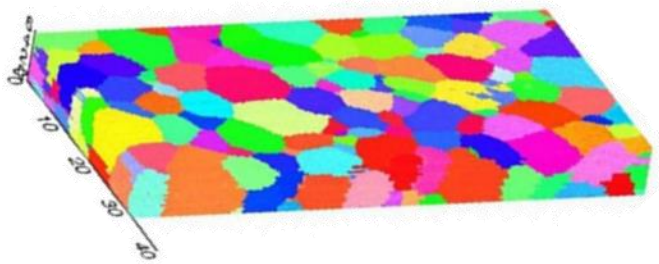

Figure 39: Representative EBSD map of a poly crystalline thin film in which most grains extend from top to bottom [10]

7.4 Patterning CdTe with AFM

Despite CdTe photovoltaics being a billion dollar per year industry, it has not had significant improvements in efficiency for years. Losses in efficiency is mostly attributed to the various microstructural defects, though, it is challenging to study the performance of these defects isolated from their surroundings.

As discussed in Chapter 2, micro and nano-islands of CdTe, fabricated to study the effect of patterning and relaxation are grown on CdS through dielectric masks. These samples are fabricated without any chemical activation treatment so that the effect of patterning could be observed. With the development of AFM based nanomilling techniques in Chapters 3 and 4, continuous thin films of CdTe can very easily be patterned as islands of desired sizes, and probed before/after patterning of the same area to investigate the effects of patterning.

For future studies, I would recommend planarizing and milling downwards, close to the back electrode, so that a better chance of working with single grains exists, instead of having sub-surface grains through thickness. Then, by scanning along a few lines of width and applying high forces, narrow trenches can be opened orthogonally like tic-tac-toe boards, thus totally isolating

some grains, interfaces or defects. Being able to isolate certain microstructural features may give invaluable insights into their real contribution to the cell performance.

7.5 Temporal Measurements

The effect of pulsed light on PV performance should be investigated by acquiring current maps upon pulsated light with a range of frequencies. The white LED source in Nanomeasurements Lab can be pulsed at a 50% duty cycle during the current acquisition, such that there is 100% exposure for half of the time. A square wave pulse of varying frequencies, however, will insure that this results in 50% exposure on average, regardless of the pulse width. The device efficiency as a function of pulse frequency can then be plotted, which should reveal time constants for photogeneration to saturate. These measurements can also be related to trapping and charging effects, which are expected to vary with proximity to various defects (e.g. grain boundaries, stacking faults etc).

7.6 Conclusion

This dissertation is a product of many challenges, which taught me important lessons that can be applied to every aspect of life. It is crucial for a researcher to be open-minded and not constrained by boundaries when it comes to performing an experiment. Of course, without violating health and safety regulations, one should be willing and courageous enough to experiment the unusual and expect the unexpected. I learned that problems can lead to even better outcomes if you are willing to figure out how to take advantage of them. In experiments, looking into doing things you think you should never do usually turns out advantageous. Be confident and trust your own intuition.

Fortunately, a lot has been achieved in this dissertation and as always, many questions are left for the next generation of students to explore. I believe that this work is only the beginning of many more achievements to come in the photovoltaics field studied in Huey AFM Lab.

7.7 References

1. Kutes, Yasemin, Brandon A. Aguirre, James L. Bosse, Jose L. Cruz-Campa, David Zubia, and Bryan D. Huey. "Mapping photovoltaic performance with nanoscale resolution." Progress in Photovoltaics: Research and Applications (2015).

2. Hamers, R. J.; Tromp, R.; Demuth, J. *Scanning Tunneling Microscopy: Springer*, 1993, 97-100.

3. Lowe D G. Distinctive image features from scale-invariant keypoints. International Journal of Computer Vision 2004 60 91-110, 10.1023/B:VISI.0000029664.99615.94

4. Cubas, Javier, Santiago Pindado, and Carlos de Manuel. "Explicit expressions for solar panel equivalent circuit parameters based on analytical formulation and the Lambert W-function." Energies 7, no. 7 (2014): 4098-4115.

5. Bernede, J. C. "Organic photovoltaic cells: history, principle and techniques." Journal of the Chilean Chemical Society 53, no. 3 (2008): 1549-1564.

6. Schroder, Dieter K. Semiconductor material and device characterization. John Wiley & Sons, 2006.

7. Giannuzzi, L. A., and F. A. Stevie. "A review of focused ion beam milling techniques for TEM specimen preparation." Micron 30, no. 3 (1999): 197-204.

8. Xu, Qiaobing, Byron D. Gates, and George M. Whitesides. "Fabrication of metal structures with nanometer-scale lateral dimensions by sectioning using a microtome." Journal of the American Chemical Society 126, no. 5 (2004): 1332-1333.

9. Janssen, Andries H., Abraham J. Koster, and Krijn P. de Jong. "Three-dimensional transmission electron microscopic observations of mesopores in dealuminated zeolite Y." Angewandte Chemie 113, no. 6 (2001): 1136-1138.

10. http://mimp.materials.cmu.edu/rohrer/research/research.html